Rare Earth Doped Silica For Integrated Optical Waveguide Lasers and Amplifiers

A thesis submitted for the degree of Doctor of Philosophy
in the Faculty of Engineering, University of Glasgow.

by

John A. Bebbington

August, 1993

This thesis is dedicated to my parents.

Acknowledgements

I would like to thank my supervisors Dr. Stewart Aitchison and Dr. John Arnold for their advice during the project. I am particularly indebted to Dr. Aitchison for his constant enthusiasm and help. I also acknowledge Professor J. Lamb and Professor P. Laybourn for the provision of research facilities in the Department of Electronics and Electrical Engineering.

Many people helped me with the technical aspects of the project and I am grateful to the departmental superintendent Tom Wright and his staff.

I would like to thank Roy Turnbull, George Thornton and Harry Anderson for the construction of the flame hydrolysis fabrication equipment and Jimmy Young, Ian McNicholl, Robert Kirk and Tommy Cairns for the maintenance. I also thank George Boyle for his sound technical advice and Joe Smith for the supply of gas bottles and discussions concerning a certain football team. I would also like to acknowledge all members of the mechanical and polishing workshop, in particular Kas Piechowiak and Hugh Moy for their help and support throughout the period of the project. I also express my thanks to: Joan Carson, Margaret Henderson, Linda Pollock and Lois Hobbs in the cleanroom; Jim Gray for his help with the laser systems; Robert Harkins for his work with e-beam writing, production of masks and for being such a 'good' loser at ten-pin bowling; Ray Darkin in the dry etching section; and Stewart Fairbairn in the electronic workshop. I also convey my gratitude to Lawrence Bradley who kept me supplied with equipment for the duration of the project and for his sense of humour, usually at my own expense.

During the project I made many friends and I thank them all for their encouragement, in particular, Jim Bonar and Giovanni Barbarossa for their friendship, advice and help with experiments.

The Science and Engineering Research Council provided financial support for the project, under a CASE studentship with BT. I would like to thank Dr. Graeme Maxwell and Jim Ainslie at BT Laboratories, Ipswich for their assistance and provision of their research facilities and materials.

Finally, and most of all, I would like to thank my family for their constant support throughout my period of study.

Abstract

The aim of the project was to realise rare earth doped planar silica waveguide lasers. Research centred on two rare earth ions: neodymium taking advantage of the four level laser system near 1.05 μm and erbium with emission at 1.54 μm, in the important third telecommunication window.

Research concentrated on SiO_2-P_2O_5 glass films fabricated by the flame hydrolysis of $SiCl_4$ and PCl_3. The resultant low density glass soot was deposited onto silica or oxidised silicon substrates, which was then sintered at temperatures up to 1350°C in a furnace to produce high quality, low loss planar waveguides. The propagation loss of the passive planar films, measured by the three-prism technique, was below 0.1 dB/cm.

Rare earth ions were incorporated into the SiO_2-P_2O_5 host glass by the solution doping technique and for the first time in the planar format, by an aerosol doping technique. The propagation loss of the rare earth doped samples was found to be dependent on the rare earth concentration and P_2O_5 codoping level. Moreover, the loss of the planar films fabricated by the multiple-step solution doping technique was dependent on the fabrication conditions. This problem was circumvented by the aerosol doping technique which incorporated the rare earth ions into the host glass in a single fabrication step and also gave the possibility of regional and vertical selective area doping of planar films.

Ridge waveguides were fabricated by a combination of photolithographic and reactive ion etching techniques. Optical assessment of neodymium and erbium doped channel waveguides included fluorescence, absorption and fluorescence lifetime measurements, which supplied information concerning the doping concentrations and ion-ion interactions. Loss measurements were also performed on the channel waveguides with air or SiO_2-B_2O_3-P_2O_5 glass acting as the cladding layer. The loss for channel waveguides clad with a glass layer was measured to be below 0.3 dB/cm with a 0.4 wt% rare earth doping level.

Finally, oscillation was achieved at 1.054 μm in 0.4 wt% and 0.5 wt% neodymium doped SiO_2-P_2O_5 channel waveguides. The core dimensions were 6 μm wide, 6 μm thick and 6 cm long. Threshold pump power for continuous wave oscillation was 25 mW for the sample with 0.4 wt% doping level, when pumped at 804 nm. The slope efficiency, with respect to the absorbed pump power, was measured to be approximately 3 % when a 5 % transmitting output coupler was used.

Table of Contents

Chapter 4 Optical Planar Waveguides

Chapter 5 Rare Earth Doped Silica Channel Waveguides

Chapter 6 Monolithic Integration of Rare Earth doped Silica Planar Waveguide Lasers and Amplifiers

Chapter 7 Conclusion and Future Work

List of Tables

Chapter 2 Rare Earth Doped Silica

Chapter 3 Fabrication of Planar Silica Films By Flame Hydrolysis Deposition

Chapter 4 Optical Planar Waveguides

Chapter 5 Rare Earth Doped Silica Channel Waveguides

Chapter 6 Monolithic Integration of Rare Earth doped Silica Planar Waveguide Lasers and Amplifiers

List of Illustrations

Chapter 2 Rare Earth Doped Silica

Chapter 3 Fabrication of Planar Silica Films By Flame Hydrolysis Deposition

Chapter 4 Optical Planar Waveguides

Chapter 5 Rare Earth Doped Silica Channel Waveguides

Chapter 6 Monolithic Integration of Rare Earth doped Silica Planar Waveguide Lasers and Amplifiers

Chapter 1 Introduction

1.1 Introduction

The modern day concept of optical communication was first perceived by Kao and Hockham in 1966 [1], who realised that a glass fibre could be used as a waveguide to transmit an optical signal. Today, optical fibres, based on fused silica, are used in intercontinental, international and national communication systems, and are being introduced in trials into the local area network, with the future customer able to receive services ranging from telephony to high-definition television. However, only until a network is realised which transmits and processes in the optical domain will the full potential of an optical communication system be exploited. It is probable that the optical signal processing function will be performed by integrated waveguide technology.

S. E. Miller first proposed the field of Integrated Optics in 1969 [2]. Since then, integrated optical waveguides have been fabricated in various materials such as crystals, polymers and glasses. The implementation of integrated optical circuits requires a high quality optical waveguide with a low loss and a precisely controlled structure yielding a low fibre to waveguide coupling loss. Optical waveguides fabricated from a high silica technology based on a combination of flame hydrolysis and reactive ion etching provides such high performance and cost effective circuits, with the possibility of monolithic integration of active and passive functions by means of doping with rare earth metals.

1.2 Synopsis

The object of the work described in this thesis was to fabricate and characterise rare earth doped silica and demonstrate integrated optical waveguide lasers.

Chapter 2 outlines the applications of rare earth doped doped silica fibres in telecommunications, methods of rare earth doping and the optical properties of rare earth ions in silica. The final section of the chapter discusses the extension of the technology to integrated optics, facilitating integrated optical sources and amplifiers.

The technique used for film fabrication was Flame Hydrolysis Deposition. Chapter 3 reviews the high-silica technology, describes in detail the fabrication equipment and gives an account of the theory and fabrication process to produce high silica planar films.

The fabrication of planar rare earth doped silica waveguides using the solution doping technique and for the first time in the planar format, an aerosol doping technique, are presented in chapter 4. The refractive index and thickness of films are measured using prism coupling experiments. Loss measurements are made of the planar films using the three-prism and fibre probe methods.

Chapter 5 deals with the fabrication of ridge waveguides, giving details of the photolithographic, reactive ion etching and polishing processes. The chapter also concentrates on the optical properties of the rare earth doped silica ridge waveguides and reports the successful demonstration of neodymium doped silica planar waveguide lasers.

To attain the goal of an integrated optical waveguide laser or amplifier, Bragg reflectors acting as feedback elements in a laser structure and selective area doping are necessary. In Chapter 6, the peak reflectivity of the gratings is modelled as a function of length for different amplitudes of grating corrugation and a description of the fabrication of the gratings is presented. The methods of regional and vertical selective area doping using the aerosol and solution doping techniques are also outlined.

Finally, Chapter 7 contains the conclusions of the work and discusses the areas of research that the author feels the direction of future research should follow in order to achieve the monolithic integration of active and passive functions and demonstrate functionable devices.

1.3 References

1. Kao, K.C., and Hockham, G. A.
Proc. IEE, 1966, **13**, 1151.
2. Miller, S.E.
Bell System Tech. J., 1969, **48**, 2059.

Chapter 2 Rare Earth Doped Silica

2.1 Introduction

In the penultimate row of the periodic table, after the element lanthanum La^{57}, the filling of the 4f electronic shell occurs from the element cerium to ytterbium. These elements are called the lanthanide or rare earth elements.

Element	**Symbol**
Cerium	Ce^{58}
Praseodymium	Pr^{59}
Neodymium	Nd^{60}
Promethium	Pm^{61}
Samarium	Sm^{62}
Europium	Eu^{63}
Gadolinium	Gd^{64}
Terbium	Tb^{65}
Dysprosium	Dy^{66}
Holmium	Ho^{67}
Erbium	Er^{68}
Thulium	Tm^{69}
Ytterbium	Yb^{70}

Table 2.1 List of rare earth ions.

All the rare earth elements have the same outer electronic configuration of $5s^2 5p^6 6s^2$, plus a varying number of electrons in the inner 4f shell which determines the optical properties.

Normally, the rare earths exist as triply oxidised ions, with both the $6s^2$ and one of the 4f electrons removed, leaving the electrons in the 5s and 5p shell unaffected. As a consequence, the filled outer shells of the ion partially shield the inner 4f electrons from the ligand field of the host, electron-phonon coupling effects are weak and hence the energy levels of the ion in the host are similar to those for the free ion.

The low lying energy levels of the rare earth ion are determined by the forces acting on and between the electrons in 4f shell. The three main interactions that are considered are: the coulombic interaction between the electrons in the 4f shell; spin orbit coupling; and the interaction between the host crystal field and the electrons in the 4f shell.

The Hamiltonian may be written as:

$$\hat{H} = \hat{H}_o + \hat{H}' + \hat{H}_{so} + \hat{H}_c \qquad (2.1)$$

where $\hat{H}_0$ gives the hydrogenic configuration energy.

$\hat{H}'$ is the inter-electron coulomb interaction which has the effect of splitting the single-electron configuration into a number of different energy levels. Each of these levels are described by a particular pair of quantum numbers, L and S, where L and S are obtained by summing vectorally the angular momenta, l_i, and spin momenta, s_i, of the individual 4f electrons:

$$L = \sum_i l_i \qquad S = \sum_i s_i \qquad (2.2)$$

The spin-orbit term, $\hat{H}_{so}$, splits these energy levels into 'multiplets' by causing the energy of a state to be dependent on the total angular momentum quantum number, J, where J is the vector sum of L and S, i.e. LS or Russell-Saunders coupling. The quantised energy states are labelled $^{2S+1}L_J$, where 2S+1 is the spin multiplicity and L is defined by the letters S, P, D, F, G, H, I etc which correspond to L= 0, 1, 2, 3, 4, 5, 6 etc.

Finally, the coulombic interaction, given by $\hat{H}_c$, between the host ligand field and the electrons in the 4f shell acts to give a further splitting of the multiplets. For an ion with an odd number of electrons in the 4f shell, such as Er^{3+} and Nd^{3+}, a given multiplet will split into at most J + 1/2 components. The number of possible Stark levels is dependent on the symmetry of the host, the full number being observed in glass hosts as they have less than tetragonal symmetry [1].

Although the energy levels are adequately labelled by the LS coupling scheme, electric dipole transitions between them would be forbidden, except for the effect of the ligand field breaking the inversion symmetry of the ions environment. The transition probabilities are typically 3 or 4 orders of magnitude smaller than allowed transitions, with quantum mechanical calculations of the electric dipole transition strengths first performed by Judd [2] and Ofelt [3].

A Dieke energy level diagram, such as figure 2.1, can be used to represent the energy levels of the rare earth ions [4].

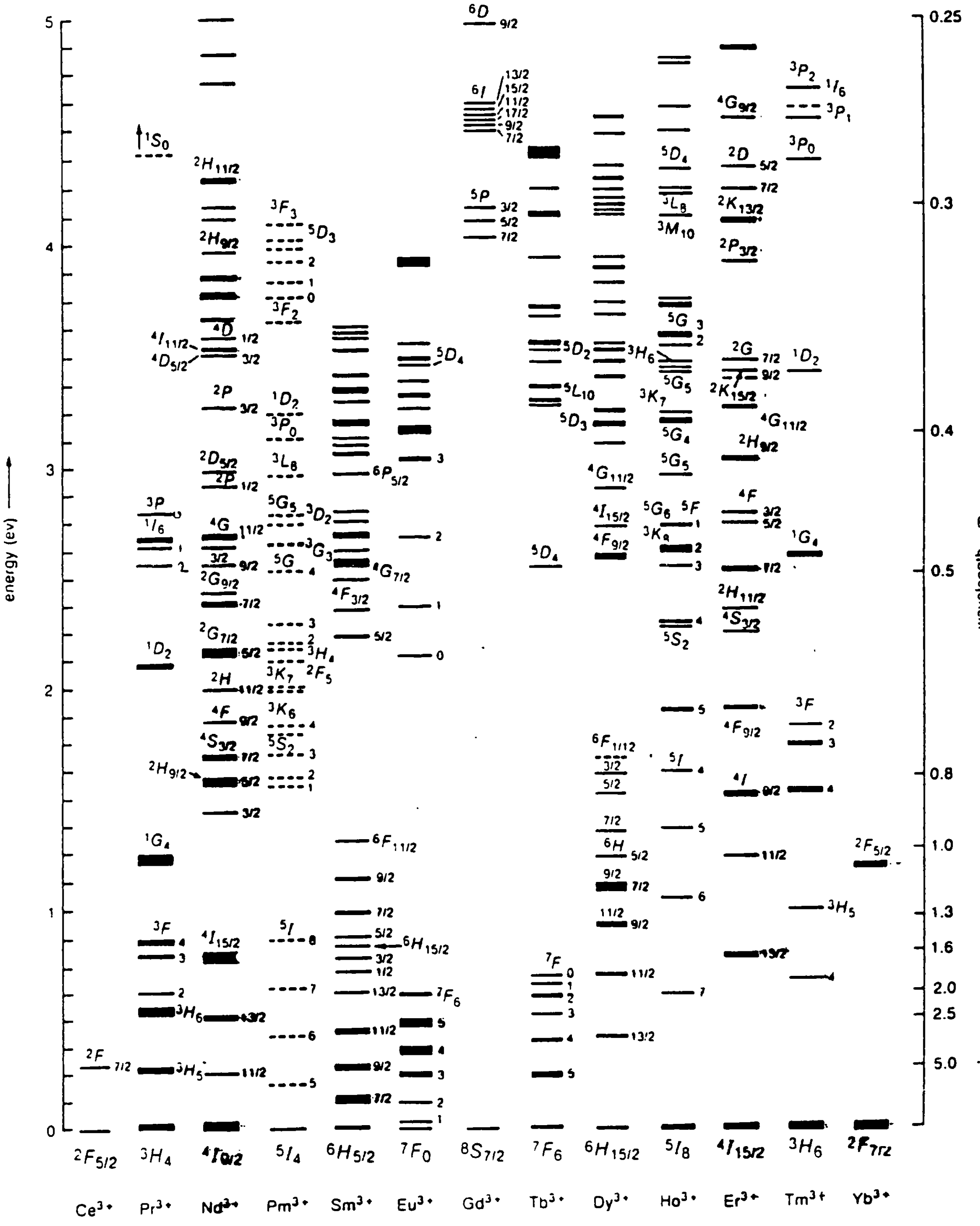

Figure 2.1 Dieke energy level diagram for rare earth ions.

2.2 Application of Rare Earth Doped Silica in Telecommunications

Considerable success has been achieved with rare earth doped silica fibre lasers and amplifiers [5]. For applications in telecommunications rare earth doped optical fibre sources and amplifiers exhibit the same low loss, high power confinement and geometry as conventional single mode fibres. They also have the added advantage of long interaction lengths and consequently low doping levels of the rare earth ion and good heat dissipation, a problem which has plagued bulk glass systems [6].

Rare earth doped fibres were first shown to be feasible optical amplifiers in 1964 [7]. A 1.06 μm signal was amplified in a Nd doped fibre pumped by a flashlamp array. In 1974, Stone and Burrus reported the first semiconductor diode pumped Nd^{3+} doped fibre laser, providing a compact, practical source [8]. However, research in the field waned until 1985 when Southampton University began to publish material concerning rare earth doped single mode fibre devices [9,10]. Interest was rekindled with the demonstration of single transverse mode fibre lasers and amplifiers fabricated using an extension of the MCVD technology [11-13]. Since then semiconductor diode pumping [14], Q-switching [15], mode-locking [16], tunable [17-19] and single longitudinal mode operation [20, 21] have been demonstrated. Many rare earth dopants have been investigated in silica optical fibres [22], but interest has concentrated on Er^{3+} doped silica due to emission at 1.54 μm, in the third telecommunication window.

At present signal regeneration in optical communication systems is carried out by converting the optical signal to an electrical signal and then back to an optical signal, with data rates approaching the maximum modulation rates of the semiconductor technology used in the optoelectronic repeaters. The maximum separation between such expensive optoelectronic repeaters is 100 km. All-optical amplification removes the need for such repeaters, with research investigating semiconductor amplifiers [23], amplifiers based on stimulated Raman scattering [24] and Er doped fibre amplifiers (EDFAs), with the latter emerging as the most effective. EDFAs have the advantage of: ease of splicing into systems with low loss; low noise and high gain with only a few milliwatts of pump power supplied from a semiconductor laser diode; high pump efficiency; a wide bandwidth enabling multichannel operation with negligible intermodulation effects at frequencies greater than 10 kHz; large signal saturation output power; and polarisation insensitivity. It is expected that trunk transmission systems and optical distribution systems will be influenced by EDFAs, the EDFAs operating as power amplifiers, repeaters in lumped or distributed form and as low noise preamplifiers [25].

2.3 Fabrication of Rare Earth Doped Silica Fibres

Rare earth ions may be incorporated into silica fibres by adaptations of the three main standard fibre-making techniques known as modified chemical vapour deposition (MCVD), vertical axial deposition (VAD) and rod-in-tube. Incorporation of the rare earth ions into the core of silica fibres can be split into liquid-phase processes, gas-phase processes and rod-in-tube method. For completeness all three processes will be described, but greater weight will be placed on the liquid phase processes: solution doping and aerosol doping, methods adopted to dope high silica planar films fabricated by flame hydrolysis deposition (FHD).

2.3.1 Liquid Phase Techniques

Solution Doping

At present the most common method for incorporating rare earth ions into silica fibres is the solution doping technique, first demonstrated by Stone and Burrus [26].

For fibres fabricated using the MCVD technique, the clad is deposited as a glass layer, but the core is deposited at a lower temperature forming a partially sintered, porous layer. The preform is then immersed in an alcohol or aqueous solution of the rare earth chloride or nitrate. The rare earth concentration incorporated is controlled by altering the duration of the immersion or by varying the solution strength and keeping the immersion time constant, the second approach giving greater control over the dopant concentration [27]. After the immersion, the sample is dried, dehydrated in a chlorine atmosphere at high temperature to remove OH^- impurities and finally sintered. The tube is then collapsed and drawn into a fibre.

The solution doping technique may also be used to dope silica fibres fabricated by the VAD technique [28], a technology from which the fabrication of planar silica films by FHD is derived. In this case a porous preform rod is formed by depositing soot synthesised in an oxy-hydrogen flame externally onto a "seed" rod. The boule is then soaked in the solution of the appropriate rare earth chloride, dehydrated, sintered and then overcladded prior to be drawn into a fibre.

The solution doping technique is a simple, reproducible method enabling a high concentration of rare earth dopant [29]. The method also gives the possibility of co-doping, for example Er^{3+} and Yb^{3+} and doping the glass with Al_2O_3 using a solution of Al(NO$_3$), which increases the solubility of the rare earth ions in the glass without the detrimental effects of clustering and enables control over the doping profile, confining the rare earth ion to the centre of the core [29,30].

Aerosol Doping

The aerosol doping technique has been used to fabricate multi-component and rare earth doped glass fibres [31,32]. The aerosol is produced by nebulizing a solution which has a low viscosity and surface tension utilising supersonic vibration or an inert carrier gas under pressure. The aerosol droplets are approximately a micrometre in diameter and consequently may be transported using a carrier gas uninhibited by gravitational settling.

For silica fibres fabricated using the MCVD technique, the rare earth ions may be added to the core by nebulizing a high purity aqueous solution of the rare earth chloride [31]. The aerosol is transported using oxygen as the carrier gas to the preform tube where a core layer has been deposited at reduced temperature forming an open porous structure. A hot zone of 1200°C is maintained in the tube and as the aerosol approaches the hot zone, the water evaporates yielding a submicron particle of NdCl$_3$ which is oxidised and incorporated into the deposited glass layer. The process of depositing another layer of silica and doping with the rare earth ion using the aerosol is repeated until the desired core thickness is achieved. Alternatively, the rare earth dopant may enter the preform tube simultaneously with the glass forming raw materials by using a multiple annular input. To circumvent the possible problem of the presence of microcrystallites in the glass, the nebulized solution may constitute all the components of the glass structure to achieve microscopic homogeneity. In this case, the precursor for silica is tetraethylorthosilicate (TEOS) which can be easily nebulized and is a suitable solvent for organo-metallic compounds of Al, P, Ge, Nd and Er [31]. The preform is then dehydrated in a chlorine atmosphere at high temperature to remove OH$^-$ impurities and finally sintered. The tube is then collapsed and drawn into a fibre.

The aerosol doping method may also be used to dope silica fibres fabricated by the VAD or outside vapour deposition (OVD) technologies [33,34]. Using a multi-conduit burner, as shown in figure 2.2, an aqueous solution of the rare earth chloride is nebulized by a pressurised inert carrier gas, which also feeds the aerosol into the oxygen rich oxy-hydrogen flame. As illustrated, the fourth conduit is longer than the first to third conduits, allowing the glass forming raw materials, the hydrogen gas and the atomised rare earth solution to mix adequately before the subsequent hydrolysis of the metal halides and oxidation of the rare earth chloride. The glass soot is then deposited with the rare earth oxide incorporated. A modification to this method is to use a nebulizer which employs supersonic vibration. The resultant aerosol is directed into the flame by a nozzle and oxidised, mixed with the particulate glass material and directed by the flame to be deposited on the target. The process to form the fibre after the doping is identical to that outlined earlier.

The concentration of the rare earth dopant incorporated using this aerosol doping technique is dependent on the strength of the solution and for the case of the nebulizer utilising a pressurised carrier gas, the flow rate of the carrier gas. The aerosol technique has the advantage in comparison to the solution doping technique, that the glass soot is doped as it is deposited, which enables control of the dopant profile during the deposition. This method also allows co-doping and high concentrations of rare earth dopant to be incorporated into the glass, similar to the solution doping method.

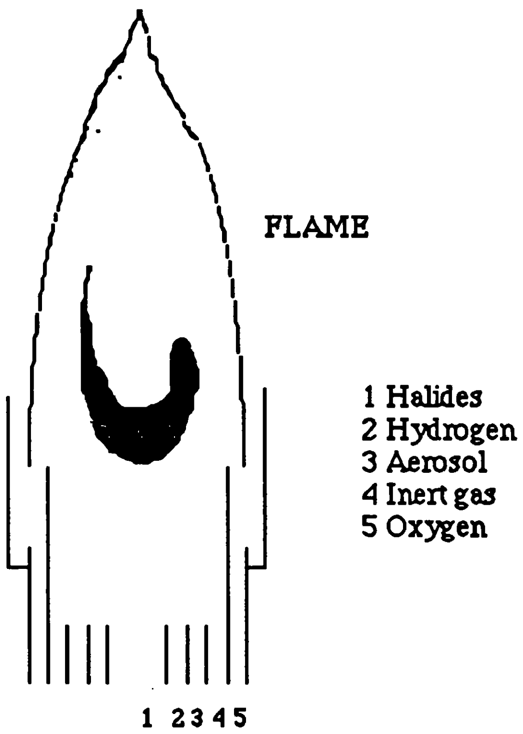

Figure 2.2 End section of multi-conduit burner, taken from reference 34.

2.3.2 Gas Phase Techniques

Rare earth doped silica fibres have also been fabricated using a gas phase technique, a consequence of rare earth chlorides having vapour pressures of approximately one torr when heated to 1000°C. Using a modification of the MCVD process [13], this method involves high purity rare earth chloride being heated, producing a vapour in a chamber attached to the front end of the silica tube where the deposition occurs. The vapour is then carried into the reaction zone along with $SiCl_4$, $GeCl_4$ and Al_2Cl_6 and O_2 to form the fibre core. The rare earth compound may be melted onto the wall of the chamber upstream from the deposition chamber or be impregnated in a porous silica generator [35], with another adaptation being to enclose the rare earth chloride in an ampoule [36].

The modified MCVD technique gives reproducible refractive index profiles and dopant concentrations. However, the technique is not as readily adaptable to dope planar films as the liquid phase processes.

2.3.3 Rod-In-Tube Technique

The rod-in-tube technique involves a rod of glass doped with rare earth ions being sleeved in a tube of lower index glass which has the same thermal expansion, which is then pulled down to form a fibre [6,37].

Summary

From the methods discussed liquid phase doping techniques are the most attractive for the incorporation of rare earth ions in planar silica films fabricated by FHD. This is due to their simplicity and the ease at which high concentrations of rare earth dopant may be achieved, necessary due to the shorter path lengths and higher propagation losses present in integrated optic waveguide lasers and amplifiers.

2.4 Optical Properties of Rare Earth Ions In Glass

Glass is an amorphous solid consisting of covalently bonded molecules. When rare earth ions are incorporated they usually exist as network modifiers or are interstitially situated in the glass network. The host influences the spectroscopic properties and the concentrations of rare earth ions able to be incorporated [5].

2.4.1 Spectroscopy and Influence of Glass Host

The spectroscopy of rare earth doped materials has been studied for many years [38, 39]. Nd and Er are of interest for telecommunication purposes because they have fluorescence bands which coincide with the second and third telecommunication windows respectively and have absorption bands suitable for semiconductor diode pumping.

A rare earth ion may be optically pumped to an excited state by the absorption of a photon, relaxing back to the ground state by radiative transitions by the emission of a photon or by non-radiative means, by the excitation of optical phonons of the host matrix. The most direct route for an ion to decay back to the ground state is by the emission of a photon of energy equal to the difference between the excited state and the ground state. However, in most cases the probability of such radiative decay is far outweighed by the probability of rapid relaxation to an intermediate energy level by multi-phonon decay. The lifetime of an energy level from which the ion decays by multi-phonon decay is proportional to the energy difference between it and the next lowest energy level and is the order of 1 μs [40]. When the gap between energy levels is too great for multi-phonon emission relaxation, radiative decay dominates. For a silicate glass host this occurs for transitions with an energy greater than 5000 cm^{-1}.

A simplified energy level diagram for Nd^{3+} is shown in figure 2.3.

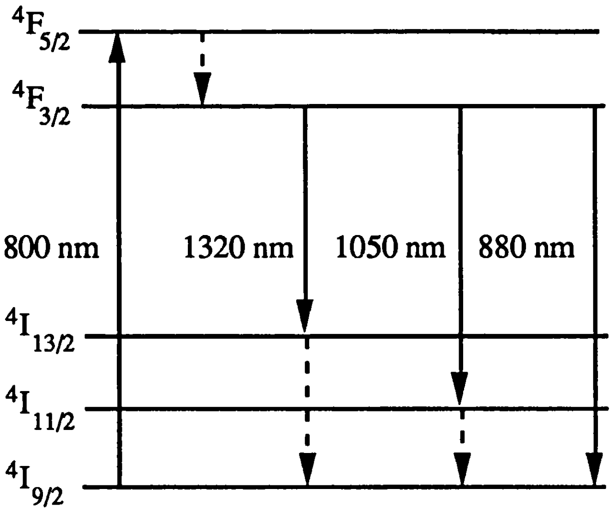

Figure 2.3 Optical transitions and energy level diagram for Nd^{3+}

Nd^{3+} in the $^4I_{9/2}$ ground state may be optically pumped or excited to the $^4F_{5/2}$ state by the absorption of 800 nm radiation. The ion first loses energy to the host lattice by a rapid non-radiative decay to the $^4F_{3/2}$ energy level. The energy gap between the $^4F_{3/2}$ state to the next lowest energy state is too large for non-radiative decay to dominate and consequently the lifetime of the $^4F_{3/2}$ is long relative to the $^4F_{5/2}$ state. Radiative decay from the $^4F_{3/2}$ is also partially forbidden and the state is termed a metastable state, as the ion resides in the state for a relatively long time. The lifetime of the metastable state is approximately 450 μs in a silica glass host. Decay from the metastable level occurs by radiative emission at 1.32 μm to the $^4I_{13/2}$ state, at 1.06 μm to the $^4I_{11/2}$ state and at 0.9 μm to the $^4I_{9/2}$ ground state. The wavelength of the fluorescence bands and their relative intensities is dependent on the host glass composition [5]. The ion returns to the ground state from the lowest two excited states by fast non-radiative decay.

Nd^{3+} doped silica fibre lasers have been realised with all three transitions [41,42]. A population inversion is easily achieved in the four level laser system operating at 1.06 μm by pumping into the upper lasing level, the metastable $^4F_{3/2}$ state via the $^4F_{5/2}$ state, with stimulated emission occurring as the ions decay to the $^4I_{11/2}$ state, the population inversion accomplished by the rapid non-radiative decay from the lower lasing level to the ground state. Emission from the $^4F_{3/2}$ - $^4I_{13/2}$ transition was of interest for amplification in the second telecommunication window, but in silica glass excited state absorption (ESA) occurs for radiation in the band 1.32 μm-1.36 μm from the metastable state to a higher energy state. The ESA reduces the population of the metastable state and hence the stimulated emission rate. Therefore, interest has been shown in non-oxide host glasses where the problem of ESA is reduced [43] and other rare earth ions, such as Pr [44], for optical amplifiers and sources in the second telecommunication window.

Er^{3+} may be excited from the ground state by pumping at 807 nm to the $^4I_{9/2}$ state, at 980 nm to the $^4I_{11/2}$ state, or at 1480 nm directly into the metastable $^4I_{13/2}$ state. Non-radiative decay occurs to the metastable state, from which the ions decay to the $^4I_{15/2}$ ground state by radiative emission with the peak at 1540 nm. As Er^{3+} is a three level laser system the fluorescence band coincides with the absorption band. An energy level diagram for Er^{3+} is given in figure 2.4.

Er^{3+} doped silica lasers operating at 1540 nm are more difficult to attain as Er^{3+} is a three level laser system in which the lower lasing level is the ground state. In order to achieve a population inversion, more than half of the total Er^{3+} population must be excited to the metastable. The most popular pump bands are at 980 nm and 1480 nm, with the pump band at 800 nm, compatible with AlGaAs semiconductor diode pump sources, handicapped by ESA. In this case, the ESA is due to pump photons exciting ions in the metastable state, promoting the ions to a higher excited state which then ultimately decay back again to the upper lasing level by non-radiative processes, reducing the pump efficiency.

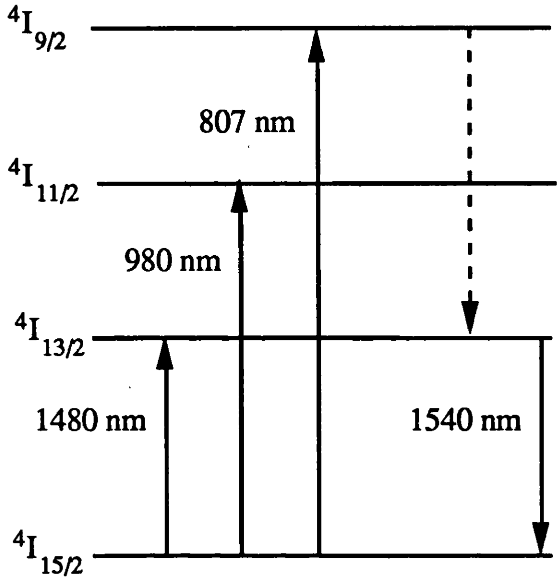

Figure 2.4 Optical transitions and simplified energy level diagram for Er^{3+}.

The host has two main influences on the spectroscopic properties of the rare earth ions: Stark splitting and the broadening of the energy levels.

As discussed earlier, Stark splitting arises from the ligand field which removes any degeneracy in the energy states. However, the 4f electrons are partially shielded from the ligand field and hence the perturbation is slight. Fluorescence and absorption spectra are temperature dependent as the population distribution in the Stark levels appears to be governed by Boltzmann statistics [45].

Broadening of the energy levels of the ions falls into two categories: homogeneous and inhomogeneous broadening. Homogeneous broadening affects all dopant ions by the same amount and is derived from phonon broadening, resulting from the creation or annihilation of a low energy phonon in a transition between two energy states. The phonon broadening is dependent on the temperature and on the glass host. Inhomogeneous broadening arises from each ion experiencing different environments and is due the perturbation of the energy levels by the crystal field which varies from site to site in the glass host. The extent and type of broadening is important as the gain is inversely proportional to the linewidth and the gain saturation is dependent on the broadening mechanism.

2.4.2 Rare Earth Concentration

Planar films fabricated by FHD aim to match as closely as possible the glass composition used for current "telecoms-type" optical fibres. For integrated optic waveguide lasers and amplifiers, the concentration of rare earth dopant must be higher than that found in fibre lasers and amplifiers, which is typically 10-1000 ppm, to overcome the higher losses and the shorter length of the active medium. Silica, although having many excellent properties, has the disadvantage that the solubility of rare earth ions in it is low, with the poor solubility being relieved by the addition of a few mole % P_2O_5 or Al_2O_3 [46]. The two major drawbacks associated with high rare earth doping levels are ion-ion interactions resulting in concentration quenching and cooperative upconversion and crystallisation within the glass matrix.

Concentration quenching involves non-radiative cross relaxation between closely spaced, neighbouring rare earth ions competing with radiative relaxation of the rare earth ions from the metastable state [47]. For Nd^{3+}, concentration quenching can be interpreted by non-radiative transfer of part of the energy from an ion in the metastable $^4F_{3/2}$ state to an adjacent ion in its ground state, dividing the excitation energy between the two ions quenching radiative decay from the metastable state, as shown in figure 2.5. Concentration quenching is evident in fluorescence lifetime measurements: a nonexponential decay which is independent of pump power as only one excited ion is requisite for the cross relaxation [48].

The second ion-ion interaction is cooperative upconversion which is illustrated in figure 2.6. This mechanism is evident in Er^{3+} doped silica, occurring when the metastable $^4I_{13/2}$ level is heavily populated at high pump powers, enabling an interaction between two adjacent ions involving the transfer of energy from one ion to another, the donor ion returning to the $^4I_{15/2}$ ground state and acceptor ion promoted to the $^4I_{9/2}$ state, with the acceptor ion finally returning to the $^4I_{13/2}$ by fast non-radiative decay. The net result is the decay of one of the excited ions in the metastable state to the ground state without the emission of a photon. The mechanism is dependent on pump power as it requires two excited interacting ions and manifests itself in radiative lifetimes reducing and becoming nonexponential with increasing pump powers. The nonexponential decay is due to the variation in coupling strengths between excited ions. The cooperative upconversion mechanism was confirmed by directly populating the $^4I_{13/2}$ metastable state with a pulse of radiation at 1.5 μm and noting that the upconverted fluorescence at 800 nm from the $^4I_{9/2}$ state exhibited the same decay kinetics as the square of the 1.5 μm fluorescence, indicating that the $^4I_{9/2}$ state is being populated from the $^4I_{13/2}$ state [49].

Pure silica can only incorporate very low doping levels of rare earth ions before the onset of microclustering and ion-ion interactions, with crystallisation occurring in the glass matrix at higher concentrations. Microclustering arises from the large cationic field strength of rare earth ions, precipitating the requirement of a coordination of a sufficiently high number of non-bridging oxygen ions to screen the rare earth ion. When rare earth ions are introduced into a highly rigid network, such as silica, they cannot sufficiently co-ordinate non-bridging oxygen ions, resulting in the rare earth ions to cluster, forming a cation rich phase sharing non-bridging oxygens. The onset of clustering in pure silica occurs for levels greater than 10^{19} cm^{-3} (0.1 wt%) for Nd^{3+} measured by fluorescence lifetime measurements [50] and for Er^{3+}, ion-ion interactions are evident for concentrations of 10^{18} cm^{-3}, revealed by fibre amplifier measurements [51].

However, the addition of Al_2O_3 and P_2O_5 has been found to retard clustering. Al codoping eliminates clustering by Al_2O_3 forming a solvation shell around the rare earth ion with the Al-O$^-$ groups co-ordinating the rare earth ion, with the resultant complex incorporated into the silica network [46]. The ratio of Al-to-rare earth ion of approximately 10 is found to prevent clustering. On codoping with P, the glass structure consists of SiO_4 and PO_4 tetrahedra incorporating the P=O bond, identified by Raman Spectroscopy. Also identified was the presence of non-bridging oxygens in SiO_4, Si-O$^-$, which allows the rare earth ion to be co-ordinated. Arai et al found a P-to-Nd^{3+} ratio of approximately 15 improved the solubility of Nd^{3+}. In contrast, it was found that P doping levels below 1 mole % give no major improvements in solubility for Nd^{3+} and concentrations must be kept below 10^{18} cm^{-3}. For very high rare earth doping levels a P and rare earth rich crystalline precipitate is formed [52].

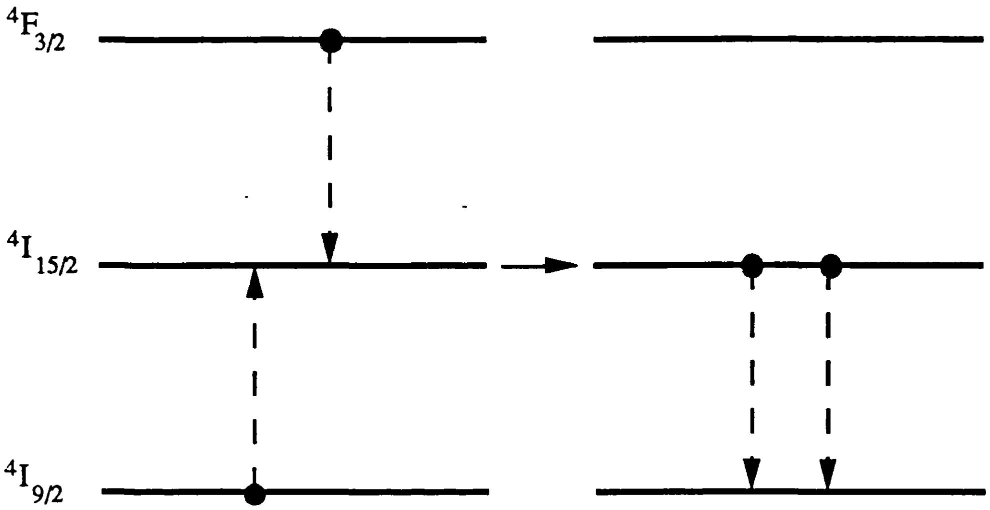

Figure 2.5 Schematic of concentration quenching effect for Nd^{3+}.

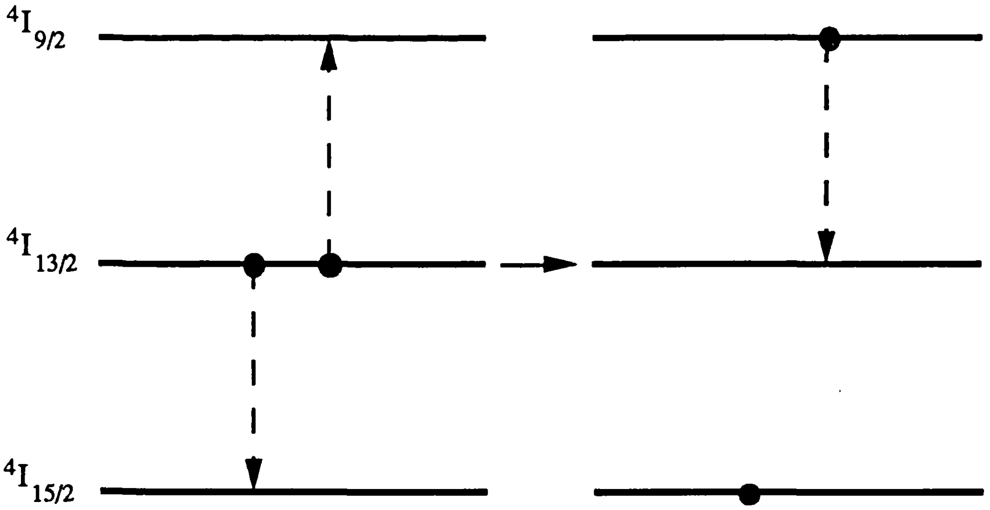

Figure 2.6 Schematic of co-operative upconversion mechanism affecting Er^{3+}.

2.5 Theoretical Analysis of Waveguide Lasers

The operation of rare earth waveguide oscillators and amplifiers has been analysed by many authors [53-57]. The model used in this study to describe an end-pumped four level laser system, suitable to analyse Nd^{3+} doped silica waveguide lasers and amplifiers, was that proposed by Digonnet [58].

Digonnet described in closed form expressions the gain, threshold and conversion efficiency of a waveguide laser as function of the interaction of the signal and pump modes, waveguide and material parameters. For a four level laser system of length L, which is end-pumped by an optical beam of wavelength λ_p, the interaction between the pumping rate per unit volume r(x, y, z), the population inversion density n(x, y, z) and the signal photon density of the ith mode $s_i(x, y, z)$, is described by the rate equations which may be written in a steady state as:

$$\frac{dn(x,y,z)}{dt} = r(x,y,z) - \frac{n(x,y,z)}{\tau_f} - \frac{c\sigma\, n(x,y,z)}{n_1} \sum_{j=1}^{N} s_j(x,y,z) = 0 \qquad (2.3)$$

$$\frac{ds_i}{dt} = \frac{c\sigma}{n_1} \int_{cavity} n(x,y,z) s_i(x,y,z) dV - \frac{c\delta_i}{2Ln_1} s_i = 0 \qquad (2.4)$$

where:

c = velocity of light

n_1 = laser medium refractive index

τ_f = fluorescence lifetime

σ = effective stimulated emission cross section

δ_i = round-trip loss for the ith mode

The summation in equation 2.3 is carried over the N transverse modes present in the cavity.

In the above equations, it was assumed that the gain medium is placed in a relatively high-Q cavity and the spontaneous emission was also ignored in equation 2.4, as its contribution to the output above threshold is negligible.

Distribution functions $r_o(x, y, z)$ and $s_{o,i}(x, y, z)$, normalised to unity over space, may be introduced such that:

$$r(x, y, z) = R\, r_0(x, y, z) \tag{2.5}$$

$$s_i(x, y, z) = S_i\, s_{o,i}(x, y, z) \tag{2.6}$$

where R is the pumping rate and S_i is the total number of signal photons in the i^{th} mode. Solving equation 2.3 for n(x, y, z) and inserting the result in equation 2.4, gives an expression for the steady state number of signal photons S_i:

$$J_i(S_1, S_2, \ldots, S_N) = \frac{\delta_i}{2L\sigma\tau_f R} \tag{2.7}$$

$$J_1(S_1) = \int_{cavity} \frac{s_{o,1}(x,y,z) r_0(x,y,z)}{1 + \frac{c\sigma\tau_f}{n_1} \sum_{j=1}^{N} S_j s_{o,j}(x,y,z)} dV \tag{2.8}$$

Letting $S_2 = S_3 = \ldots S_N = 0$, indicating single mode operation, resulting from gain competition limiting the number of oscillating modes, equations 2.7 and 2.8 may be rewritten:

$$J_1(S_1) = \frac{\delta_1}{2L\sigma\tau_f R} \tag{2.9}$$

$$J_1(S_1) = \int_{cavity} \frac{s_{o,1}(x,y,z) r_0(x,y,z)}{1 + \frac{c\sigma\tau_f}{n_1} S_1 s_{o,1}(x,y,z)} dV \tag{2.10}$$

where $J_1(S_1) = J_1(S_1, 0, 0, \ldots, 0)$.

The pumping rate required to reach threshold is determined by setting $S_1 = 0$ into equations 2.9 and 2.10. By definition the pump rate $R = P_{abs}/h\upsilon_p$, therefore the absorbed pump power required to reach threshold is :

$$P_{th} = \frac{h\upsilon_p}{\sigma\tau_f} \frac{\delta_1}{2L} \frac{1}{J_1(0)} \tag{2.11}$$

where:

$$J_1(0) = \int_{cavity} r_o(x, y, z) s_{o, 1}(x, y, z) dV \tag{2.12}$$

$LJ_1(0)$ can be redefined as follows:

$$A_p^* = \frac{1}{LJ_1(0)} = \frac{A_f}{F_{\nu\mu nm}} \tag{2.13}$$

where: A^*_p = effective pump area

A_f = effective core area

$F_{\upsilon\mu nm}$ = filling factor where the index pairs (υ, μ) and (n, m) characterise the signal and pump modes respectively.

Taking into account that there are significant propagation losses at the pump wavelength α_r and that for an end pumped device, P_{th} is related to the incident pump power P_p by:

$$P_{th} = P_p[1 - \exp(-(\alpha_r + \alpha_p)L)] \tag{2.14}$$

where α_p is the absorption loss at pump wavelength, then the incident pump power required to reach oscillation threshold can be written as:

$$P_p = \frac{\alpha_p + \alpha_r}{\alpha_p} \frac{h\upsilon_p}{2\sigma\tau_f} \frac{A_f}{F_{\upsilon\mu nm}} \frac{\delta_1}{1 - \exp[-(\alpha_p + \alpha_r)L]} \tag{2.15}$$

From equation 2.15, it can be deduced that the lasing threshold is dependent on: the propagation loss at the pump and lasing wavelengths; the reflectivity of the mirrors in a low diffraction loss laser cavity; the spatial overlap of the signal and pump modes; and the waveguide area, the lasing threshold reducing for a decreasing area due to the increase in power density in the cavity [59].

2.6 Planar Waveguide Lasers and Amplifiers

Recently there has been growing interest in rare earth doped planar waveguide lasers and amplifiers, enabling monolithic integration of active and passive optical functions. Rare earth doped channel waveguide lasers and amplifiers have been formed in glasses, in lithium niobate and in other crystals. Development of such technology enables active functions in glasses which were previously regarded as only being able to provide passive optical functions and enables the combination of an integrated laser source with the electrooptic, acoustooptic and non-linear properties of $LiNbO_3$ and other crystals. Moreover, the planar geometry makes possible the integration of optical sources and amplifiers, splitters, modulators, ring resonators, wavelength multiplexers and other optical circuits, which cannot be realised by optical fibre devices.

This section reviews the recent progress achieved with emphasis placed on results reported for planar glass devices fabricated by FHD for a potential application as integrated optical light sources and amplifiers in the third telecommunication window.

The first operation of a continuous wave (CW) Nd^{3+} doped silica optical waveguide laser on a silicon substrate fabricated by FHD and solution doping was reported in 1989 [60]. The Nd^{3+} concentration was about 2000 ppm and the propagation loss near 1.05 μm for a 20 μm wide guide formed by reactive ion etching (RIE) was 0.85 dB/cm. Pumped at a 800 nm using a Ti: Al_2O_3 laser, pump power threshold for CW lasing at a wavelength of 1.0515 μm for the 5 cm long waveguide was 150 mW. Pump power input to the waveguide and lasing output detection were carried out using single-mode optical fibres with a cutoff wavelength of 1.3 μm. The fibres had a dielectric mirror directly deposited onto the endfaces and were butted up against the waveguide. The input mirror had a high reflectivity (R=99%) at the lasing wavelength and high transmission (T=99%) at the pumping wavelength. The output mirror had R=95% at the lasing wavelength. The low slope efficiency of 0.12% and high pump threshold were due to the scattering loss at pumping and lasing wavelengths induced by the clustering of Nd^{3+}; the multimode nature of the waveguide resulting in a low transfer rate of pump power; and the optical loss caused by butting the optical fibres, acting as mirrors, against the waveguide.

Laser diode pumping of Nd^{3+} doped silica was later achieved by dramatically reducing the pumping power required to reach lasing threshold by reducing the scattering loss through improvements in the fabrication technique, depositing dielectric mirrors on each waveguide endface and increasing the power density in the cavity by reducing the waveguide width [59]. The multi-mode waveguides were 4 cm long and 6-30 μm wide, with a core thickness of 6 μm and an index difference of the core with respect to the cladding of 0.5 %. The concentration of Nd^{3+} in the waveguide was estimated to be 2000 ppm. For identical mirror reflectivities to those reported earlier, a minimum pump power threshold of 25 mW was achieved in a waveguide with a 8 μm wide core. A slope efficiency of 1.2 % was attained by pumping at 805 nm using AlGaAs laser diodes, giving a maximum output power of 300 μW. The performance of the Nd^{3+} doped SiO_2-P_2O_5 planar waveguide lasers achieved by the author and described in detail in chapter 5 compares favourably with the characteristics of the laser discussed above.

A Nd^{3+} doped silica glass waveguide laser deposited on a silica substrate fabricated by FHD using chelates has also been demonstrated [61]. The rare earth was introduced into the glass during the fabrication process by the vapour phase transport of neodymium chelate of 2, 2, 6, 6-tetramethyl -3, 5-heptanedione [$Nd(thd)_3$], resulting in a Nd^{3+} doping level of 0.7 wt%. The silica glass was co-doped with Al_2O_3 which acted to increase the refractive index of the waveguide region and to serve as a homogenizing agent enabling a higher concentration of rare earth to be incorporated into the glass matrix. Pumped at 807 nm using a Ti: Al_2O_3 laser, CW lasing at 1062 nm was achieved with a pump power threshold of 143 mW, with a slope efficiency of 2.1 %.

Of even greater significance was the report of the first demonstration of an Er^{3+}-doped glass planar waveguide fabricated by FHD and RIE [62]. A high doping concentration of 8000 ppm in the SiO_2-P_2O_5 host glass was required to enable CW lasing with a short cavity length of 4.5 cm. The core layer was 6 μm thick and 25 μm wide, with a refractive index difference to the cladding layer of 0.75 %. The scattering loss of the waveguide was less than 0.1 dB/cm, with no increase in the scattering loss in the shorter wavelength region, indicating homogeneous distribution of Er^{3+} in the core glass. Dielectric mirrors were again deposited onto the end faces of the waveguide to form a Fabry-Perot cavity. The input mirror had a high reflectivity (R=99.9%) at the lasing wavelength around 1.6 μm and high transmission (T=98%) at the pumping wavelength. The output mirror had R=99% at the lasing wavelength and T=98% at the pumping wavelength. Pumping was carried out at 980 nm using a Ti: Al_2O_3 laser. The incident pump power threshold and slope efficiency were 49 mW and 0.81 %, respectively. Multi-mode oscillation occurred around 1.598 μm and 1.604 μm, although the fluorescence peak was at 1.535 μm. The difference between the lasing wavelength and the fluorescence peak was thought to be due to the reabsorption of the emission at 1.535 μm in the three level laser system.

However, to construct compact and functional devices, it is essential to integrate the waveguide laser with passive optical functions, but the presence of external mirrors or the direct coating of a dielectric mirror at each end of the substrate to provide the necessary feedback for laser action makes integration difficult. One such solution for monolithic integration was reported when oscillation was achieved for the first time in an Er^{3+}-doped silica-based waveguide ring resonator fabricated by FHD and RIE [63].

The resonator consisted of a wavelength division multiplexing (WDM) coupler and an intersection. The resonator length was 9.2 cm, which corresponds to a free spectral range (FSR) of 2.2 GHz. The buried waveguide core had a cross-section 8 μm wide and 7 μm thick, with a refractive index difference between the core and the cladding layer of 1.3 %. The power coupling ratio of the WDM coupler was 72%, with an excess loss of 0.2 dB at 1.535 μm and 30 % at 980 nm, respectively.

TM-polarisation oscillation occurred at 1.536 μm with a full width at half maximum (FWHM) of 0.3 nm, when pumped at 980 nm with a Ti: Al_2O_3 laser. The spacing of the longitudinal modes was measured to be 2.2 GHz, equal to the FSR and the average linewidth of the modes was 200 KHz. The lasing threshold for the pump power and the slope efficiency were 250 mW and 1.1 %, respectively.

As discussed, Nd^{3+} and Er^{3+} doped silica planar waveguides have received considerable attention, but it can be argued that semiconductor lasers are superior in terms of performance and convenience of use. The true potential of planar rare earth doped glass waveguides then lies in their application as integrated optical amplifiers with high gain and a high output power, enabling, for example, transparent splitters.

Er^{3+} doped SiO_2-P_2O_5 waveguides fabricated by FHD have shown considerable promise for such applications [64]. For an Er^{3+} concentration of 0.55 wt%, with a 8 μm wide and 7 μm thick core and a refractive index difference between core and cladding of 1.2 %, a net gain of 13.7 dB was achieved in a 19.4 cm long waveguide with a pump power of 640 mW from a Ti: Al_2O_3 laser operating at 980 nm. As shown in figure 2.7, the 0 dB gain pump threshold was 25 mW, with a gain coefficient of 0.65 dB/cm.

To achieve a high degree of integration though, it is essential that laser diodes be used to pump integrated optical devices. This was achieved by pumping an Er^{3+} doped SiO_2-P_2O_5 waveguide with high power strained InGaAs quantum well laser diodes emitting at 980 nm [65]. The waveguide was again 8 μm wide and 7 μm thick and s-shaped to give a 23 cm length in an area of 7.9 x 3.5 cm^2, on a silicon substrate. The loss of the Er^{3+}-doped waveguide at 1.3 μm and 1.535 μm was 0.15 dB/cm and 0.90 dB/cm, respectively.

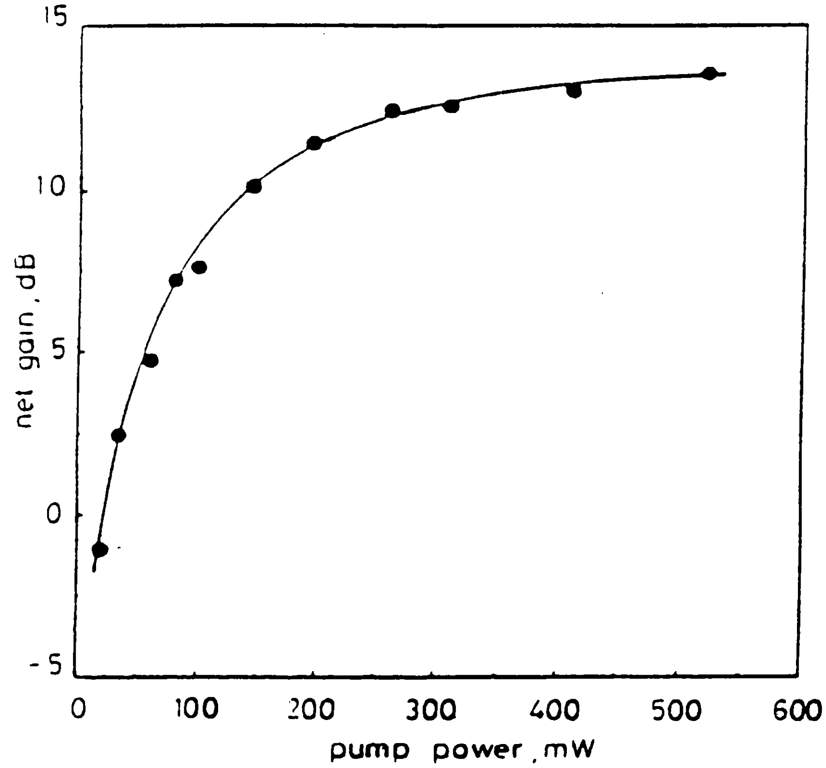

Figure 2.7 Amplification power charateristics of 19.4 cm long Er^{3+}-doped silica-based waveguide, taken from reference 64.

The pump source used was composed of 2 laser diode submodules, a polarisation multiplexing submodule and a wavelength multi/demultiplexing (WDM) submodule. The pump and signal light were multiplexed by the WDM submodule which contained a dielectric mirror. The laser diode modules provided a total pump power of 99 mW through a single-mode fibre, from which a maximum net signal gain of 9.4 dB was attained. The threshold pump power to acquire the net gain was 27 mW. The relationship between the output signal power at a pump power of 68 mW and the signal gain of the waveguide amplifier is shown below in figure 2.8. The small signal gain was 7.4 dB and the saturated output power was approximately -2.1 dBm. Theoretical analysis has shown that the amplification characteristics may be improved further by increasing the confinement of the pump and signal modes and increasing the length of the waveguide for a given pump power [66].

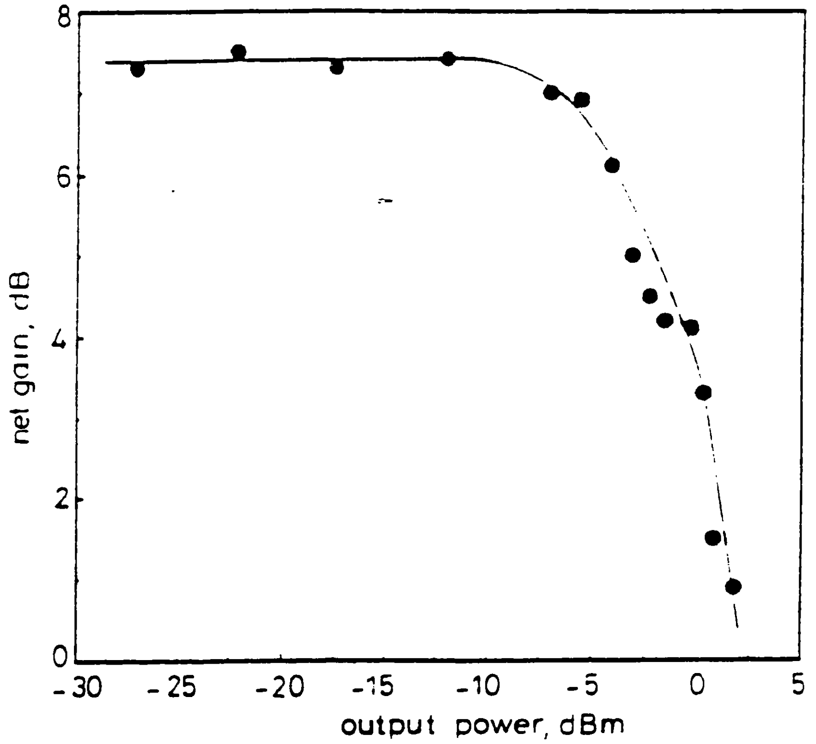

Figure 2.8 Signal gain at 1.535 μm of Er^{3+}-doped silica-based waveguide as function of output signal power at 68 mW launched pump power, taken from reference 65.

Er^{3+} doped planar waveguides on silicon substrate have also been fabricated by plasma enhanced chemical vapour deposition (PECVD) [67], electron-beam vapour deposition (EBVD) [68], implantation of MeV Er ions [69-71] and sputter deposition techniques [72].

A maximum net gain of 5 dB and a gain coefficient of 0.67 dB/cm were obtained in a 0.48 wt% Er^{3+} doped waveguide fabricated by PECVD and RIE, pumped with 420 mW at a wavelength of 980 nm. The Er^{3+} doped phosphosilicate glass waveguide had a similar gain coefficient and threshold as Er^{3+} doped silica based waveguides fabricated by FHD.

Using EBVD, a single-transverse mode Er^{3+} doped SiO_2-GeO_2 glass waveguide laser operating at 1.53 μm was achieved. The core was 10 μm wide, 8 μm high and 64.5 mm long. The threshold pump power for CW oscillation was between 150 and 200 mW when pumped at 980 nm.

Doping of silica and phosphosilicate glass films by implantation of MeV Er ions has also been studied. Implantation energies and fluences ranged from 500 KeV to 3.5 MeV and 3.8 x 10^{15} to 9 x 10^{16} ion/cm^2, respectively. After thermal annealing, the implanted films showed an intense and sharply peaked fluorescence spectrum near 1.54 µm. Thermal annealing was found to reduce the beam-induced defects in silica and increase the fluorescence intensity and lifetime from 6 to 15 ms. This was attributed to an increase in the number of optically active Er^{3+}. Non-radiative relaxation was evident for Er^{3+} concentrations in the order of 1 mole%.

To form ultrashort length integrated amplifiers, an increase in Er^{3+} doping levels is required, without the detrimental effect of decreased luminescence efficiency. One such promising technology is highly Er^{3+} doped sodium calcium silicate glass waveguides on silicon substrate. Planar films 1.3 µm thick were fabricated by RF sputtering from $(SiO_2)(Na_2O)_{0.2}(CaO)_{0.17}Er_{0.028}$ glass targets. Ridge waveguides 6 µm wide were formed by ion-beam sputtering, giving a scattering loss of ~ 1 dB/cm when clad with silicone gel. The peak absorption at 1.53 µm was measured to be 8.5 dB/cm. Gain measurements were carried out on a 2.4 cm long waveguide by pumping at 975 nm using a Ti: Al_2O_3 laser. A 21 dB enhancement in signal output at 1.53 µm was observed for a pump power of 120 mW. However, the net gain for the device was 0 dB and the pump efficiency was reduced by upconversion of the pump radiation, manifested by green light emitted from the pumped waveguide.

Ion-exchange in glass is a mature, flexible technique used for the formation of planar waveguide devices [73]. This technique has been applied, with great success, to realise integrated optic waveguide lasers and amplifiers in several Nd^{3+} and Er^{3+} doped glasses. An advantage of this technology is the high doping level of the rare earth ion in the host glass that can be achieved without phase separation and consequential devitrification.

Laser oscillation at 906, 1057 and 1358 nm has been achieved in the same Nd^{3+} doped phosphate based glass integrated optic laser [74]. The low loss channel waveguides were formed in the phosphate glass by ion-exchange from a silver film. The 1.4 cm long device was pumped using a Ti: Al_2O_3 laser. The lasing threshold for 906 nm emission was 170 mW of absorbed pump power. The threshold for 1057 nm emission was 12 mW of absorbed pump power using a 4 % transmitting output coupler. A 56 % slope efficiency was achieved at 1057 nm when using a 20 % transmitting output coupler. The maximum output power at 1057 nm was 210 mW. The threshold for 1358 nm emission was 52 mW of absorbed pump power.

Extended-cavity operation of Nd^{3+} doped glass waveguide lasers has also been demonstrated [75]. Channel waveguide lasers were fabricated in Nd^{3+} doped mixed alkali glass using field assisted ion-exchange, yielding slope efficiencies of 4-11 %, with pump thresholds of 20 mW. Lasing occurred at 1057 nm. Active mode locking of the extended-cavity integrated optic laser, achieved using an inter-cavity standing-wave acousto-optic deflector driven at 50 MHz, produced pulse widths of approximately 80 ps FWHM. Q-switching was performed using a linear polariser and a bulk $LiNbO_3$ electro-optic modulator inserted into the cavity. For an absorbed pump power of 118 mW, pulses produced were 75 ns FWHM with a peak power of 1.2 W. The CW output narrowed from 4 nm FWHM to 7 GHz and was tunable over 24 nm when a grating was used as a feedback element, reducing to single-frequency operation when a high-reflectivity etalon was inserted into the cavity. However, Q-switching of planar waveguide lasers using a bulk modulator in an extended-cavity configuration has the disadvantages of fresnel reflections between guided and bulk components and the loss of ruggedness and stability of an integrated waveguide laser.

Utilising the same field assisted ion-exchange and Nd^{3+} doped mixed alkali glass, a Y-branch waveguide laser and amplifier was achieved [76].The overall length of the device was 24 mm. The laser cavity was formed by bonding mirrors to the polished end facets. The lasing threshold was 26 mW of absorbed pump power, giving a slope efficiency of 5 %, when a 4 % transmitting output coupler was used. When investigated as an amplifier, a small signal gain of 0.034 dB/mW was achieved, with the 3 dB splitting loss of the Y-branch structure overcome for an absorbed pump power of 85 mW. Potentially, the 1 x 2 geometry could be extended to a large number of output ports forming the basis for splitters, where the splitting losses can be compensated. Moreover, linewidth narrowing in an imbalanced Y-branch waveguide laser was achieved [77]. An extended cavity was used to imbalance the arms by a ratio of 2.8:1. The subsequent linewidth was measured to be 3.7 GHz FWHM, compared to linewidths of 3-4 nm for single channel waveguide Fabry-Perot lasers.

Low threshold monomode waveguide lasers have been formed in Nd^{3+} doped BK-7 glass using potassium ion-exchange [78]. With a 2 wt % Nd_2O_3 doping level, the threshold for lasing was 7.5 mW pumped at 807 nm, with a slope efficiency of 6 %. The lasing wavelength was 1058 nm. A monolithic integrated Q-switched laser was achieved by using rapid variation of the path difference between the cavities of the multiple-cavity resonator [79]. In this case, a thermooptic phase modulator was used to switch the cavity loss of the Y-junction glass waveguide laser between high and low states. Q-switched pulses of duration of 5 μs and peak powers of 70 mW were obtained. Moreover, Er^{3+} doped potassium ion-exchanged waveguide lasers in BK-7 glass have been demonstrated [80]. Operating at 1544 nm, the lasing threshold was approximately 150 mW when pumped at 980 nm and exhibited a slope efficiency of 0.55 %, with respect to launched pump power. The doping level was 0.5wt% Er_2O_3. However, a disadvantage of the Er^{3+} doped ion-exchanged glass is that Er^{3+} is a 3-level laser system and that the signal may be absorbed by ions in the ground state outside the channel waveguide, excited by the evanescent field, thus increasing the pump power required to reach lasing threshold. This problem may be rectified by selective area doping of the ion-exchanged channel waveguides with Er by ion implantation [81].

A maximum output power greater than 150 mW has been reported from Nd^{3+} doped LHG-5 glass channel waveguides [82]. Using a field enhanced silver ion-exchange technique, multimode waveguides with a radius up to 215 µm were formed. The waveguides with a 3.3 wt % Nd^{3+} doping level were pumped using an AlGaAs laser diode operating at 802 nm. Lasing occurred at 1054 nm, with a pump threshold of 170 mW, giving a slope efficiency of 45 %. The Nd^{3+} doped LHG-5 glass amplification charateristics were also investigated at 1054 nm [83]. The cross-section of the 10 mm long, buried waveguide was elliptical: the short and long axes were 17 and 33 µm, respectively. A gain of 3.4 dB at 1054 nm with a gain coefficient of 0.027 dB/mW was achieved when pumped at 514 nm using an argon ion laser, the efficiency increasing to 0.079 dB/mW when pumped at 808 nm using a diode laser. Oscillation was also achieved at 1.325 µm and 1.355 µm using the same Nd^{3+} doped phosphate glass composition [84]. The cross-section of the waveguide used in this case was semicircular, with a radius of approximately 90 µm. The waveguide length was 5 mm. When pumped at 802 nm using a AlGaAs laser diode, threshold was achieved at both 1.325 µm and 1.355 µm for a pump power of 33 mW. The slope efficiencies were 0.77 and 0.92 %, respectively, for an output coupler with a reflectivity of 99.7 % at the lasing wavelength.

Potentially, the most important development for planar waveguide lasers was the first demonstration of a Nd^{3+} doped glass channel waveguide laser containing an integrated Bragg reflector [85]. Silver ion exchange was used to form the waveguides in the Nd^{3+} doped soda-lime silicate glass. First order gratings were defined in photoresist on the glass surface using a holographic technique and subsequently etched into the waveguide using an argon ion mill. The grating structure was 5.5 mm long, had a period of 0.35 µmn and had an etch depth of 60 nm. The peak reflectivity was approximately 90 %. Oscillation occurred in a single longitudinal mode with a linewidth of approximately 500 MHz. Pump power threshold and slope efficiency were 50 mW and 1 %, respectively.

Efficient CW emission from Nd^{3+} doped $MgO:LiNbO_3$ waveguide lasers has been reported as well. Operating at 1.085 µm, thresholds as low as 1.5 mW and slope efficiencies of 34 % have been achieved, with semiconductor diode pumping demonstrated [86]. An efficient monolithic Q-switched Nd^{3+} doped $MgO:LiNbO_3$ waveguide laser operating at 1.085 µm was also realised [87]. Q-switched pulses of 350 W peak power and 300 ps duration were obtained for 15 mW of pump power. The signal produced was frequency-doubled in an external quasiphase-matched $LiNbO_3$ waveguide giving 12 W pulses at 540 nm with a 15 % conversion efficiency. Nd^{3+}-doped $Ti:LiNbO_3$ waveguide lasers formed by thermal diffusion of the Nd have been successfully demonstrated as well [88]. The absorbed pump power threshold was measured to be 13 mW at 814 nm, with a slope efficiency of 55% and a maximum output power in excess of 100 mW, with feedback provided only by the intrinsic Fresnel reflections at the end faces. CW Er^{3+} doped $Ti:LiNbO_3$ channel waveguide lasers have been fabricated by an indiffusion of Er^{3+} prior to channel fabrication by Ti diffusion [89]. Pumped at 1.477 µm, CW operation at 1.532 µm, with a threshold of 8 mW absorbed pump power was achieved. The slope efficiency was 0.4 %.

Ion-implanted Nd:YAG waveguide lasers have also shown promising results. Ion-implanted planar waveguides were formed by using high energy He^+ ions, resulting in propagation losses of approximately 1 dB/cm. Absorbed pump power threshold for the planar waveguide laser was 10.5 mW, pumped at 590 nm [90]. Channel waveguide lasers showed a 20 times reduction in pump power threshold as compared to the planar waveguide, with absorbed pump power thresholds as low as 500 µW using a GaAlAs diode laser. Output slope efficiencies of 29 % have also been demonstrated [91,92]. Futher improvements in the fabrication conditions could lead to further reductions in threshold and enable tunable lasers in such materials as $Ti:Al_2O_3$, $Cr:BeAl_2O_4$ and various other Cr doped garnets. The first report of optical gain in Cr-doped material indicated the potential of diode laser pumping of an integrated, broadband tunable laser source [93]. Optical amplification was measured in proton-exchanged $Cr:LiNbO_3$ channel waveguides, giving the possibility of a tunable laser in the 750-1150 nm spectral range.

2.7 Conclusion

The spectroscopy of rare earth doped glass has been studied for many decades, but it is only recently that interest has been shown in the subject for application in future all-optical communication networks. In particular, Er^{3+} doped silica fibre amplifiers have been exploited as optical amplifiers in the third telecommunication window. However, there is limited opportunity for complex circuitry combining active and passive regions, dictated by the fibre dimensions.

In contrast, rare earth doped planar waveguides have a real potential for monolithic integration of active and passive optical functions. The technologies and materials used for the rare earth doped planar waveguides is diverse, with high-silica planar waveguides on silicon substrate fabricated by FHD producing waveguides most compatible with silica optical fibres. Compact planar waveguide lasers and amplifiers have been demonstrated, with potential major applications in telecommunications, computer and sensor networks.

2.8 References

1. Patek, K.
Glass Lasers
Butterworth and Co. Ltd., 1970.
2. Judd, B. R.
Phys. Rev., 1962, **127**, 750.
3. Ofelt, G. S.
J. Chem. Phys., 1962, **37**, 511.
4. Dieke, G. H.
Spectra and energy levels of rare earth ions in crystals.
J. Wiley and Sons, 1968.
5. France, P. W. (Ed)
Optical Fibre Lasers and Amplifiers
Blackie Publishers, 1991.
6. Urquhart, P.
Proc. IEE J, 1988, **135**, 385.
7. Koester, C. J., and Snitzer, E.
Appl. Opt., 1964, **3**, 1182.
8. Stone, J., and Burrus, C. A.
Appl. Opt., 1974, **13**, 1256.
9. Poole, S. B., Payne, D. N., and Fermann, M. E.
Elecron. Lett., 1985, **21**, 737.
10. Mears, R. J., Reekie, L., Poole, S. B., and Payne, D. N.
Elecron. Lett., 1985, **21**, 738.
11. Mears, R. J., Reekie, L., Poole, S. B., and Payne, D. N.
Elecron. Lett., 1986, **22**, 159.
12. Mears, R. J., Reekie, L., Jauncey, I. M., and Payne, D. N.
Elecron. Lett., 1987, **23**, 1026.
13. Poole, S. B., Payne, D. N., Mears, R. J., Fermann, M. E., and Laming, R. I.
J. Lightwave Techn., 1986, **4**, 870.
14. Millar, C. A., Miller, I. D., Ainslie, B. J., Craig S. P., and Armitage, J. R.
Electron. Lett., 1987, **23**, 865.
15. Barnes, W. L., Poole, S. B., Townsend, J. E., Reekie, L., Taylor, D. J., and Payne, D. N.
J. Lightwave Techn., 1989, **7**, 1461.
16. Hanna, D. C., Kazer, A., Philips, M. W., Sheperd, D. C., and Suni, P. J.
Electron. Lett., 1989, **25**, 95.

17. Reekie, L., Mears, R. J., Poole, S. B., and Payne, D. N.
J. Lightwave Techn., 1986, **4**, 956.

18. Millar, C. A., Miller, I. D., Mortimore, D. B., Ainslie, B. J., Craig S. P., and Urquhart, P.
IEE Proc., Pt. J, 1988, **135**, 303.

19. Schmuck, H., Pfeiffer, Th., and Veith, G.
Electron. Lett., 1991, **27**, 2117.

20. Cowlie, G. C., Payne D. N., and Reid, D.
Electron. Lett., 1991, **27**, 229.

21. Zyskind, Z. L., Sulhoff J. W., Sun, Y., Stone, J., Stulz, L. W., Harvey, G. T., DiGiovanni, D. J., Presby, H. M., Piccirilli, A., Koren, U., and Jopson, R. M.
Electron. Lett., 1991, **27**, 2148.

22. Ainslie, B. J., Craig-Ryan, S. P., Davey, S. T., and Wakefield, B.
J. Lightwave Techn., 1988, **6**, 287.

23. Devlin, W. J., Cooper, D. M., Spurdens, P. C., Sherlock, G., Bagley, M., Regnault, J. C., and Elton, D, J.
IEEE InP and Related Compounds Conference, Denver.

24. Stolen, R. H.
Optical Fibre Telecommunications
New York: Acedemic, 1979.

25. Nakagawa. K., Nishi, S., Aida, K., andYoneda, E.
J. Lightwave Techn., 1991, **9**, 198.

26. Stone, J., and Burrus, C. A.
Appl. Phys. Lett., 1973, **23**, 388.

27. Townsend, J. E., Poole, S. B., and Payne, D. N.
Electron. Lett., 1987, **23**, 329.

28. Gozen, T., Kikukawa, Y., Yoshida, M., Tanaka, H., and Shintani, T.
Paper no. WQ1 in Technical Digest of Optical Fiber Communications Conference (New Orleans, LA). Optical Society of America, Washington, DC, 1988.

29. Ainslie, B. J., Craig, S. P., Davey, S. T., and Wakefield, B.
Proc. ECOC '88, IEE Pubn. 292, 1988.

30. Ainslie, B. J., Armitage, J. R., Craig, S. P., and Wakefield, B.
Mater. Lett., 1988, **6**, 139.

31. Morse, T. F., Kilian, A., and Reinhart, L.
J. Non-Cryst. Solids, 1991, **129**, 93.

32. Sanada, R., Shioda, T., Moriyama, T., Inada, R., Takahashi, S., and Kawachi, M.
European Conference on Optical Communications, York, 1980.

33. Takahashi, S., Sanada, K., Inada, K., and Fukada, O.
United States Patent, no. 4, 336, 049, June 22, 1982.

34. Takahashi, S., Sanada, K., Inada, K., and Fukada, O.
United States Patent, no. 4, 338, 098, June 14, 1983.

35. Ainslie, B. J., Craig, S. P., Davey, S. T., and Wakefield, B.
Mater. Lett., 1987, **5**, 143.

36. MacChesney, J. B., and Simpson, J. R.
Paper no. WH5 in Technical Digest of Optical Fiber Communications Conference (San Diego, CA). Optical Society of America, Washington, DC, 1985.

37. Amano. S., Yamashita, T., Tajima, H., Masuda, I., and Izumitani, T.
European Conference on Optical Communications, Helsinki, 1987.

38. Snitzer, T.
Appl. Opt., 1966, **5**, 1487.

39. Sandoe, J. N., Sarkies, P. H., and Parke, S.
J. Phys. D: Appl. Phys., 1972, **5**, 1788.

40. Reisfeld, R., and Jorgensen, C. K.
Lasers and Excited States of Rare Earths.
Inorganic Chemistry Concepts 1, Springer Verlag, 1977.

41. Alcock, I. P., Ferguson, A. I., Hanna, D. C., and Tropper, A. C.
Optics. Lett., 1986, **11**, 709.

42. Hakimi, F., Po, H., Tumminelli, R., McCollum, B. C., Zenteno, L., Cho, N. M., and Snitzer, E.
Optics. Lett., 1989, **14**, 1060.

43. Brierley, M., Carter, S., France, P., and Pendersen, J. E.
Electron. Lett., 1990, **26**, 329.

44. Miyajima, Y., Sugawa, T., and Fukasaku, Y.
Electron. Lett., 1991, **27**, 1706.

45. Millar, C. A., Whitley, T. J., and Fleming, S. C.
Proc. IEE J, 1990, **137**, 155.

46. Arai, K., Namikawa, H., Kumata, K., and Honda, T.
J. Appl. Phys., 1986, **59**, 3430.

47. Stroud, J. S.
Appl. Opt, 1968, **7**, 751.

48. Ainslie, B. J., Craig, S. P., and Wyatt, R.
Mater. Lett., 1989, **8**, 204.

49. Ainslie, B. J., Craig-Ryan, S. P., Davey, S. T., Armitage, J. R., Atkins, C. G., Massicott, J. F., and Wyatt, R.
IEE Proc., Pt. J, 1990, **137**, 205.

50. Namikawa, K., Kazou, A., Kumata, K., Ishii, Y., and Tanaka, H.
Jpn. J. Appl. Phys., 1982, **21**, L360.

51. Shimizu, M., Yamada, M., Horiguchi, M., and Sugita, E.
IEEE Photon. Technol. Lett., 1990, **2**, 43.

52. B. J. Ainslie.
J. Materials Sci. Lett., 1987, **6**, 1361.

53. Desurvire, E., Simpson, J. R., and Becker, P. C.
Opt. Lett., 1987, **12**, 888.

54. Morkel, P. R., and Laming, R. I.
Opt. Lett., 1987, **14**, 1062.

55. Armitage, J. R.
Appl. Opt., 1988, **27**, 4831.

56. Digonnet, M. J. F.
IEEE J. Quantum Electron., 1990, **26**, 1788.

57. Ohashi, M.
J. Lightwave Techn., 1991, **9**, 1099.

58. Diggonet, M. J. F., and Gaeta, C. J.
Appl. Opt., 1985, **24**, 333.

59. Hattori, K., Kitagawa, T., Ohmori, Y., and Kobayashi, M.
IEEE Photon. Technol. Lett., 1991, **3**, 882.

60. Hibino, Y., Kitagawa, T., Shimizu, M., Hanawa, F., and Sugita, A.
IEEE Photon. Technol. Lett., 1989, **1**, 349.

61. Tumminelli, R., Hakimi, F., and Haavisto, J.
Opt. Lett., 1991, **16**, 1098.

62. Kitagawa, T., Hattori, K., Shimizu, M., Ohmori, Y., and Kobayashi, M.
Electron. Lett., 1991, **27**, 335.

63. Kitagawa, T., Hattori, K., Hibino, Y., Ohmori, Y., and Kobayashi, M.
Proc. ECOC '92, 1992, 907.

64. Kitagawa, T., Hattori, K., Shuto, K., Yasu, M., Kobayashi, M., and Horiguchi, M.
Electron. Lett., 1992, **28**, 1818.

65. Hattori, K., Kitagawa, T., Oguma, M., Wada, M., Temmyo, J., and Horiguchi, M.
Electron. Lett., 1992, **28**, 1818.

66. Rasmussen, T., Lumholt, O., Povlsen, J. H., and Bjarklev, A.
Electron. Lett., 1993, **29**, 455.

67. Shuto, K., Hattori, K., Kitagawa, T., Ohmori, Y., and Horiguchi, M.
Electron. Lett., 1993, **29**, 139.

68. Nakazawa, M., and Kimura, Y.
Electron. Lett., 1992, **28**, 2054.

69. Polman, A., Lidgard, A., Jacobson, D. C., Becker, P. C., Kistler, R. C., Blonder, G. E., and Poate, J. M.
Appl. Phys. Lett., 1990, **57**, 2859.

70. Polman, A., Jacobson, D. C., Eaglesham, D. J., Kistler, R. C., and Poate, J. M.
J. Appl. Phys., 1991, **70**, 3778.

71. Polman, A., Jacobson, D. C., Lidgard, A., and Poate, J. M.
Nucl. Instrum. Methods, 1991, **B59/60**, 1313.

72. Shmulovich, J., Wong, A., Wong, Y. H., Becker, P. C., Bruce, A. J., and Adar, R.
Electron. Lett., 1992, **28**, 1181.

73. Ramaswamy, R. V., and Srivastava, R.
J. Lightwave Technol., 1988, **6**, 984.

74. Malone, K. J., Sanford, N. A., and Hayden, J. S.
Electron. Lett., 1993, **29**, 691.

75. Sanford, N. A., Malone, K. J., and Larson, D. R.
Opt. Lett., 1991, **16**, 1095.

76. Sanford, N. A., Malone, K. J., Larson, D. R., and Hickernell, R. K.
Opt. Lett., 1991, **16**, 1168.

77. Sanford, N. A., Aust, J. A., Malone, K. J., and Larson, D. R.
Opt. Lett., 1993, **18**, 281.

78. Mwarania, E. K., Reekie, L., Wang, J., and Wilkinson, J. S.
Electron. Lett., 1990, **26**, 1317.

79. Mwarania, E. K., Murphy, D. M., Hempstead, M., Reekie, L., and Wilkinson, J. S.
IEEE Photon. Technol. Lett., 1992, **4**, 235.

80. Feuchter, T., Mwarania, E. K., Wang, J., Reekie, L., and Wilkinson, J. S.
IEEE Photon. Technol. Lett., 1992, **4**, 542.

81. Snocks, E., van den Hoven, G. N., Polman, A., Hendriksen, B., and Diemeer, M. B. J.
Paper 3-38 , Proc. ECIO '93, 1993.

82. Aoki, H., Maruyama, O., and Asahara, Y.
IEEE Photon. Technol. Lett., 1990, **2**, 459.

83. Aoki, H., Ishikawa, E., and Asahara, Y.
Electron. Lett., 1991, **27**, 2351.

84. Aoki, H., Maruyama, O., and Asahara, Y.
Electron. Lett., 1990, **26**, 1911.

85. Winick, K. A., and Roman, J. E.
OSA 1992 Annual Meeting , postdeadline paper PD9.

86. Lallier, E., Pocholle, J. P., Papuchon, M., DeMicheli, M. P., Quing He, M. J. Li, Ostrowsky, D. B., Grezes-Besset, C., and Pelletier, E.
IEEE J. Quantum. Electron., 1991, **27**, 618.

87. Lallier, E., Pappilon, D., Pocholle, J. P., Papuchon, M., DeMicheli, M. P., and Ostrowsky, D. B.
Electron. Lett., 1993, **29**, 175.

88. Hempstead, M., Wilkinson, J. S., and Reekie, L.
IEEE Photon. Technol. Lett., 1992, **4**, 852.

89. Brinkmann, R., Sohler, W., and Suche, H.
Electron. Lett., 1991, **27**, 416.

90. Chandler, P.J., Field, S. J., Hanna, D. C., Sheperd, D. P., Townsend, P. D., Tropper, A. C., and Zhang, L.
Electron. Lett., 1989, **25**, 985.

91. Field, S. J., Hanna, D. C., Large, A. C., Sheperd, D. P., Tropper, A. C., Chandler, P.J., Townsend, P. D., and Zhang, L.
Electron. Lett., 1991, **27**, 2376.

92. Field, S. J., Hanna, D. C., Sheperd, D. P., Tropper, A. C., Chandler, P.J., Townsend, P. D., and Zhang, L.
IEEE J. Quantum. Electron., 1991, **27**, 428.

93. Zhou, F., De La Rue, R. M., Ironside, C. N., Han, T. P. J., Henderson, B., and Ferguson, A. I.
Electron. Lett., 1992, **28**, 2041.

Chapter 3 Fabrication of Planar Silica Films by Flame Hydrolysis Deposition

3.1 Introduction

It is anticipated that in future optical communication networks signal processing will be performed at data rates which surpass the capacity of conventional electronic technology. It is highly likely that such ultra-fast optical signal processing will be fulfilled by an integrated optoelectronic technology.

Integrated optic components have several advantages over bulk optic and fibre optic configurations when operating as optical beam splitters/combiners, optical switches, wavelength and optical frequency-division multi/demultiplexers and optical time division multiplexers. These include the determination of precise optical path lengths, device stability and ruggedness, mass productivity and the possibility of integration of many optical functions on a single substrate.

One approach within the integrated optic field which has been receiving increasing attention for application in such future optical fibre communication systems is that of silica waveguides on silicon substrates. Based on a combination of silica film deposition and reactive ion etching (RIE), the resultant channel waveguides have a low loss, precisely defined core structure which have a low waveguide to fibre coupling loss as the core dimensions and refractive index match that of silica-based optical fibres [1-5]. Furthermore, there is potential for optical and electronic integration on the silicon substrate. Of the several silica deposition techniques, flame hydrolysis deposition (FHD) presents the greatest flexibility.

FHD is a "high-silica technology" in which thick layers of high-silica content glass are directly deposited onto the substrates producing, after consolidation, thin films with a high degree of homogeneity in terms of thickness and refractive index. The combination of FHD and RIE has the advantage of being able to mass produce low loss, single-mode, buried channel waveguides, as well as multi-mode ridge waveguides with core dimensions of 50 μm by 50 μm [6]. Due to the potential of producing glass with the same refractive index but with different consolidation temperatures, vertical integration of different optical circuits on a single substrate is easily attainable [7]. Also, because the glass is deposited in the form of fine particles, there is the possibility of consolidation by CO_2 laser processing [8] and monolithic integration of active and passive functions by means of rare earth doping. A disadvantage of the silica waveguides is the lack of significant electro-optic and acousto-optic effects.

Due to the low cost of the raw materials and fabrication equipment, together with the progress in waveguide formation and device packaging, the FHD technology presents an opportunity for the first large scale penetration of integrated optic devices into the opto-electronics market [9].

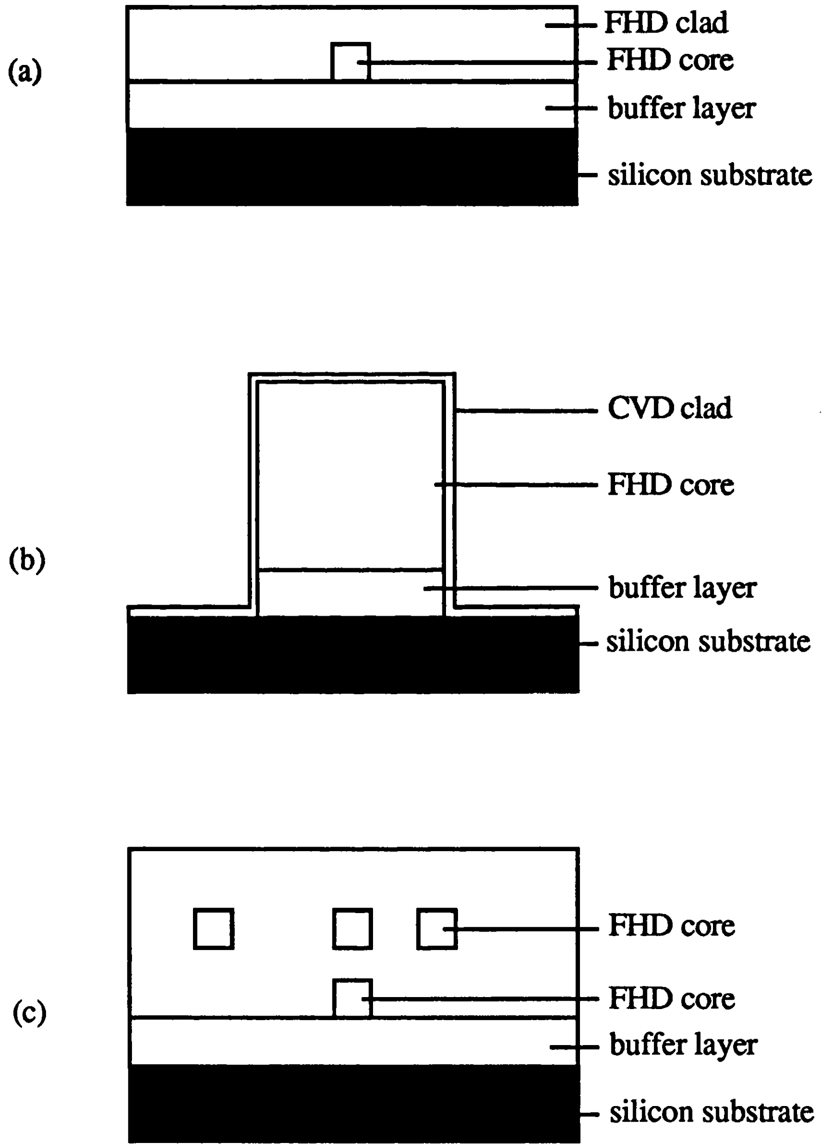

Figure 3.1 (a) single-mode buried channel waveguide and (b) multimode ridge waveguide after reference 1. Figure 3.1 (c) vertical integration of optical circuits, after reference 7.

3.2 FHD Technology and Application to Integrated Optic Components

FHD of silica was patented in 1942 by J.F.Hyde [10]. Since then the technology has been developed to produce low loss optical fibres [11,12] and more recently optical waveguides on silicon and silica substrates [13].

FHD is fundamentally a chemical vapour deposition process, where the required reagents are transported to a deposition chamber by an inert carrier gas. This technique has the advantage of added purification of the reagents, as contaminants such as transition metal ions which would cause unwanted absorption in the glass, are much less volatile. In the deposition chamber the glass forming metal chlorides are hydrolysed in an oxy-hydrogen flame to produce a "soot" of fine glass particles.

The metal chlorides used are:
- silicon tetrachloride ($SiCl_4$), producing silicon dioxide (SiO_2) when hydrolysed, which acts as the host for the dopant material.
- phosphorous trichloride (PCl_3), producing phosphorous pentoxide (P_2O_5) when hydrolysed, which acts to reduce the fusing temperature and increase the refractive index of the glass.
- germanium tetrachloride ($GeCl_4$), producing germanium dioxide (GeO_2) when hydrolysed, which acts to increase the refractive index of the glass.
- titanium tetrachloride ($TiCl_4$), producing titanium dioxide (TiO_2) when hydrolysed, which acts to increase the refractive index.
- boron trichloride (BCl_3), producing boron oxide (B_2O_3) when hydrolysed, which acts to reduce the sintering temperature and to decrease the refractive index of the glass.

The chemical reaction when the metal chlorides are hydrolysed in the oxy-hydrogen flame has the form:

$$\mathrm{Xchloride}\ (v) + H_2O\ (v) \xrightarrow{\mathrm{HEAT}} \mathrm{Xoxide}\ (s) + HCl\ (v)$$

$$X = Si,\ Ge,\ P,\ Ti,\ B$$

The soot synthesized by the flame hydrolysis process is directly deposited onto substrates, placed on a turn-table. During the deposition the torch traverses in a radial direction,with respect to the rotating turn-table, resulting in a uniform deposition thickness. The refractive index and the thickness of the films can be controlled independently by varying the relative flow rates of the reagents and the number of traverses of the torch respectively during the deposition. The soot is sintered at temperatures up to 1350°C in an electric furnace producing films from a few micrometres to 100 micrometres thick [14].

Materials used for substrates are silicon or 'Homosil' grade fused silica. The silicon substrates have a 10 μm thick, thermally grown oxide buffer layer to prevent absorption of the evanescent field of the guided mode by the silicon. Thick layers of high-silica glass can be formed on silicon substrates without cracking because of the tight fusion between the oxide buffer layer on the silicon substrate and the deposited silica layer and due to the stress in the waveguide being compressive as the thermal expansion coefficient of silicon is larger than that of the doped silica. Silica glass substrates have the disadvantage of cracking occurring in the deposited waveguide layer, particularly when doped with high levels of GeO_2, due to the tensile residual stress in the deposited layer. This is a consequence of the waveguide layer having a greater thermal expansion coefficient compared to the silica substrate. In addition, plastic deformation or "warping" of silica substrates during the sintering process occurs at a lower temperature compared to silicon substrates. Therefore, silicon is the preferred substrate material for silica waveguide formation [1].

Channel waveguides are formed by a combination of photolithographic and RIE processes. Waveguide parameters and loss characteristics of two types of buried single SiO_2-TiO_2 buried channel waveguides are given in table 3.1.

Integrated optic components such as optical beam splitters [9,15], optical switches [16], wavelength-division multi/demultiplexers [17-19] and optical frequency division multi/demultiplexers [20,21] have all been successfully fabricated based on optical circuit elements listed in ~~table~~ figure 3.2. Hybrid optical integration has also been realised using a guiding groove technique [22], mounting interference filters, laser diodes and photodetectors on the silicon substrate [23,24].

	LOW Δ	HIGH Δ
Relative index difference Δn (%)	0.25	0.75
Core size (μm)	8 x 8	6 x 6
Loss (dB/cm)	< 0.1	0.3
Fibre coupling loss (dB/point)	< 0.05	0.5

Table 3.1 Characteristics of SiO_2-TiO_2 single mode buried waveguides, from reference 1.

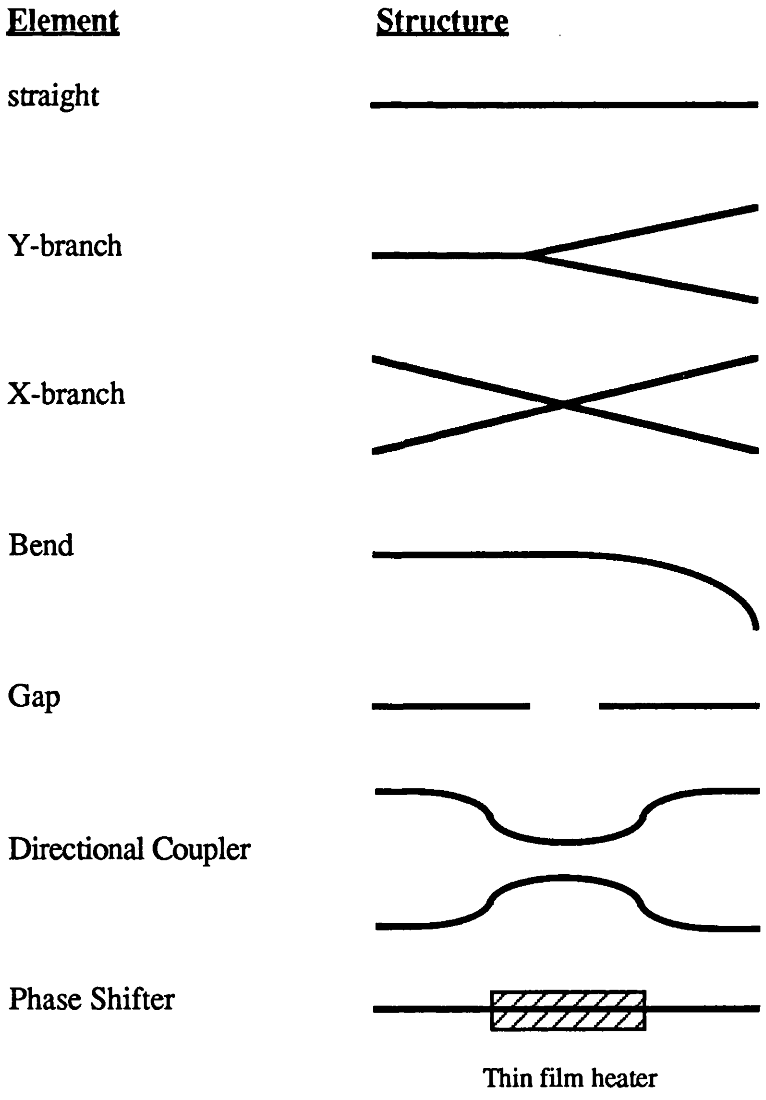

Figure 3.2 Optical circuit elements, taken from reference 1.

3.3 Flame Synthesis and Deposition of Glass Soot

Fabrication of planar optical waveguides by FHD is similar to the OVD and VAD processes used in the production of optical fibre preforms, in which metal chlorides are fed to a burner consisting of concentric circular channels. Glass particles are synthesized by means of flame hydrolysis in a pre-established oxy-hydrogen flame and deposited on a substrate placed directly beneath the flame.

Flame hydrolysis is a desirable technique for the conversion of metal chlorides into the corresponding oxides due to the purity of flame processing and the rapid reaction rates attainable, resulting from: the hydrolysis mechanism presenting a lower activation energy than oxidation, flame radicals enhancing the oxidation process and finally the higher reaction temperatures available [25].

The primary steps leading to particulate deposition in order of occurrence, as the reactants emerge from the burner have been identified as:

1. precursor reaction
2. particulate formation and growth
3. particulate deposition.

Following diffusion into the centre of the combustion zone the reagents react rapidly relative to the particulate growth rate and residence times. The formation of primary protoparticles involves a phase change from the gaseous to a condensed phase which is stable if the particle nuclei exceeds a critical radius, given by [26]:

$$r_c = \frac{2\sigma}{\rho \Delta F} \tag{3.1}$$

where σ is the surface tension, ρ is the density and F is the free energy of condensation. Ulrich [26] suggested that silica particle nucleation is particularly stable. Furthermore, he concluded that since chemical formation and nucleation of silica is instantaneous relative to particle growth rates, they have no major influence on the final particle size and that the primary factor in particle growth is Brownian motion. As the particles cool and freeze they continue to collide, they do not coalesce but stick, forming aggregates. Further collisions between aggregates form larger clusters, termed agglomerates, which are held together by physical bonds rather than fusion bonds. The collision frequency is determined by concentration of reactants and the flame temperature.

Particulate deposition by FHD is dominated by thermophoresis [27], where the soot is driven towards the relatively cool substrate by a temperature gradient [28]. The smaller thermal gradients of 100°C/cm to 400°C/cm for VAD systems, as compared to approximately 1000°C/cm for the MCVD process, combined with a large deposition surface area and a more orthogonal impact of the particle stream, results in a greater deposition efficiency and rate for the VAD system in comparison to the MCVD process.

The dependence of the deposition properties of the binary systems SiO_2-GeO_2, SiO_2-B_2O_3 and SiO_2-TiO_2 produced by FHD on substrate temperatures ranging from 200°C to 800°C have also previously been investigated [29,30]. The GeO_2 and B_2O_3 dopants were found to be deposited with a crystalline structure for a substrate temperature less than 400°C, but with an amorphous form dissolved in the SiO_2 glass network for temperatures greater than 400°C, the dissolved GeO_2 and B_2O_3 concentrations increasing with substrate temperature. In contrast, the TiO_2 dopant had no crystalline form, irrespective of the substrate temperature and the dissolved TiO_2 concentration exhibited no significant dependence on substrate temperature. Such behaviour was attributed to the saturated vapour pressure of each oxide component at the high temperatures present in the flame. Each halide reagent was found to have a threshold flow rate below which the oxide product did not form solid particles in the flame, but remained in the vapour state [31]. The threshold flow rate of the halides was in the order $SiCl_4$,$TiCl_4$ < $GeCl_4$,BBr_3 < PCl_3. Oxides with larger vapour pressure at high temperatures will tend to remain in the vapour state and hence have a greater threshold flowrate for the formation of solid particles in the flame. Consequently, oxides with a high saturated vapour pressure, such as GeO_2, will be carried to and condense on the substrate. For a substrate temperature below 400°C, the vapour phase GeO_2 will solidify in the crystalline form, but for substrate temperatures greater than 400°C there is insufficient cooling for the GeO_2 to deposit in the crystalline state.

In contrast, Potkay et al [32], analysed SiO_2-GeO_2 soot from VAD preforms and found the presence of GeO_2 crystallites for substrate temperatures ranging from 300°C to 800°C and found no indication of amorphous GeO_2 dissolved in SiO_2 for substrate temperatures greater than 500°C. On the basis of their observations, they suggested that GeO_2 exists both as hexagonal crystallites and as a shell covering silica core particles for all substrate temperatures. The presence of such crystallites does not prevent refractive index profile control, which is routinely demonstrated, but may potentially result in preform degradation if exposed to moisture.

3.4 Glass Composition

Numerous glass compositions have been formed by FHD, with TiO_2 [13,33] or GeO_2 [34,35] dopants being used to increase the refractive index of the silica glass host, with small amounts of P_2O_5 and B_2O_3 added to lower the consolidation temperature.

Our research has centred on the binary glass SiO_2-P_2O_5, because as previously discussed, the P_2O_5 dopant increases the solubility of the rare earth ions in the silica glass host. In addition, the P_2O_5 dopant leads to an increase in the refractive index and a decrease in the consolidation temperature of the glass [36-38]. Although P_2O_5 appears not to be an obvious dopant since it sublimes at 300°C, is hydroscopic and has an expansion coefficient 25 times larger than silica, SiO_2-P_2O_5 forms a stable glass with an expansion coefficient compatible with that of pure silica for P_2O_5 concentrations up to approximately 25 mole%. The glass exhibits no tendency to phase separation or to devitrification, it is chemically resistant to water and has a very low loss at wavelengths of interest for telecommunications [39].

The phase diagram for the SiO_2-P_2O_5 system, shown in figure 3.3, illustrates that even small amounts of P_2O_5 dramatically lower the temperature at which a single liquid phase solution is produced. The lowest temperature at which a single liquid phase is produced, termed the eutectic point, is 850°C for approximately 20 mole% P_2O_5 [38]. It is then evident that for P_2O_5 concentrations greater than approximately 10 mole%, for a consolidation temperature of 1300°C, a single phase will be produced by rapidly cooling the melt.

The refractive index of the SiO_2-P_2O_5 glass as a function of P_2O_5 dopant concentration is shown in figure 3.4. The refractive index increases as a linear relationship at lower P_2O_5 doping concentrations, deviating from the relationship at higher concentrations probably due to the deposited glass composition not reflecting the $SiCl_4$ and PCl_3 reacting gas mixture in the fabrication process [39].

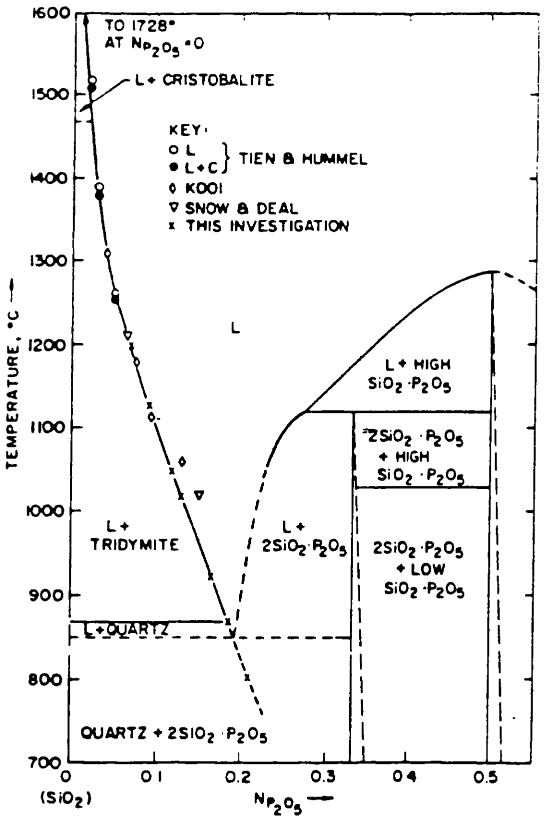

Figure 3.3 Phase diagram of SiO2-P2O5 glass, taken from reference 38.

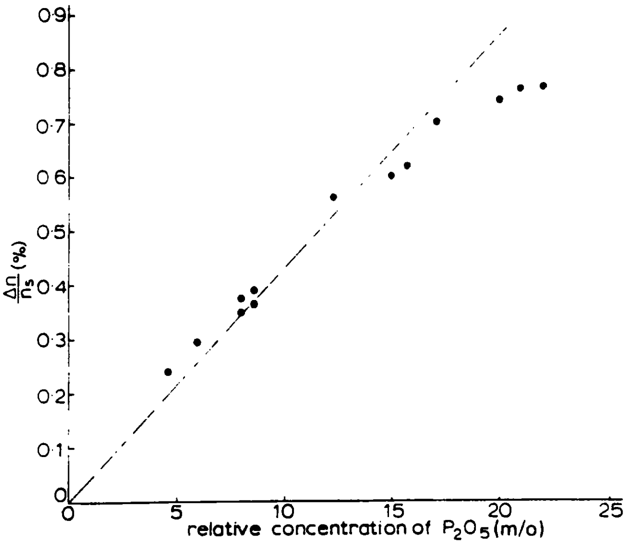

Figure 3.4 Variation of refractive index of SiO2-P2O5 glass as a function of P2O5 doping levels, taken from reference 39.

3.5 Sintering of Soot to Form Glass Film

Sintering occurs when powders of metals, ionic crystals and glasses are heated to temperatures near their melting points [40]. The initial stages of densification of a low density glass, as synthesized by FHD, proceed via the formation and growth of necks between adjoining particles where the radius of curvature is smallest. Further densification produces smooth networks or bridges which grow more slowly to form a pore-free glass layer. Figures 3.6 to 3.9 show different stages of sintering for SiO_2-P_2O_5 glass.

The theory of viscous sintering is based on an assumption proposed by Frenknel [41], that the energy required for the viscous flow is provided by a decrease in the surface energy due to a decrease in the surface area during densification. Using this assumption, he obtained expressions for the rate of growth of a neck between glass spheres and the rate of linear shrinkage of a compact glass sphere. Experimental studies have since verified Frenknel's analysis [42-45].

Scherer proposed a cubic array as a model for the microstructure of a low density, open pore glass, as shown in figure 3.5.[46] The sintering rate of the low density glass was modelled as the rate at which a cubic array of cylinders consolidates by viscous flow, driven by the surface energy reduction. As the length of the cylinder decreases, the surface area of the cell decreases, providing the driving force for densification.

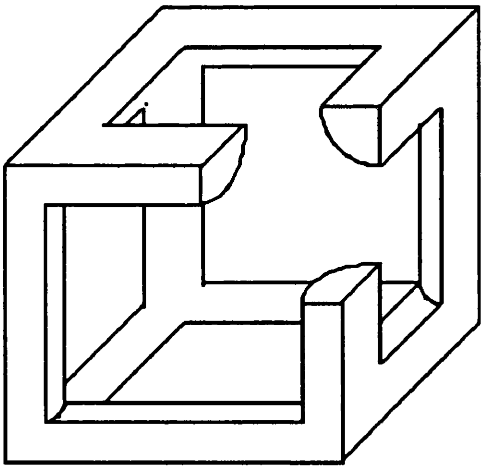

Figure 3.5 Schematic diagram of cubic array of cylinders

In Frenknel's model, the rate of energy dissipation in viscous flow, E_f, as a cylinder decreases in height is given by:

$$\frac{dE_f}{dt} = \left(\frac{3\pi\eta r^2}{h}\right)\left(\frac{dh}{dt}\right)^2 \qquad (3.2)$$

where r and h are the radius and height of the cylinder and η is the viscosity. The energy provided by the reduction in surface area is:

$$\frac{dE_s}{dt} = \gamma\frac{dS_c}{dt} \qquad (3.3)$$

where γ is the surface tension and S_c is the surface area of a cylinder.

By the conservation of energy:

$$\frac{dE_f}{dt} = -\frac{dE_s}{dt} \qquad (3.4)$$

then it can be shown that the governing dimensionless equation for isothermal viscous sintering is:

$$\frac{\rho}{\rho_s} = \left(\frac{\gamma}{\eta l_o}\right)\left(\frac{\rho_s}{\rho_o}\right)^{\frac{1}{3}}(t - t_o) \qquad (3.5)$$

where ρ = density of the cell
ρ_s = theoretical density of the solid phase
ρ_o = initial density of the cell
l_o = the initial value of the length of the cell
$t - t_o$= sintering time

The sintering rate is strongly dependent on the glass viscosity which is dependent on the temperature, glass composition and the sintering atmosphere. As already discussed the addition of P_2O_5 and B_2O_3 lowers the consolidation temperature of silica glass. The presence of water vapour in heavily hydrated samples such as those prepared by FHD, also has a strong effect on increasing the densification rate, the water reducing the viscosity of silica. The sintering atmosphere affects the sintering rate by affecting the surface tension and viscosity of glass and the pore closure [47].

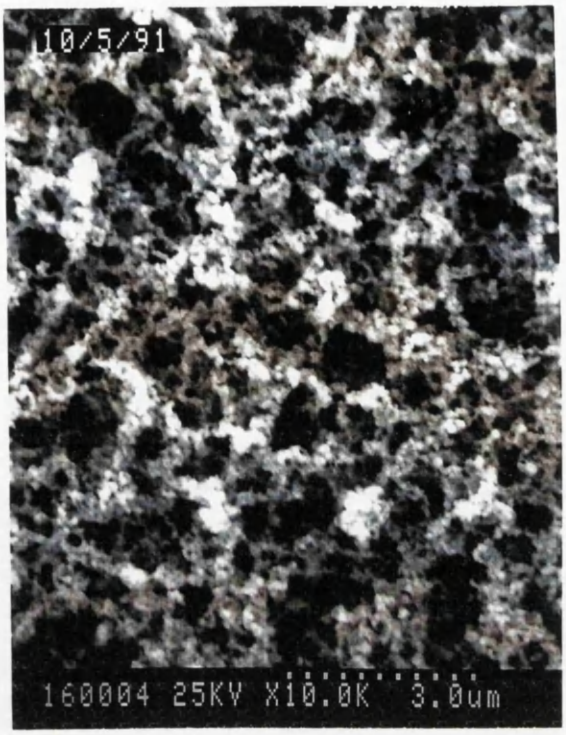

Figure 3.6 Scanning electron microscope (SEM) photograph of glass soot deposited by FHD.

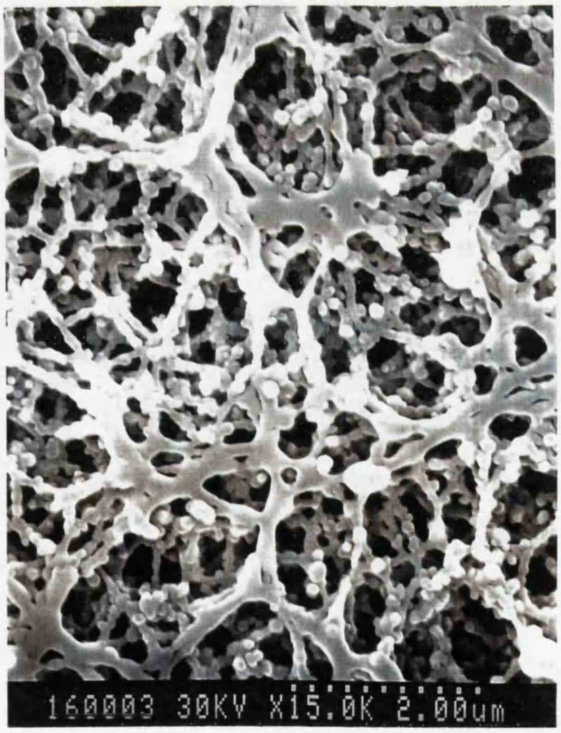

Figure 3.7 SEM photograph of initial stage of sintering of glass.

Figure 3.8 SEM photograph showing increased degree of sintering.

Figure 3.9 SEM photograph of final stages of sintering before complete consolidation.

3.6 FHD Apparatus

The original FHD apparatus in Glasgow University was constructed by Maxwell [48]. This section details modifications made to the original FHD apparatus to comply with COSHH regulations and to improve the performance of the system. The following sections give a detailed description of the reconstructed FHD apparatus.

The FHD equipment can be split into six main sections.

1) An extracted chemical cabinet where the liquid chlorides were contained in Dreschel bottles.
2) The BCl_3 gas supply system and associated gas pipeline to feed the gas to the burner.
3) Two gas supply systems: the first to supply zero grade nitrogen to the bubbler cabinet to keep the water content in the cabinet below 10 ppm and to act as an inert carrier gas for the chloride vapours; and the second to supply hydrogen and oxygen to the burner.
4) An extracted deposition chamber where the chlorides were hydrolysed and deposited as a low density soot on substrates placed on a heated turn-table.
5) A scrubber system to remove the hydrochloric vapour extracted from the deposition chamber.
6) An electric furnace where the soot deposited onto substrates was sintered to form a transparent glass film.

3.6.1 The Chemical Cabinet

The chemical cabinet was a sealed glove box which was constantly purged by a zero grade nitrogen to maintain a dry atmosphere in order to prevent hydrolysis of the metal chlorides. The temperature of the cabinet was maintained at 22°C. The optipur grade metal chlorides: $SiCl_4$, PCl_3 or $POCl_3$, $GeCl_4$ and $TiCl_4$, were contained in the chemical cabinet in Dreschel bottles which were placed in polytetrafluoroethane (PTFE) trays in case of spillage. The vapour pressure of the metal chlorides was controlled by setting the temperature of the liquids to 20°C, achieved by circulating a low viscosity oil in the outer jackets of the Dreschel bottles, the temperature of the oil controlled by a heater/refrigeration unit. The chloride vapour was transported to the deposition chamber by bubbling the zero grade nitrogen carrier gas through the Dreschel bottles, the amount of vapour transported controlled by adjusting the flow rate of the carrier gas through the bottles. The carrier gas flow rate was controlled by mass flow controllers (MFC's) and potentiometers, the flow rate being displayed on digital voltmeters. The flow path of the carrier gas was determined by pneumatic bellow valves (PBV's) which were closed or opened by solenoid valves and associated switchgear, directing the carrier gas to the waste line when not passing through the bubblers. The PBV's in the original FHD system had a stainless steel central assembly which was found to corrode in the presence of the chlorides, resulting in failure of the valves. The replacement PBV's had a polyvinyldifluoride (PVDF) central assembly which is chemically inert to the chlorides. PTFE check valves were also added to the pipeline for the flow of the carrier gas into the Dreschel bottles to prevent any escape of the chlorides to the waste line. The pipeline which fed the chloride vapours from their Dreschel bottles to the burner was continually purged with 500 sccm zero grade nitrogen to maintain a dry atmosphere to prevent any hydrolysis of the chlorides and subsequent blockage of the pipe. A manometer was used to monitor the pressure of the nitrogen carrier gas being fed into the burner.

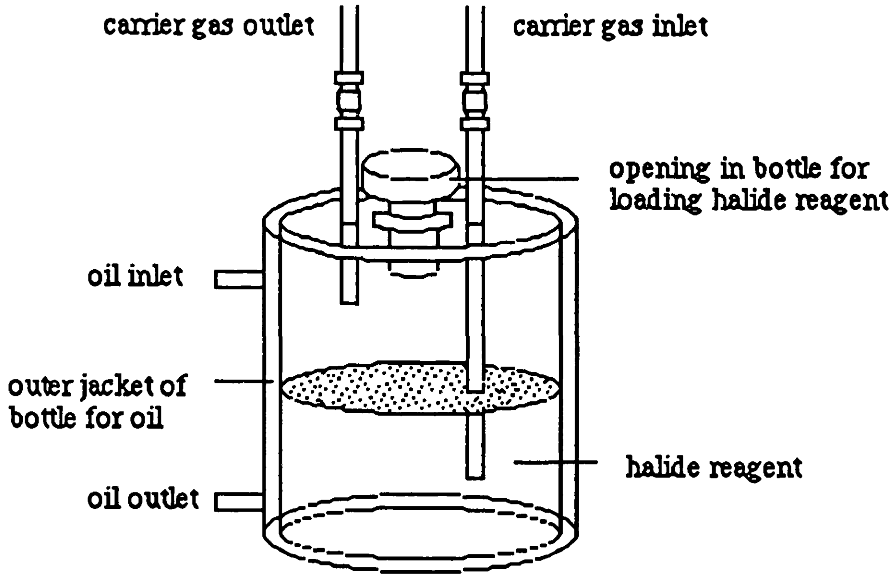

Figure 3.10 Illustration of Dreschel bottle

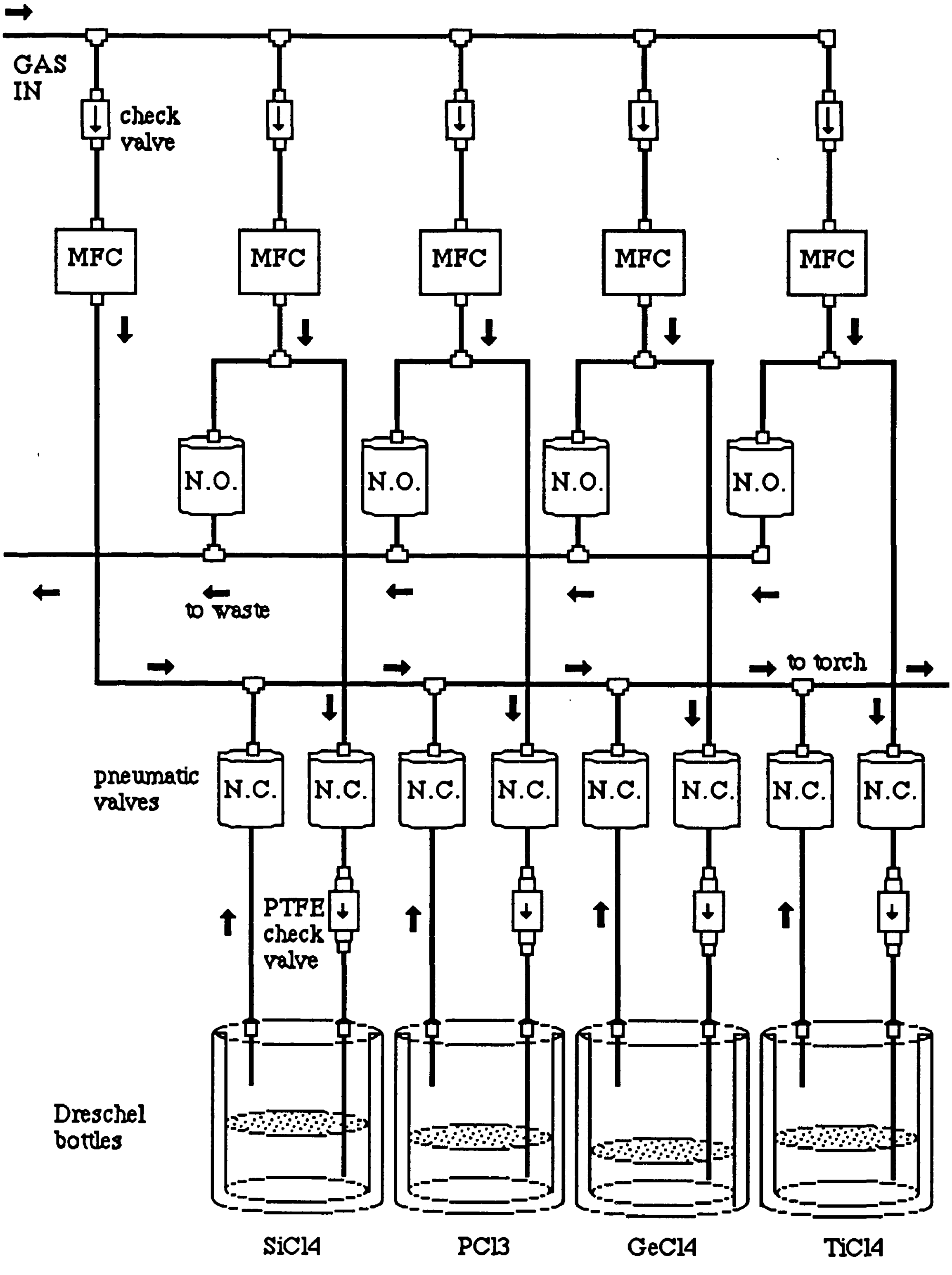

Figure 3.11 Schematic diagram of pipework of chemical cabinet
N.O. = normally open PBV   N.C. = normally closed PBV

3.6.2 The BCl3 Gas Supply

The BCl_3 gas facility consisted of a BCl_3 gas bottle contained in an extracted, sealed cabinet, the temperature of which was maintained at 26°C. The gas pipe line was continually purged by zero grade nitrogen to provide a dry atmosphere, to prevent hydrolysis of the BCl_3 in the pipe, the nitrogen gas switched off by closing a valve when BCl_3 was being fed to the burner. A temperature gradient of 3.5°C/m was maintained along the pipeline from the BCl_3 gas bottle to the MFC to assist the flow of BCl_3 gas. A separate pipeline, with nitrogen flowmeter, was provided to enable purging of the pipeline to the burner after the MFC, allowing the closure and maintenance to the section of pipework between the gas bottle and the MFC. The BCl_3 gas supply system is illustrated in figure 3.12.

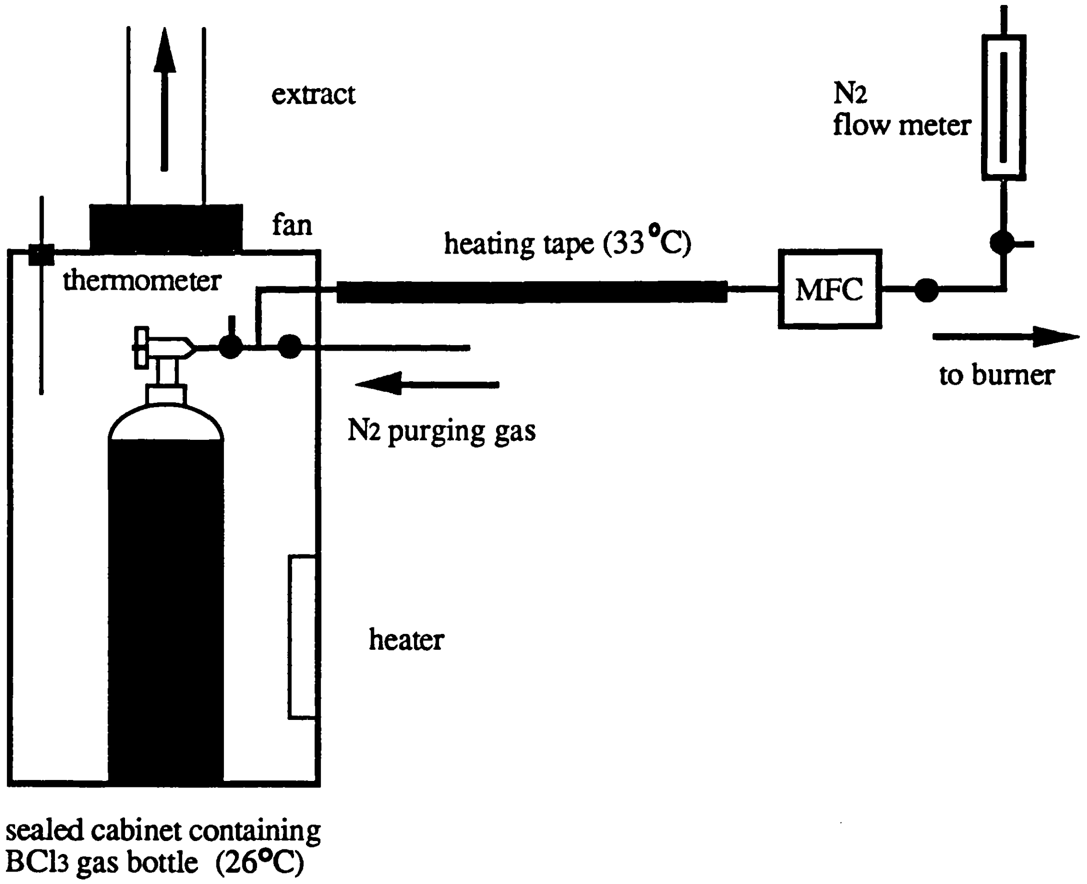

Figure 3.12 Schematic diagram of BCl_3 gas supply system being purged with nitrogen

3.6.3 The Gas Supply System

The gas supply assembly for the zero grade nitrogen consisted of four gas cylinders, regulators and valves. This gave continuous supply from two cylinders, with an electronic switch over when two cylinders empty, allowing replacement of empty cylinders without affecting the supply of gas to the bubbler cabinet. The pressure of the gas was maintained at 3.4 bar (50 psi). Gas driers were also incorporated to ensure that the water content was maintained below 10 ppm in the chemical cabinet. A 2 µm particulate filter was also present to remove any particulate contaminants.

Hydrogen and oxygen were fed to the burner to provide an oxy-hydrogen flame in order to hydrolyse the chlorides. Both gas supply lines had flowmeters incorporated to enable accurate control of the flow rates and flashback arresters for safety reasons.

3.6.4 The Deposition Chamber

The deposition chamber was where the metal chlorides were hydrolysed in an oxy-hydrogen flame, the resultant glass soot deposited onto substrates placed on a heated turn-table and the waste gases extracted to the scrubber unit. The deposition chamber is shown in figure 3.13.

The chamber was formed by hard anodised aluminium panels with a sliding perspex front screen to allow access to the chamber and visual inspection of the deposition. The hydrochloric and unreacted metal chloride vapour was extracted from the chamber by a rectangular opening at the same level as the turn-table in the chamber. An opening in the panel directly opposite from the extract had an air filter placed across it to reduce particulate contamination during the deposition, but still maintain a flow of air into the chamber to minimise flame turbulence. The torch used was a modified quartz Wickbold burner consisting of concentric tubes. The chloride vapour, hydrogen and oxygen were fed into different channels of the burner by flexible PTFE tubing. The torch was positioned with respect to the turn-table by an adjustable stand, which was mounted on a threaded screw upon which the torch traversed in a radial direction with respect to the rotating turn-table. Turn-tables used were a 180 mm diameter hard anodised aluminium turn-table capable of supporting six 30 mm diameter Homosil silica substrates, or a 360 mm diameter silicon carbide turn-table used to hold three 3 inch diameter silicon substrates. Both turn-tables were resistant to corrosion by the hydrochloric vapour. The temperature of the turn-table during a deposition was controlled by an electric heater which was placed directly underneath the turn-table. The variable transformer used to control the turn-table heater and the stepper motors which controlled the rotation of the turn-table and the linear drive for the torch were situated underneath the base aluminium panel beside the Digiplan stepper motor control units. The Digiplan stepper motor control unit was connected to an IBM PC XT computer by a General Purpose Interface Bus. The BASIC program used to control the stepper motors gave independent control over the traversal of the torch and the rotation of the turn-table.

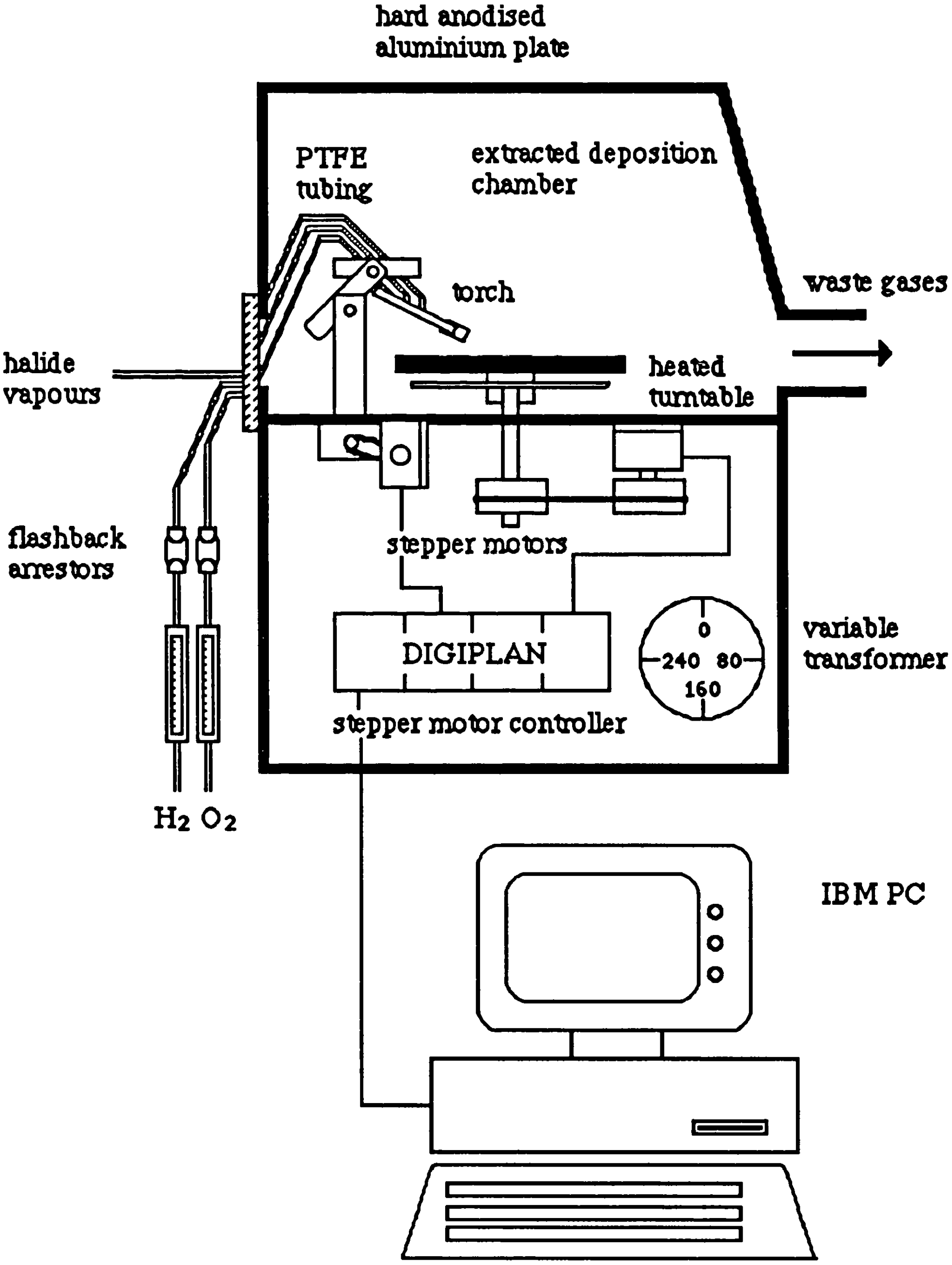

Figure 3.13 Schematic of deposition chamber and control equipment.

3.6.5 The Scrubber Unit

The waste gases extracted from the deposition chamber were neutralised in the scrubber unit, illustrated in figure 3.14. Two scrubber units were used: the first constructed from stainless steel, the replacement from plastic, required due to the gradual corrosion of the original unit. Both scrubber units were based on the same design. The extracted gas was channelled over a series of baffles, situated between which were spray bars which produced a fine mist in which the hydrochloric vapour was dissolved. Calcium carbonate was added to the water to neutralise the acid produced by the hydrochloric vapour. A pH solution was also added to monitor the basicity of the water. The scrubber unit was a closed loop system, with a pump transfering water from a reservoir to the scrubber unit.

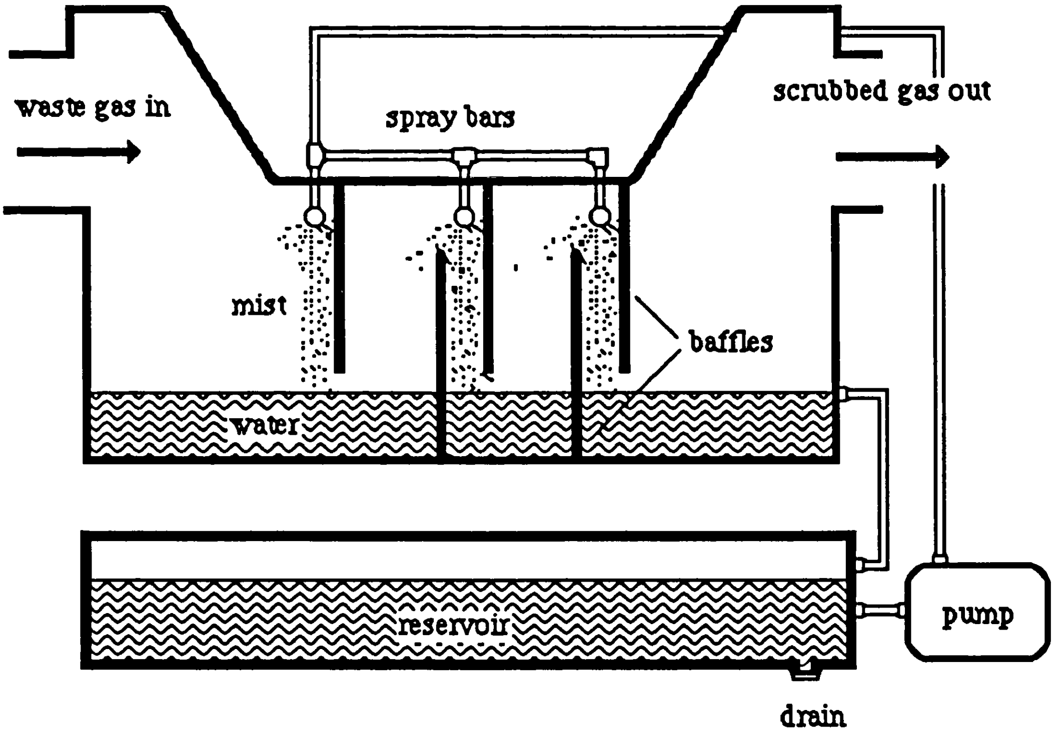

Figure 3.14 Schematic diagram of scrubber unit

3.6.6 Consolidation Furnace

The furnace used to sinter the deposited soot was a Severn Science Limited (SSL) model SC 105/4.5/1600, capable of a maximum working temperature of 1600°C. A quartz furnace tube was placed inside a SiO_2:Al_2O_3 ceramic furnace liner, giving a working tube diameter of 90 mm. The thermal profile of the furnace measured by Maxwell [48] using a Platinum/Platinum 13% Rhodium thermocouple encased in alumina sheath is given below in figure 3.15.

The table used to support the substrates horizontally during the consolidation process consisted of a 3 inch diameter, 5 mm thick piece of silica with three silica legs. The table and substrate were held in the hot zone in the centre of the furnace. This enabled three 30 mm silica substrate samples or one 3 inch diameter silicon substrate sample to be sintered at one time. The drawbacks of this type of furnace were the limited number of samples which could be consolidated at one time and the devitrification of the silica tube at the high temperatures over a period of time, causing contamination through quartz particles dropping onto the horizontally supported samples, resulting in pinholes in the film.

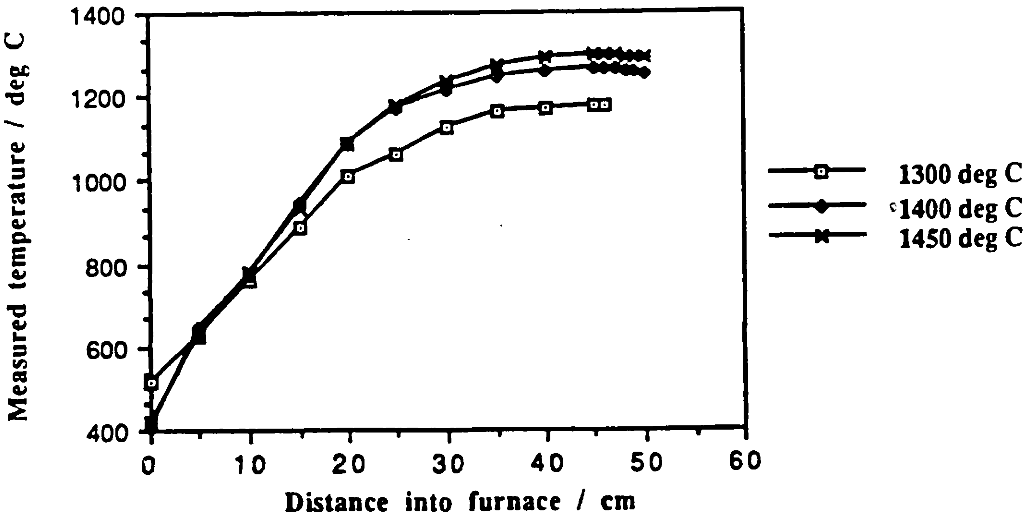

Figure 3.15 Temperature profile of furnace, taken from reference 48.

3.7 FHD Fabrication Procedure

Substrates used were either 30 mm diameter polished 'Homosil' grade silica discs or 3 inch diameter silicon wafers with a 10 μm thermally grown oxide buffer layer. Prior to the deposition of the soot, the substrates were cleaned in a class 100 cleanroom environment using the cleaning procedure outlined below:

1) 5 minute ultrasonic bath with Opticlear.
2) Rinse with acetone.
3) 5 minute ultrasonic bath with acetone.
4) Rinse with methanol.
5) 5 minute ultrasonic bath with methanol.
6) Rinse with reverse osmosis (RO) water.
7) Blown dry with nitrogen.
8) Dry for 10 minutes on hot plate.

The deposition procedure given below, first outlined by Maxwell [48], was strictly adhered to in order to ensure reproducible and safe operation of the fabrication system. The procedure is as follows:

1) Switch on turn-table heater and heat turn-table to 100°C.
2) Switch on pump for scrubber unit and computer.
3) Load fabrication program and input data required for deposition: number of traversals of torch, traversal length of torch, traversal rate of torch, and rotation rate of turn-table.
4) Set nitrogen carrier gas flow rates for required chloride reagents to desired amount using potentiometers, the flow rate displayed on digital voltmeters.
5) Place substrates on heated turn-table.
6) Open hydrogen and oxygen gas bottles.
7) Open hydrogen flow meter and ignite torch.
8) Set hydrogen and oxygen flow rates to desired amount.
9) Feed chloride reagents to burner, switch on stepper motor control, initiating deposition when hydrolysis of the reagents in the flame stabilises.
10) After completion of the deposition, switch off the transport of the chloride reagents to the torch and shut off hydrogen flow at the gas bottle on completion of hydrolysis of residual chlorides, allowing the hydrogen gas line to empty.
11) Close hydrogen and oxygen flow meters.
12) Switch off computer, stepper motor control and pump for scrubber unit.

13) Remove substrates from turn-table and place immediately in furnace for consolidation.

Typical fabrication parameters used during the deposition were:

hydrogen flow rate: 4 litres/minute
oxygen flow rate: 6 litres/minute

Halide flow rate: $SiCl_4$ 100 - 150 sccm
PCl_3 0 - 200 sccm
$GeCl_4$ 0 - 40 sccm

Deposition: Traversal length: radius of turn-table
Traversal rate: 15 cm/minute
Rotation rate: 30 revolutions/minute
Number of traversals of torch determined by required film thickness

The torch used was a modified quartz Wickbold burner. The torch had three inputs: the metal chloride vapour and nitrogen carrier gas, hydrogen and oxygen were fed through the centre, middle and outermost conduits respectively. A standard torch position during a deposition is illustrated in figure 3.16. A quartz nozzle was placed on the torch to give a more directional flame.

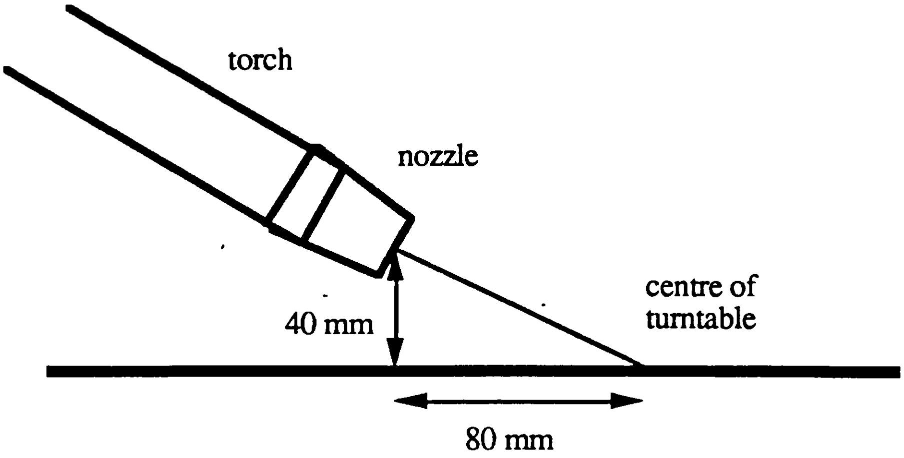

Figure 3.16 Schematic diagram of position of torch relative to turn-table during deposition.

Figure 3.17 shows the hydrolysis of 150 sccm $SiCl_4$ and 160 sccm PCl_3 using the hydrogen and oxygen flow rates given above. The bright yellow colour of the flame is characteristic of the hydrolysis of PCl_3.

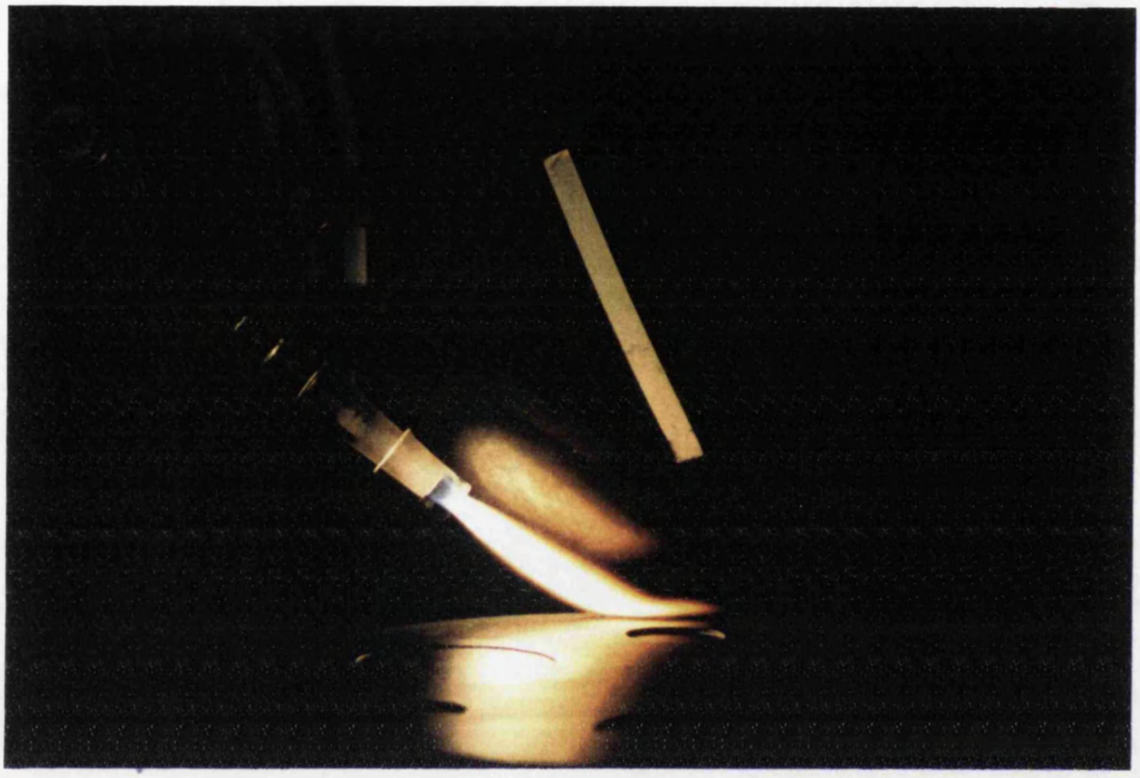

Figure 3.17 Photograph of the flame hydrolysis of $SiCl_4$ and PCl_3 using the three port torch.

For the given fabrication parameters and position of the torch with respect to the turn-table, the temperature of which was maintained at 100°C, no degradation of the deposited soot occurred as reported by Maxwell and bubbles were not present in the consolidated films. However, if the temperature of the turn-table was below 60°C, poor quality soot deposition occurred, rendering the film unsuitable for consolidation. To sinter the glass soot, the samples were heated up to 1350°C in the furnace, maintained at the temperature for two hours and removed rapidly, without ramping down the temperature.

Two further sources of contamination of the glass soot were dust particles from the laboratory environment and from the quartz burner. Due to the flame coming into contact with the burner and nozzle, devitrification occurred, resulting in quartz particles being deposited with the soot, again resulting in pinholes in the final consolidated film. Figure 3.18 shows a photograph of a typical defect produced by such contamination.

To minimise such problems, it was necessary to clean the burner and nozzle in buffered hydrofluoric acid after use.

Figure 3.18 Photograph of defect in consolidated glass film produced by contamination by quartz particles.

3.8 Conclusion

The FHD technology, based on a combination of silica film deposition and RIE, has the advantage of mass producing, at low cost, with a high degree of reproducibility, integrated optic devices for application in future optical communication networks.

Furthermore, the FHD technology is flexible in terms of the glass compositions it facilitates, enabling fabrication of glasses with a wide range of refractive indices and consolidation temperatures. Our research has centred on the binary glass SiO_2-P_2O_5, where the P_2O_5 acts to increase the refractive index, decrease the sintering temperature and increase the solubility of rare earth dopants in the glass matrix.

3.9 References

1. Kawachi, M.
Opt. and Quant. Electron., 1990, **22**, 391.

2. Izawa, T., Mori, H., Murakami, Y., and Shimizu, N.
Appl. Phys. Lett., 1981, **38**, 483.

3. Valette, S., Renard, S., Denis, H., Jadot, J. P., Founier, A., Philippe, P., Gidon, P., Grouillet, A. M., and Desgranges, E.
Solid State Techn., 1989, **32**, 69.

4. Henry, C. H., Blonder, G. E., and Kazarinov, R. F.
J. Lightwave Techn., 1989, **7**, 1530.

5. Imoto, K., Takahiro, A., and Sano, H.
Proc. ECOC '88, Brighton, September 1988.

6. Himeno, A., Kobayashi, M., and Terui, H.
Electron. Lett., 1985, **21**, 1020.

7. Barbarossa, G., and Laybourn, P. J. R.
Electron. Lett., 1992, **28**, 437.

8. Yamada, Y., Kawachi, M., Yasu, M., and Kobayashi, M.
Appl. Opt., 1985, **24**, 454.

9. Photonic Integration Research, Inc. (PIRI), Product Catalogue.
Sept., 1992.

10. Hyde, J. F.
United States Patent, no. 2, 272, 342, Feb. 1942.

11. Izawa, T., and Inagaki, N.
Proc. IEEE, 1980, **68**, 1184.

12. Keck, D. B., Schultz, P. C., and Zimar, F.
United States Patent, no. 3, 737, 292, 1973.

13. Kawachi, M., Yasu, M., and Edahiro, T.
Electron. Lett., 1983, **19**, 583.

14. Yasu, M., Kawachi, M., and Kobayashi, M.
Trans. IECE Jpn., 1985, **J68-C**, 454.

15. Takahashi, H., Ohmori, Y., and Kawachi, M.
Electron. Lett., 1991, **27**, 2131.

16. Takato, N., Jinguji, K., Yasu, M., Toba, H., and Kawachi, M.
J. Lightwave Techn., 1988, **6**, 1003.

17. Barbarossa, G., and Laybourn, P. J. R.
Electron. Lett., 1991, **27**, 2085.

18. Kawachi, M.
Proc. CLEO '89, Baltimore, April 1989.
19. Kawachi, M., Yamada, Y., Yasu, M., and Kobayashi, M.
Electron. Lett., 1985, **21**, 314.
20. Inoue, N., Takato, N., Toba, H., and Kawachi, M.
J. Lightwave Techn., 1988, **6**, 339.
21. Toba, H., Oda, K., Nosu, K., and Takato, N.
Electron. Lett., 1989, **25**, 574.
22. Yamada, Y., Kawachi, M., Yasu, M., and Kobayashi, M.
Electron. Lett., 1984, **20**, 589.
23. Kawachi, M., Kobayashi, M., and Miyashita, T.
Proc. IGWO '86, Atlanta, 1986, paper FDD5.
24. Kobayashi, M., Yamada, M., Yamada, Y., Himeno, A., and Terui, H.
Electron. Lett., 1987, **23**, 143.
25. Miller, T. J., Potkay, E., and Yuen, M. J.
Fibre Optics: Processing and Applications.
AIChE Symposium Series, **83**, 1.
26. Ulrich, G. D.
Combust. Sci. and Technol., 1971, **4**, 47.
27. Gourdin, W. H., and Andrejco, M. J.
J. Appl. Phys., 1982, **53**, 5920.
28. Walker , K. L., Geyling, F. T., and Nagel, S. R.
J. Am. Ceram. Soc., 1980, **63**, 552.
29. Kawachi, M., Sudo, S., Shibata, N., and Edahiro, T.
Jpn. J. Appl. Phys., 1980, **19**, L69.
30. Kawachi, M., Sudo, S., Shibata, N., and Edahiro, T.
Jpn. J. Appl. Phys., 1980, **19**, 2047.
31. Kawachi, M., Sudo, S., Shibata, N., and Edahiro, T.
Jpn. J. Appl. Phys., 1981, **20**, 709.
32. Potkay, E., Clark, H. R., Smyth, I. P., Kometani, T. Y., and Wood, D. L.
J. Lightwave Techn., 1988, **6**, 1338.
33. Kawachi, M., Yasu, M., and Kobayashi, M.\
Jpn. J. Appl. Phys., 1983, **22**, 1932.
34. Kashyap, R., Ainslie, B. J., and Maxwell, G. D.
Electron. Lett., 1989, **25**, 206.
35. Kominato, T., Ohmori, Y., Okazaki, H., and Yasu, M.
Electron. Lett., 1990, **26**, 327.

36. Hammond, C. R.
Phys. and Chem. Glasses, 1978, **19**, 41.

37. Tien, T. Y., and Hummel, F. A.
J. Am. Ceram. Soc., 1962, **45**, 422.

38. Eldridge, J. M., and Balk, P.
Trans. Metall. Soc. AIME, 1968, **242**, 539.

39. Gambling, W. A., Payne, D. N., Hammond, C. R., and Norman, S. R.
IEE Proc., 1976, **123**, 570.

40. Mackenzie, J. K., and Shuttleworth, R.
Proc. Phys. Soc. London, 1949, **62**, 833.

41. Frenkel, J.
J. Phys. (Moscow), 1945, **9**, 385.

42. Scherer, G. W.
J. Am. Ceram. Soc., 1977, **60**, 239.

43. Kuczynski, G. C.
J. Appl. Phys., 1949, **20**, 1160.

44. Kingery, W.D, and Berg, M.
J. Appl. Phys. 1955, **26**, 1205.

45. Yan, M. F., MacChesney, J. B., Nagel, S. R., and Rhodes, W. W.
J. Mater. Sci., 1980, **15**, 1371.

46. Scherer, G. W.
J. Am. Ceram. Soc., 1977, **60**, 236.

47. Walker, K. L., Harvey, J. W., Geyling, F. T., and Nagel, S. R.
J. Am. Ceram. Soc., 1980, **63**, 96.

48. Maxwell, G. D.
PhD Thesis, University of Glasgow, 1990.

Chapter 4 Optical Planar Waveguides

4.1 Introduction

This chapter reviews the theory of slab dielectric optical waveguides and the coupling of light into a waveguide mode using a prism coupler. The attenuation mechanisms which are present in dielectric optical waveguides are also considered.

The homogeneity of SiO_2-P_2O_5 films in terms of refractive index and thickness is investigated. The fabrication of rare earth doped planar films incorporating the rare earth ions using the solution doping and the aerosol doping techniques is also described. Finally, a comprehensive investigation of the loss of passive and rare earth doped films using the three prism and the fibre probe techniques is presented.

4.2 Dielectric Slab Waveguide

A dielectric slab waveguide consists of a thin dielectric film of refractive index n_f, thickness W, formed on a transparent, rigid, dielectric substrate of refractive index n_s. The superstrate or cladding layer, refractive index n_c, is generally air or another dielectric layer. The propagation of light in the dielectric film, or waveguide, only occurs when the film refractive index n_f is greater than n_s and n_c. When n_s and n_c are equal, the waveguide is symmetric, but if n_s and n_c are different, then the waveguide is termed asymmetric.

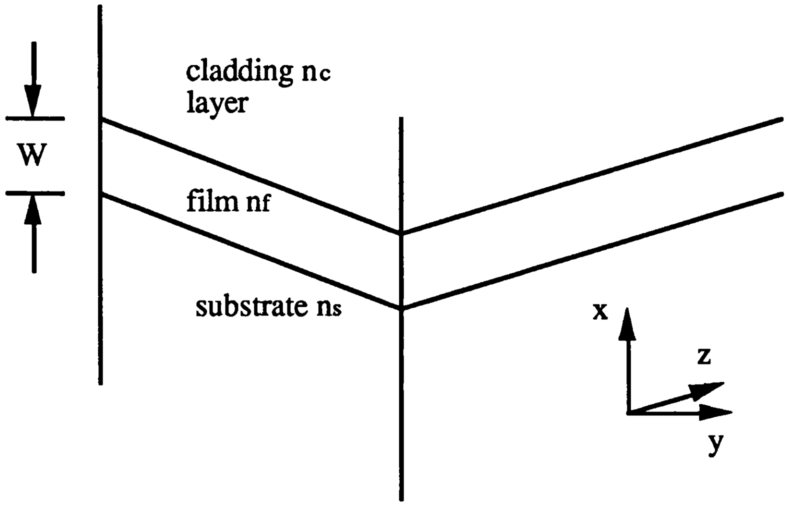

Figure 4.1 Schematic of a dielectric slab waveguide

There are two different refractive index profiles for waveguides: a step-index waveguide, in which the refractive index changes abruptly along the depth; and a graded-index waveguide, in which the refractive index gradually changes along the depth. A detailed analysis of the step-index waveguide will be presented as this was the type of waveguide fabricated by FHD.

There are two different techniques to describe light propagation in planar waveguides. The first uses a ray-optical picture, which utilises the phase shift experienced by plane waves propagating in the film to describe the guided mode [1-3]. The second- adopted by the author - applies Maxwell's equations [4-7].

4.3 Wave Equations

Maxwell's equations for an isotropic, lossless, dielectric medium are:

$$\underline{\nabla} \times \underline{E} = -\mu_o \frac{\partial \underline{H}}{\partial t} \qquad (4.1)$$

$$\underline{\nabla} \times \underline{H} = n^2 \varepsilon_o \frac{\partial \underline{E}}{\partial t} \qquad (4.2)$$

where $\underline{E}$ and $\underline{H}$ are the electric and magnetic field vectors, n is the refractive index of the medium and ε_o and μ_o are the dielectric permittivity and magnetic permeability of free space respectively. A mode of a dielectric waveguide is a solution of the wave equation:

$$\nabla^2 \underline{E}(r) + k_o^2 n^2(r)\, \underline{E}(r) = 0 \qquad (4.3)$$

where:

$$k_o^2 = \omega^2 \mu_o \varepsilon_o = \left(\frac{2\pi}{\lambda}\right)^2 \qquad (4.4)$$

where λ is the wavelength of the light in free space and ω is the angular frequency. The solutions are subject to the continuity of the tangential components of $\underline{E}$ and $\underline{H}$ at the dielectric interfaces and are of the form:

$$\underline{E}(\underline{r}, t) = \underline{E}(x, y) \exp i(\omega t - \beta z) \qquad (4.5)$$

$$\underline{H}(\underline{r}, t) = \underline{H}(x, y) \exp i(\omega t - \beta z) \qquad (4.6)$$

This corresponds to a wave travelling in the positive z-direction with a phase velocity $v = \omega/\beta$. The factor $\exp i(\omega t - \beta z)$ is common to all field expressions and may be om~~m~~itted.

Making the assumption that the slab waveguide is infinite in the y-direction so that there is no variation in the y-direction i.e. $\frac{\partial}{\partial y} = 0$ and replacing $\frac{\partial}{\partial t}$ by $i\omega$, then Maxwell's equations can be written:

$$\frac{\partial E_y}{\partial z} = i\omega\mu_0 H_x \tag{4.7a}$$

$$\frac{\partial E_x}{\partial z} - \frac{\partial E_z}{\partial x} = -i\omega\mu_0 H_y \tag{4.7b}$$

$$\frac{\partial E_y}{\partial x} = -i\omega\mu_0 H_z \tag{4.7c}$$

$$\frac{\partial H_y}{\partial z} = -i\omega\varepsilon_0 n^2 E_x \tag{4.7d}$$

$$\frac{\partial H_x}{\partial z} - \frac{\partial H_z}{\partial x} = i\omega\varepsilon_0 n^2 E_y \tag{4.7e}$$

$$\frac{\partial H_y}{\partial x} = i\omega\varepsilon_0 n^2 E_z \tag{4.7f}$$

This yields two self-consistent types of solutions. The first contains E_y, H_x, and H_z and is referred to as transverse electric (TE) modes. The second, transverse magnetic (TM) modes, has H_y, E_x, E_z as non-zero components.

Considering the case of TE polarised waves, substituting (4.7a) and (4.7c) into (4.7e) gives the wave equation for E_y:

$$\frac{\partial^2 E_y}{\partial x^2} + \left(k_o^2 n_f^2 - \beta^2\right) E_y = 0 \tag{4.8}$$

The solution of equation (4.8) must satisfy the boundary conditions that the tangential component E_y and $\frac{\partial E_y}{\partial x}$ is continuous across the film boundary at $x = -W$ and $x = 0$.

Furthermore, in order to have physical significance, E_y must tend to zero as x tends to $\pm\infty$. For guided modes, a solution which satisfies these requirements is:

$$E_y = E_f \cos\phi_c \exp(-\gamma_c x) \quad x > 0 \text{ cladding} \tag{4.9a}$$

$$E_y = E_f \cos(kx + \phi_c) \quad -W < x < 0 \text{ film} \tag{4.9b}$$

$$E_y = E_f \cos(-kW + \phi_c)\exp[\gamma_s(x + W)] \quad x < -W \text{ substrate} \tag{4.9c}$$

where

$$\beta = k_o n_f \sin\theta = k_o N \tag{4.10}$$

$$k = k_o n_f \cos\theta \tag{4.11}$$

$$\beta^2 + k^2 = k_o^2 n_f^2 \tag{4.12}$$

$$\gamma_c^2 = \beta^2 - k_o^2 n_c^2 \tag{4.13}$$

$$\gamma_s^2 = \beta^2 - k_o^2 n_s^2 \tag{4.14}$$

The angle θ in the ray-optical picture, is the angle which the wave vector makes with the normal to the interfaces and $N = n_f \sin\theta$ is defined as the effective index.

Application of the boundary conditions yields the formulae for the phase shift experienced on internal reflection between the film-substrate and film-clad interfaces, $\phi_s = \tan^{-1}\frac{\gamma_s}{k}$ (4.15) and $\phi_c = \tan^{-1}\frac{\gamma_c}{k}$ (4.16) respectively and an eigenvalue equation:

$$kW = m\pi + \tan^{-1}\frac{\gamma_c}{k} + \tan^{-1}\frac{\gamma_s}{k} \tag{4.17}$$

where m = 0, 1, 2 ... denotes the mode number. This indicates that the waveguide can support a discrete number of modes, m, provided that the propagation constant β and the waveguide thickness W satisfy the eigenvalue equation. For a step-index two-dimensional waveguide, the transverse resonance condition, equation (4.17), can be rewritten in the form:

$$V\sqrt{1-b} = m\pi + \tan^{-1}\left(\frac{b}{1-b}\right)^{\frac{1}{2}} + \tan^{-1}\left(\frac{a+b}{1-b}\right)^{\frac{1}{2}} \qquad (4.18)$$

where the normalised frequency is written:

$$V = k_o W \sqrt{n_f^2 - n_s^2} \qquad (4.19)$$

and the normalised guide index and asymmetry measure of the waveguide are defined by:

$$b = \frac{\left(N^2 - n_s^2\right)}{\left(n_f^2 - n_s^2\right)} \quad (4.20) \text{ and } \quad a = \frac{\left(n_s^2 - n_c^2\right)}{\left(n_f^2 - n_s^2\right)} \quad (4.21).$$

When waveguide parameters, such as the guide thickness W and the refractive indices are given, the effective index of the guided mode can be obtained graphically as shown below.

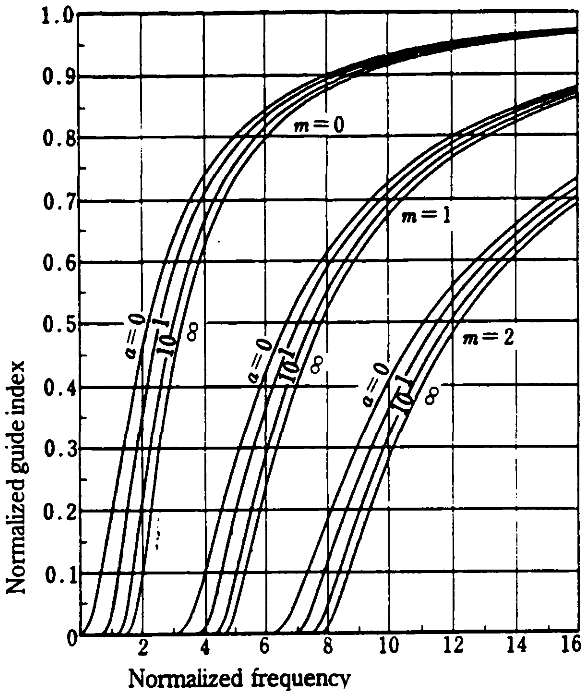

Figure 4.2 Dispersion curves of step-index planar waveguide, taken from reference 5.

When the angle θ becomes the critical angle defined by Snell's Law for the waveguide-substrate interface, the light is no longer confined in the film and begins to leak into the substrate at the interface. The guided mode is then said to be cut-off and the effective index $N = n_s$ ($b = 0$). From equation (4.18), the value of V_m at cutoff is given by:

$$V_m = V_o + m\pi\,, \quad V_o = \tan^{-1}\sqrt{a} \tag{4.22}$$

where V_o is the cutoff value for the fundamental mode. After the loss of total internal reflection, γ_s becomes imaginary and a continuum of radiation modes occurs. For symmetrical waveguides, $V_o = 0$, implies that the fundamental mode is not cutoff .

Following a similar procedure, Maxwell's equations can be solved for TM modes, where H_y, E_x, and E_z are the non-zero components. Applying the condition that E_z and H_y are continuous at the interfaces $x = 0$ and $x = -W$, yields the eigenvalue equation:

$$kW = m\pi + \tan^{-1}\left(\frac{n_f}{n_s}\right)^2\left(\frac{\gamma_s}{k}\right) + \tan^{-1}\left(\frac{n_f}{n_c}\right)^2\left(\frac{\gamma_c}{k}\right) \tag{4.23}$$

with $m = 0,1, 2, ..$

Similar to TE modes, there exists a discrete number of guided modes, plus a continuum of radiation modes present when there is no longer total internal reflection at at least one interface.

4.4 Effective Waveguide Thickness

The power P carried by a TE mode per unit waveguide length is given by:

$$P = \frac{1}{2}\,\mathrm{Re}\int_{-\infty}^{\infty}(\underline{E} \times \underline{H}^*).\,\underline{\hat{z}}\,dx = -\frac{1}{2}\int_{-\infty}^{\infty}E_y H_x^* dx \tag{4.24}$$

which can be rewritten in the form:

$$P = \frac{1}{4}E_f.\,H_f.\,W_{eff} \tag{4.25}$$

where:

$$W_{eff} = W + \frac{1}{\gamma_s} + \frac{1}{\gamma_c} \qquad (4.26)$$

Equation (4.25) indicates that the guided mode is confined to the thickness W_{eff}. The electric field penetrates from the waveguide to depths $1/\gamma_s$ and $1/\gamma_c$ in the substrate and the clad respectively and therefore W_{eff} is the effective waveguide thickness.

4.5 Prism-Film Coupler

There are numerous methods to couple light into a waveguide. They include end-fire coupling, the grating coupler [8], the taper coupler [9] and the prism coupler [7,10,11]. For reasons of convenience, the prism coupling method was exclusively used to investigate the optical properties of the planar films.

Prism coupling involves a prism which has a refractive index n_p, where n_p is greater than n_f, pressed against a waveguide as illustrated in figure 4.3.

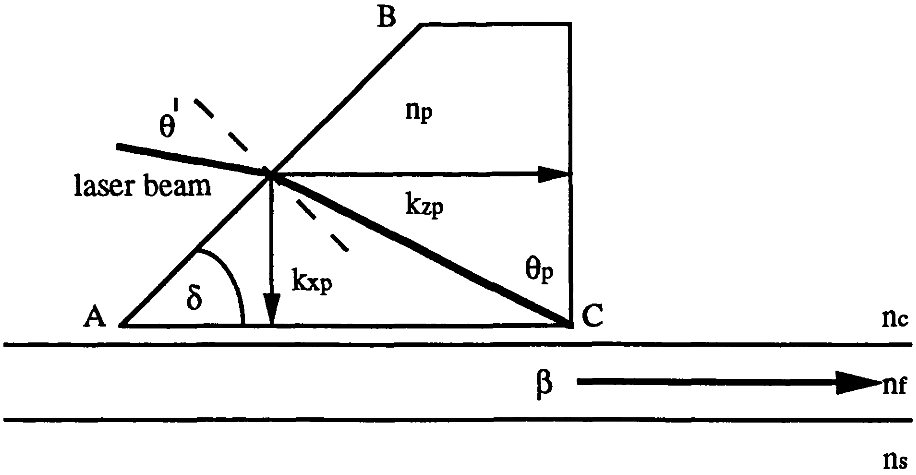

Figure 4.3 Schematic of prism coupling.

If an incident laser beam makes an angle θ_p with respect to the normal of the prism base and θ_p is greater than the critical angle $\sin^{-1}(n_{air}/n_p)$, due to the presence of an air gap between the film and the prism base, the beam experiences total internal reflection, resulting in an evanescent field below the base of the prism. If the gap is sufficiently small, light can be coupled into the waveguide by a process termed 'optical tunnelling', whereby the evanescent field below the base of the prism extends into the waveguide and excites a waveguide mode. For a particular mode to be excited, it is necessary to match the propagation constant of the mode in the waveguide and the z-component of the wavevector in the prism. If the magnitude of the wavevector in the prism is k_on_p, the z-component and x-component are $k_on_p\sin\theta_p$ and $k_on_p\cos\theta_p$ respectively. Therefore, as the angle at which the laser beam is incident on the prism base is varied, the components of the wavevector in the prism will change. At a particular value of θ_p, where the propagation constant of one of the waveguide modes is equal to $k_on_p\sin\theta_p$, phase matching occurs and a waveguide mode is excited. The angle θ' outside the prism can be correlated to θ_p using Snell's Law and it can be shown that:

$$N_{eff} = n_p \sin\left\{\delta + \sin^{-1}\left(\frac{\sin\theta'}{n_p}\right)\right\} \tag{4.27}$$

where N_{eff} is the effective index of the excited mode, δ is the prism angle BAC and θ' is the angle of incidence on the prism face AB. The point where the beam strikes the the prism base is the coupling spot and it is at this point where the effective index is measured. The input coupling efficiency for prism coupling can be calculated by using the reciprocity theorem as:

$$\eta = \frac{\left[\int g(z)h(z)dz\right]^2}{\int g^2(z)dz \int h^2(z)dz} \tag{4.28}$$

where h(z) is the amplitude distribution of the incident beam on the prism bottom and g(z) is the amplitude distribution of the waveguide mode. When the prism is used to couple a gaussian beam into a waveguide mode, the calculated optimum coupling efficiency is 80.1 %.

As well as coupling light into a waveguide, the prism coupler may also be used to couple light out of a waveguide. When light is coupled out of the waveguide, different modes have different output angles associated with them. When viewed on a screen, a series of lines which extend along the direction normal to the plane of the beam exit are observed. These are termed m-lines and the spectrum of m-lines viewed is due to light scattering within multimode waveguides. The m-line is a consequence of the in-plane scatter and may be used as a qualitative measure of the quality of the waveguide. The longer the m-line, the greater the in-plane scatter. When the incident laser beam is in the synchronous direction, where phase matching occurs for a particular mode, a bright spot appears in the centre of the m-line and there is an increase in the intensity of the m-line which corresponds to the excited mode. When the laser beam is not in the synchronous direction, no modes are excited, although scattered light from the prism base may weakly excite the m-lines.

4.6 Evaluation of Waveguide Parameters

Waveguide parameters can be calculated from the measured values of the effective indices of the different waveguide modes. Using the prism-coupler, the coupling should be weak for accurate measurements, as strong coupling causes errors in the measured propagation constant in the coupling region due to perturbation by the prism.

From one measured value of the effective index and either the film refractive index or thickness ~~is~~ known from other measurements, the unknown waveguide parameter may be evaluated from equation (4.18) using an iterative process.

From two measured values of effective index, N_m and N_n, equations:

$$k\sqrt{n_f^2 - N_m^2}\,W = \Phi_m(n_f^2, N_m^2),\; k\sqrt{n_f^2 - N_n^2}\,W = \Phi_n(n_f^2, N_n^2) \qquad (4.29a,b)$$

can be derived from equation (4.18). The unknown parameters n_f and W can be found graphically or by iterative calculations. Eliminating W from equation (4.29), n_f may be evaluated using an iterative process. Once n_f has been determined, W can be calculated directly. If the calculation is carried out with high accuracy, the uncertainty of the value calculated for n_f is comparable to that of N. However, the uncertainty in W is greater, especially when the value measured for N is close to n_f.

Finally, if there are three or more measured values of N, the reliability of the measurement and the accuracy of the calculated parameters can be checked by comparing the values calculated for different modes from the mode spectrum.

4.7 Film Characterisation

The homogeneity of planar film thickness and refractive index was investigated for multimode SiO_2-P_2O_5 films deposited on 3 inch diameter silicon substrates, which had a 10 µm thermally grown oxide layer. The refractive index of the buffer layer was 1.457 at 632.8 nm.

The SiO_2-P_2O_5 films were fabricated using a 3 port torch: the metal chloride vapour and nitrogen carrier gas, hydrogen and oxygen fed through the centre, second and outermost conduits respectively. The hydrogen and oxygen flow rates were 4 litres/minute and 6 litres/minute. The flow rate of the nitrogen carrier gas for the $SiCl_4$ was kept constant at 150 sccm. Torch traversal rate was 15 cm/minute and turntable rotation rate was 30 revolutions/minute. Film thickness and refractive index were determined independently by varying the number of traversals of the torch and the flow rate of the nitrogen gas used to transport the PCl_3 vapour, respectively. Consolidation was accomplished by sintering the films at 1300°C for 2 hours in an air atmosphere.

The thickness of the films was measured by three techniques. The first method involved a section of the glass soot being removed from the substrate using a razor blade after the deposition. After consolidation, Talystep measurements were made across the interface produced by the removal of the soot. It was essential to ensure complete removal of the soot, as any remnants would consolidate and result in a thinner film thickness being measured than was actually deposited.

The second technique was based on the fact that SiO_2-P_2O_5 glass has a greater etch rate, by a ratio of 20-30 to 1, as compared to pure SiO_2, when immersed in a solution of 15 parts HF (49%): 10 parts $H(NO_3)$: 300 parts H_2O [12]. This method entailed the sample being completely covered in wax and windows in the wax mask being opened above the areas where the film thickness was to be measured. The sample was then immersed in the 'p-etch' for 20 hours. The film thickness was able to be measured by Talystep in the selected areas, due to the difference in etch gradients between the SiO_2-P_2O_5 and SiO_2 glass, enabling discrimination between the film and substrate, as indicated in figure 4.4.

The final method used to measure the thickness of films, as well as the refractive index, was the prism coupling technique. The prisms were fixed on a rotating stage which was placed on translation stages. The prisms were made from Schott SF 15 glass, refractive index 1.6942, with a prism angle of 60.00°; or from BAK 7 glass, refractive index 1.5667, with a prism angle of 75.00°. Light from a Helium-Neon 632.8 nm laser was polarised to excite TE or TM waveguide modes. After measuring the synchronous angles at weak coupling, the waveguide effective indices were calculated using equation (4.27). The thickness and refractive index of films which supported more than 2 modes were calculated by means of a computer program.

For a typical thin film, fabricated using the parameters listed above, for 8 traversals of the torch, the thickness of the waveguide layer was measured to vary from 5.5 μm to 7.2 μm. The film thickness was greater at the edge of the substrate placed nearest to the centre of the turn-table, region A in figure 4.5 and decreased towards the edge of the substrate situated closest to the edge of the turn-table, region E. As the glass soot was deposited in bands, the film thickness in each band, as anticipated, was measured to be uniform. Table 4.1 presents results for the film thickness for the five selected regions measured using the prism coupling and 'p-etch' techniques. From table 4.1, it can be seen there is agreement between the different methods used to measure the film thickness.

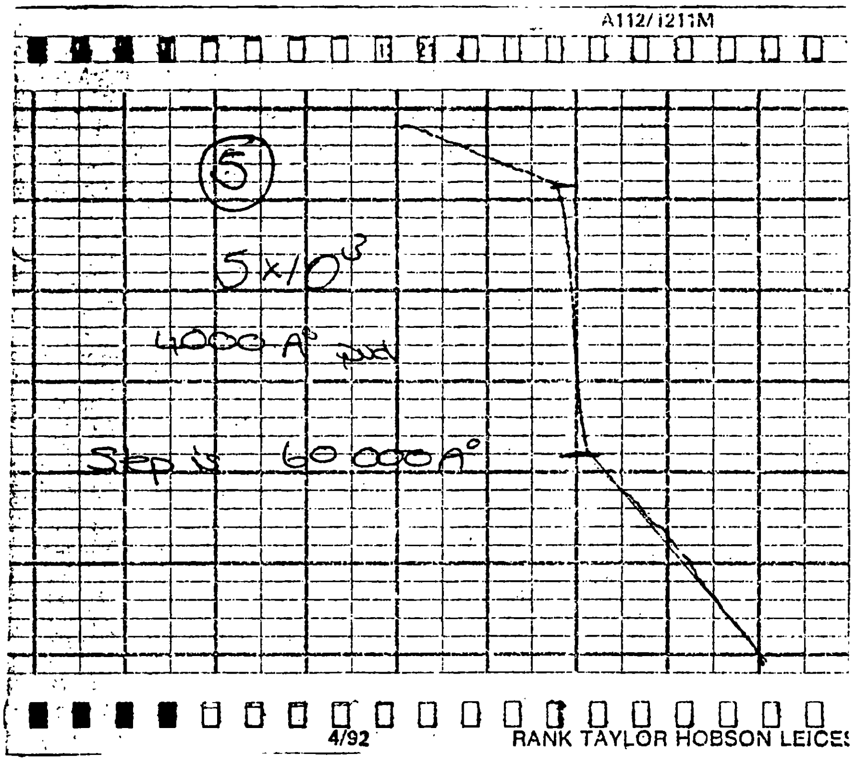

Figure 4.4 Taly step measurement of SiO_2-P_2O_5 film thickness following immersion in 'p-etch' for 20 hours.

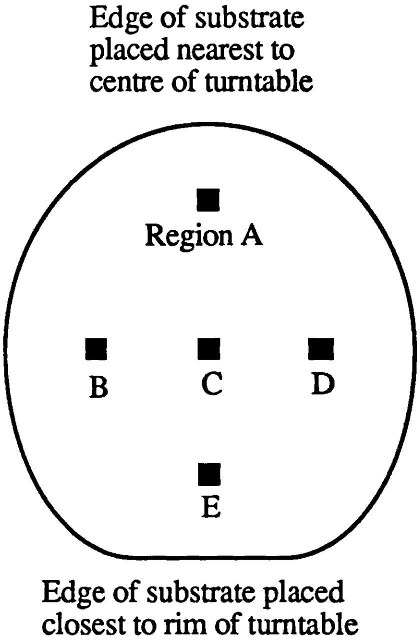

Figure 4.5 Diagram of selected areas for measurement of film thickness and refractive index on 3 inch diameter silicon substrate.

Region	Prism technique Film thickness (μm)	'p-etch' technique Film thickness (μm)
A	7.2	7.2
B	6.0	6.0
C	6.0	6.0
D	6.0	6.0
E	5.5	5.5

Table 4.1 Film thickness of selected regions measured by prism coupling and 'p-etch' techniques.

The refractive index of the film was also measured at each of the 5 sites at which the thickness was measured and found to be 1.467 for all the sites. Hence, the refractive index of the film was uniform across the substrate.

The refractive index of films fabricated with a constant $SiCl_4$ flow rate, but different PCl_3 flow rates, was also measured and is presented in figure 4.6. The increase in refractive index of the film relative to the substrate was found to be proportional to PCl_3 the flow rate. The different PCl_3 flow rates had no influence on the deposited film thickness.

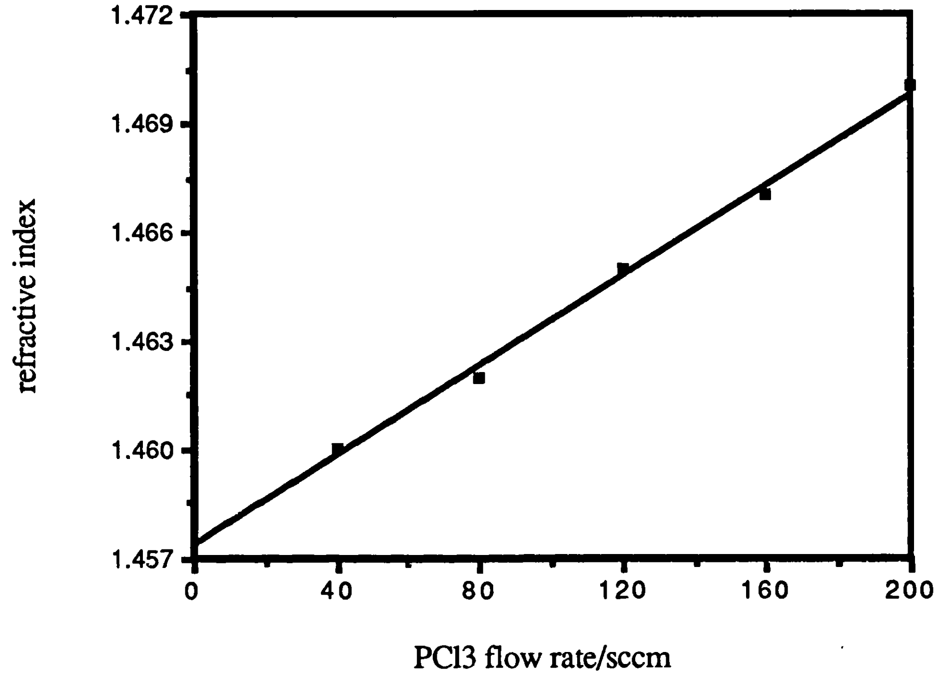

Figure 4.6 Refractive index of SiO_2-P_2O_5 film as a function of PCl_3 flowrate.

It was not possible to increase the PCl_3 flow rate greater than 200 sccm, as instead of glass soot being deposited, a gel was obtained on the substrate rendering the film unsuitable for consolidation. Hence, the maximum obtainable refractive index change of the film relative to the substrate was approximately 0.9 %, corresponding to a P_2O_5 concentration of approximately 45 wt% [13] .

4.8 Fabrication of Rare Earth Doped Planar Waveguides

4.8.1 Solution Doping Technique

The solution doping technique involved the deposited soot being partially sintered at a reduced temperature. The resultant porous structure was then immersed in an aqueous or alcohol solution of the required rare earth chloride, with the rare earth ions adsorbing onto the skeleton structure. The rare earth concentration incorporated was controlled by varying the solution strength and keeping the immersion time constant. The degree of partial sintering also determined the doping level and had to be controlled. After immersion the sample was dried and completely consolidated. The drying process was important to minimise the in-plane and out-of-plane scatter of the guides.

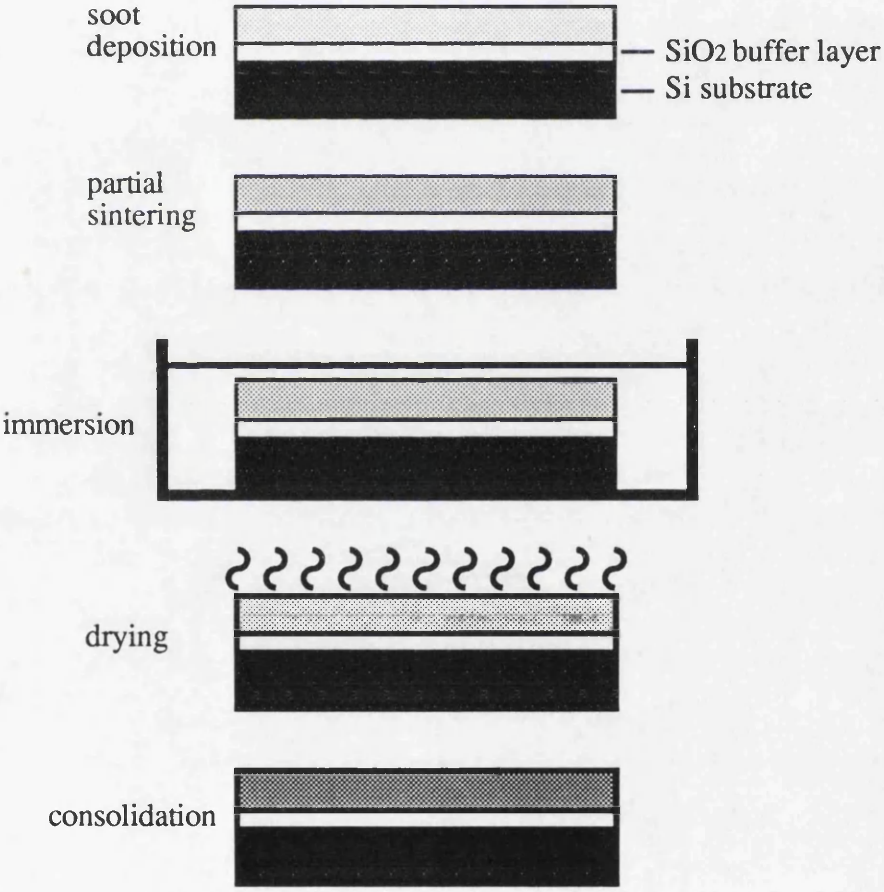

Figure 4.7 Schematic diagram of the different stages of the solution doping technique.

The degree of partial sintering was important in not only determining the doping level, but also to minimise the damage to the delicate glass structure on immersion in the solution. If the degree of partial sintering was too small, the skeleton structure was easily damaged, as shown in figure 4.8. On the other hand if the glass was too sintered there would be non-uniform distribution of the rare earth dopant. A suitable partial sintering condition for films fabricated using 150 sccm $SiCl_4$ and 160 sccm PCl_3 was found empirically to be produced by sintering at 960°C for 30 minutes, yielding a structure as exhibited in figure 4.9. Moreover, it is essential that the glass soot upon partial sintering did not form a cap of fully consolidated glass on top of partially sintered material, as shown in figure 4.10, as this would adversely affect the rare earth doping profile in the film and increase the scattering loss produced at the guide-clad interface. Finally, the solute had to be completely dissolved in the solvent in which the sample was immersed, otherwise particles precipitating onto the partially sintered sample hindered complete consolidation, as illustrated in figure 4.11, rendering the film unsuitable for optical purposes.

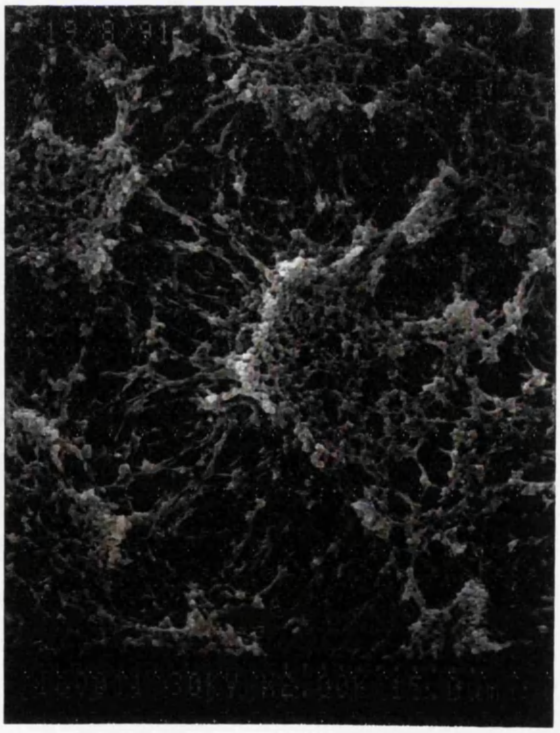

Figure 4.8 SEM photograph of damage to glass structure after immersion in solution.

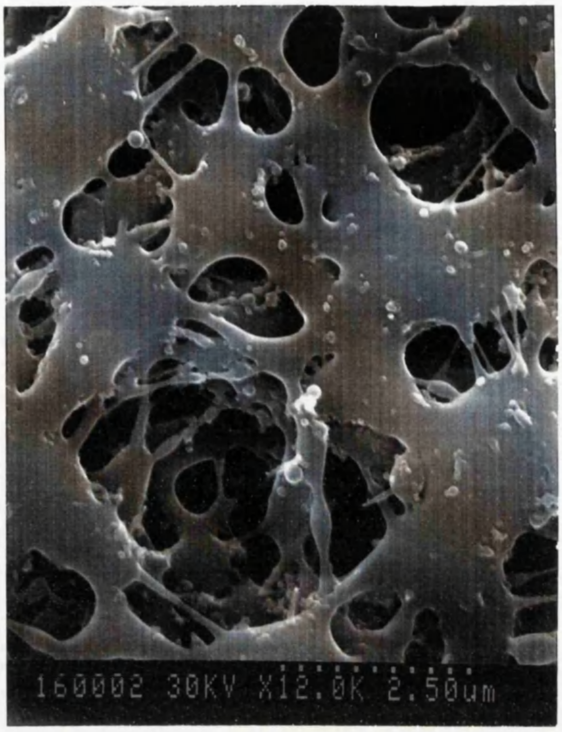

Figure 4.9 SEM photograph of suitable partial sintering structure for solution doping.

Figure 4.10 SEM photograph of partially sintered SiO_2-GeO_2-P_2O_5 glass film, with fully consolidated cap layer.

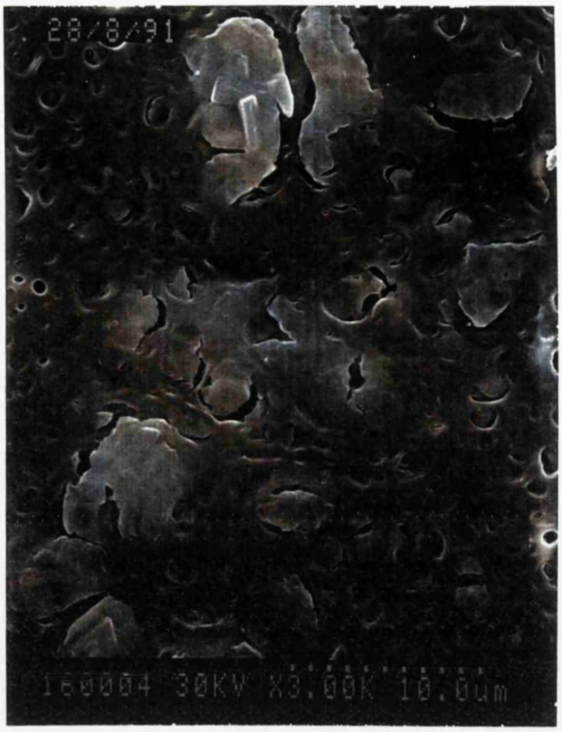

Figure 4.11 SEM photograph of SiO_2-P_2O_5 film consolidated at 1350°C for 2 hours, after immersion in 0.2 molar Al (NO_3) solution.

4.8.2 Aerosol Doping Technique

Rare earth ions can be directly incorporated into the soot during the deposition using an aerosol doping technique, making redundant the need to partially sinter the deposited soot and drying of the sample after immersion, as required by the solution doping technique [14]. A schematic diagram of the aerosol delivery system is given in figure 4.12.

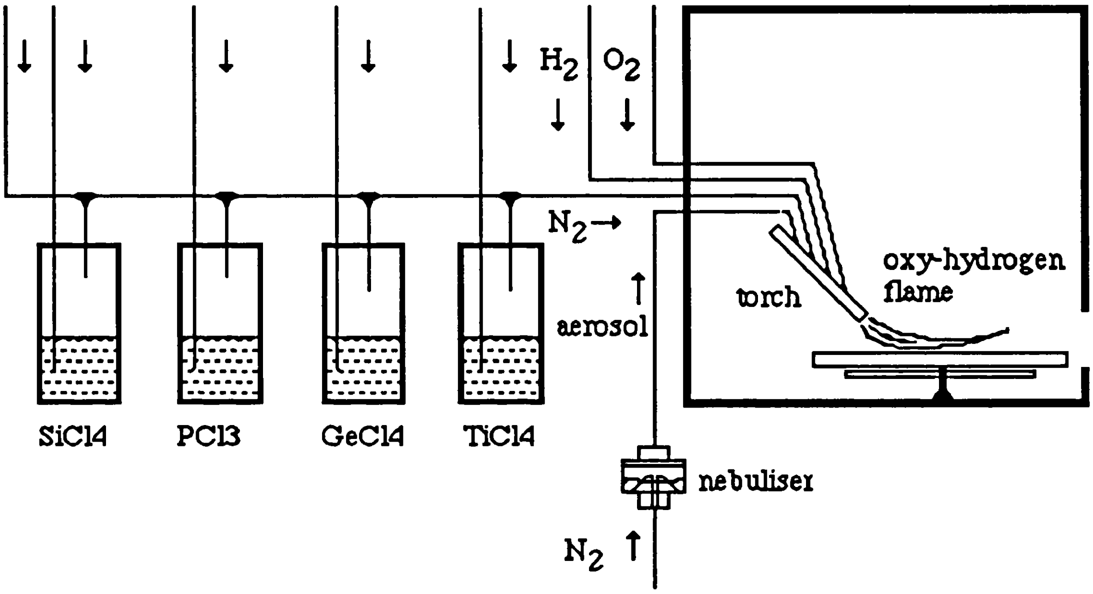

Figure 4.12 Schematic diagram of aerosol delivery system.

Rare earth ions were incorporated into the glass soot by feeding the torch with the aerosol of an aqueous solution of the required rare earth chloride. The aerosol generator was a PVC pneumatic atomiser and zero grade nitrogen gas was used to atomise the solution and to deliver the resultant aerosol droplets to the torch. The aerosol was not affected by gravitational settling and did not accrete inside the duct feeding the multi-conduit torch. The aerosol delivery rate was 0.3 ml/minute of solution for a nitrogen flow rate of 3 l/minute. Entrance of the rare earth chloride into the flame was confirmed by a change in the colour of the flame. For example when the aerosol of Er, Nd or Eu chloride was fed into the torch, the colour of the flame was green, violet, or red respectively. The rare earth dopant level incorporated into the glass was dependent on: the strength of the nebulised aqueous solution; the carrier gas flow rate transporting the aerosol to the torch; and the design and position of the torch with respect to the turn-table during the deposition.

The initial torch design used for aerosol doping was a modified three port torch. On feeding the aerosol into the inner conduit with the metal chlorides, low loss films with a rare earth concentration of approximately 0.5 wt% were formed, but the inner tube was susceptible to blockage, a consequence of the hydrolysis of the halides by the aerosol. Aerosol fed into the outermost conduit with oxygen produced films with extremely low rare earth doping levels. The aerosol was not fed into the middle conduit with hydrogen for safety considerations.

A four port torch produced more reproducible results. A schematic diagram of the four port torch used for aerosol doping is shown below.

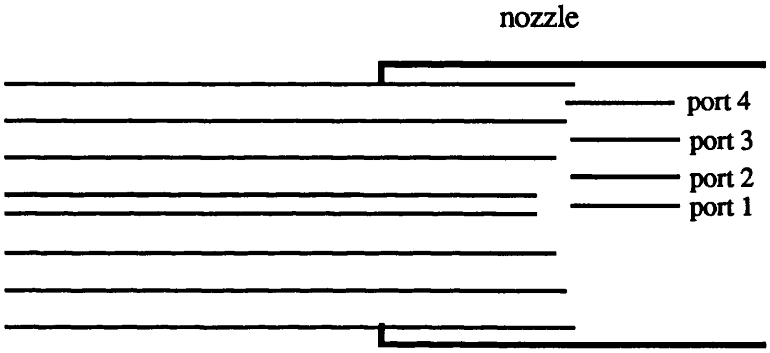

Figure 4.13 Schematic diagram of end-section of four port torch used for aerosol doping.

Best results for reproducibility of rare earth doping levels, quality of flame shape and deposition uniformity were achieved when the aerosol was fed into port 3, between the hydrogen in port 2 and the oxygen in port 4. When the aerosol was fed into port 2, hydrogen into port 3 and oxygen into port 4, the flame was too turbulent and produced poor soot deposition uniformity. In both cases the metal chlorides were fed into the central port 1. The soot deposition rate for the four port torch decreased by a third in comparison to the three port torch when using identical halide flow rates, torch and turn-table speeds. For a flow rate of 150 sccm of $SiCl_4$, a 0.5 µm film thickness per traversal after consolidation was obtained when using the four port torch. Furthermore, the refractive index difference of a film relative to the substrate fabricated using the four port torch was lower by approximately 20 % for identical PCl_3 flow rates in comparison to a film fabricated using the three port torch. The differences are thought to be due to different flame shape, greater flame turbulence and lower flame temperature resulting from the high nitrogen flow rate used as the carrier gas for the aerosol.

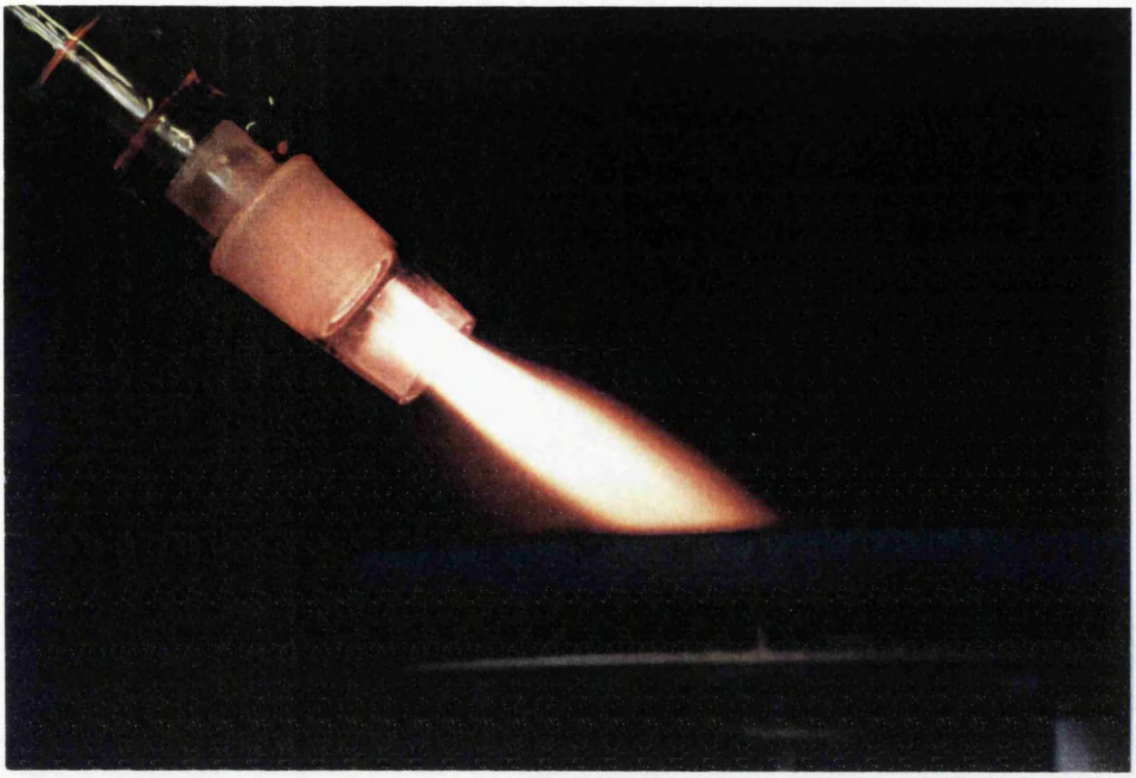

Figure 4.14 Photograph of the four port torch with aerosol of $EuCl_3$ being fed into port 3. The colour of the flame is red.

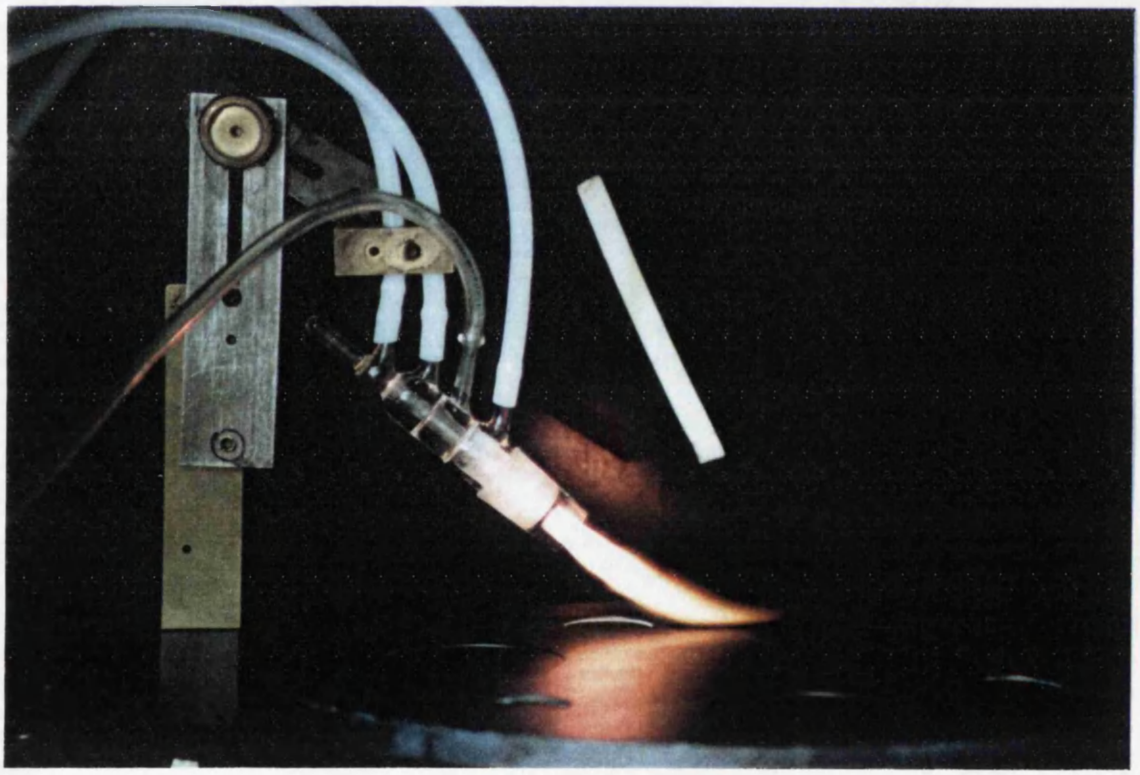

Figure 4.15 Photograph of flame when nebulised 0.2 molar $NdCl_3$ solution fed to four port torch.

4.9 Guided Wave Losses In Dielectric Slab Waveguides

The theoretical analysis presented for guided modes in a dielectric waveguide assumed there was no attenuation of the guided mode. However, the optical power of a guided mode decays as exp $(-\alpha z)$ in the propagation direction, where α is the attenuation coefficient. There are several possible causes for the attenuation of the mode, including absorption, scattering and leakage.

Absorption of the light may be intrinsic, caused by interaction of the light with the glass components or extrinsic, due to impurities. For high silica glass, there are strong absorption bands in the infrared and far infrared (5 - 50 μm) due to oscillations of the structural units within the glass. In the ultraviolet, electronic transitions cause strong absorption bands. Between these two regions, there is a transmission window in the visible and near infrared where absorption loss results from the presence of the hydroxyl group OH^- and impurities, such as the transition metal ions [15].

Scattering loss arises from an inhomogeneity of the refractive index and from interface irregularities. Volume scattering is produced by inhomogeneities arising from density and compositional fluctuations, which gives rise to variations of the dielectric constant. This can result in coupling of guided modes to the continuum of radiation modes of the waveguide and hence contribute to the attenuation of the guided mode. The magnitude of the attenuation coefficient is dependent on the dielectric material and the size of the scattering particles. Rayleigh scattering is caused by inhomogeneities smaller than the wavelength of light and the scattering component , α_{sc}, due to density fluctuations is given by :

$$\alpha_{sc} \approx \frac{8\pi^3}{3\lambda^4} n^8 p^2 \xi T_g \tag{4.30}$$

where p is the average photoelastic constant, ξ is the isothermal compressibility and T_g is the glass transition temperature [15].

Surface scattering is produced by imperfections at the interface between the waveguide and the substrate or cladding layers, causing coupling between the guided mode and another guided mode or the continuum of radiation modes. Coupling between two guided modes does not contribute directly to the loss of energy, however coupling between a guided mode and the continuum of radiation modes does produce an energy loss.

Theoretical treatments are available for scattering in planar waveguides, using the assumption that the region over which the variation in the refractive index takes place is much shorter than the wavelength of the light [1,16,17]. Tien's formula for the scattering loss α of an asymmetric planar waveguide can be written as:

$$\alpha = \frac{2\left(\sigma_{fs}^2 + \sigma_{fc}^2\right)k^3}{\beta\left(W + \frac{1}{\gamma_s} + \frac{1}{\gamma_c}\right)} \qquad (4.31)$$

where σ_{fs} and σ_{fc} are the interface roughness variance at the film-substrate and film-clad interfaces respectively. In general, the scattering loss increases with increasing index difference between the film and substrate or clad, decreasing guiding layer thickness, increasing mode number and the square of the interface roughness. Numerical evaluation of (4.31) indicates that the scattering loss for a symmetric waveguide scales approximately as W^{-3} for sufficiently thick structures with fixed index difference between the guide and the cladding layer and as the difference in dielectric constants.

Waveguide loss due to leakage occurs when the waveguide is supported on a substrate of equal or greater refractive index. This situation is present when a silicon substrate is used to support a high silica film, as silicon has a refractive index of 3.75. To minimise leakage loss, a SiO_2 layer is grown as a buffer layer, the necessary thickness of the buffer layer determined by the refractive index and thickness of the waveguide film. The leakage induced propagation loss of the fundamental TE mode is given by:

$$\alpha \approx \lambda^3 k \gamma_s^3 \sin^2(kW) \exp\left(-2\gamma_s T\right) / \pi^3 n_f\left(n_f^2 - n_s^2\right) W \qquad (4.32)$$

where T is the thickness of the buffer layer [16]. Therefore, the attenuation coefficient due to leakage decreases exponentially with increasing buffer thickness. For SiO_2-P_2O_5 films fabricated by FHD, a buffer layer thickness of 10 μm is required to maintain leakage loss below 0.01 dB/cm.

4.10 Loss Measurement Techniques

Several methods have been used to measure the losses of planar waveguides [18-20]. The methods adopted to measure the losses of passive and rare earth doped planar high silica films fabricated by FHD were the three-prism technique [21] and the fibre-probe technique [22].

4.10.1 Three-Prism Technique

The three-prism technique involved light from a 4.8 mW He-Ne 632.8 nm laser being prism coupled into the planar waveguide. The TE polarised guided light was coupled out of the waveguide by two further prisms, the position of the third prism being fixed. It was essential that the coupling efficiencies of the first and the third prisms remained constant throughout the measurement. This was accomplished by connecting the first and third prisms to the rotating turn-table and ensuring that the synchronous direction was maintained throughout the experiment. The central prism was moved between the two outer prisms, coupling light out at different positions along the waveguide. The experimental arrangement for the three-prism technique is illustrated in figure 4.16.

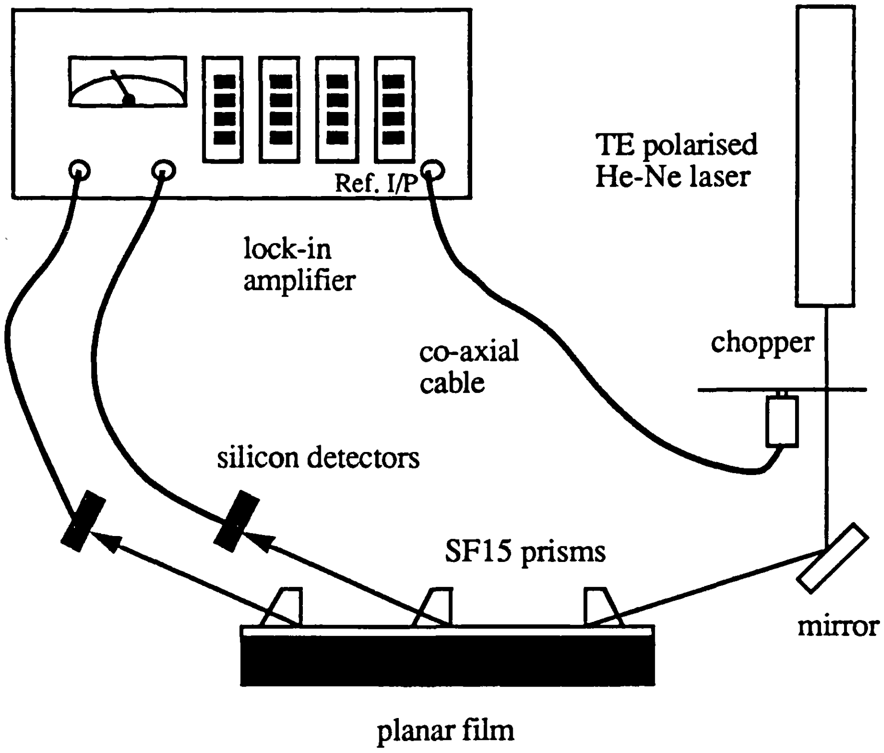

Figure 4.16 Three-prism technique for measuring loss of planar film.

The three-prism technique involved the power output, $P^o{}_3$, from the third prism being measured with no output coupling from the central prism. With output coupling from the the central prism, the power output was measured for the second prism, $P_2(z)$ and the third prism, $P_3(z)$. Lock-in detection was used to measure the power levels. The separation between the first and second prism was then measured using a calliper. On removing the coupling from the central prism, the power output from the third prism was remeasured to ensure that the coupling efficiencies of the first and third prisms remained constant. This process was repeated for a number of different positions of the second prism along the waveguide. It can be shown that the guided light power , P(z), is independent of the coupling efficiency of the second prism and is given by:

$$P(z) = \frac{P_2(z) . P_3^o}{P_3^o - P_3(z)} \qquad (4.33)$$

The loss of the planar waveguide can be found by plotting P(z) as a function of propagation distance.

4.10.2 Fibre-Probe Technique

The second method used to measure the attenuation of planar rare earth doped silica waveguides was the fibre-probe technique. This method is based on the assumption that at any point along the waveguide, the intensity of the out of plane scatter is proportional to the guided light intensity at that point. Therefore, a measurement of the scattered light distribution along the propagation direction gives the attenuation of the guide.

The experimental set-up for the fibre-probe technique is illustrated in figure 4.17. The incident laser beam was prism coupled into the waveguide, with a 1 mm diameter plastic fibre used as a probe. The angle and the distance of the probe from the waveguide surface was kept constant throughout the measurement. The coupling efficiency of the input prism was also kept constant. To obtain the attenuation of the waveguide, the intensity of the out of plane scatter was measured at several different points along the waveguide. At each point, the probe was scanned in a lateral direction across the guided wave streak to obtain a profile of the scattered light. The maximum signal measured in the lateral profile was chosen to be proportional to the guided light wave intensity at that point. Lock-in techniques were used to measure the intensity of the out of plane scatter.

The fibre probe technique has the advantage that it is a relatively simple configuration and is a non-contact measurement. However, measurement was not possible in low loss high quality waveguides which exhibit no out of plane scatter.

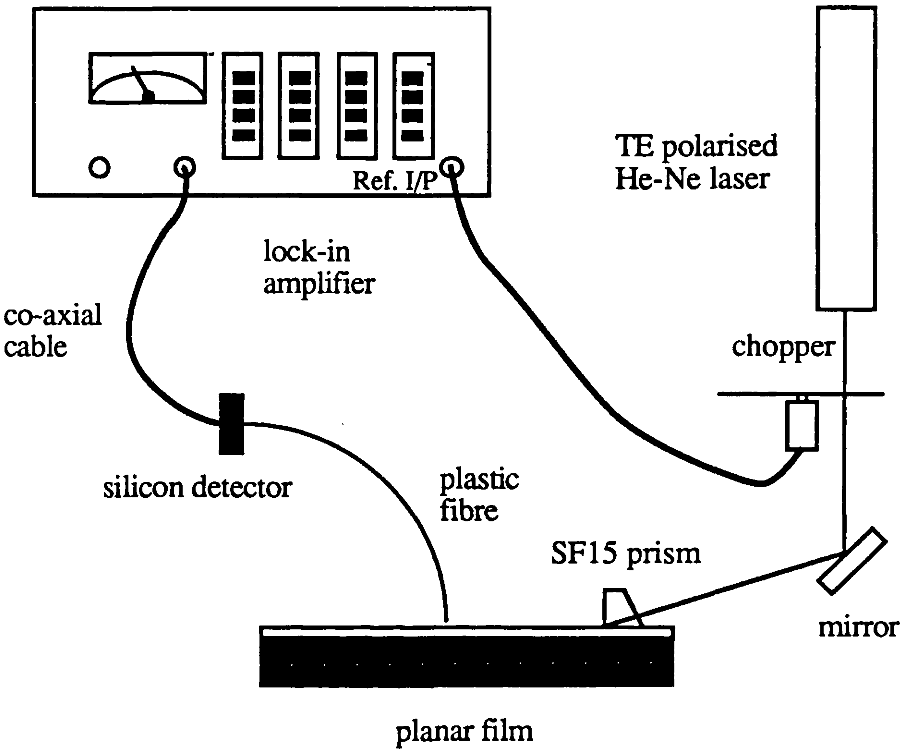

Figure 4.17 Fibre-probe technique for measuring propagation loss.

4.10.3 Loss Measurement Results

This section presents the results of loss measurements for the TE fundamental mode of passive and rare earth doped planar films at 632.8 nm using a helium-neon laser. The first four loss measurements presented are for 4 µm thick SiO_2-GeO_2-P_2O_5 films, which had a refractive index of 1.475. The films were fabricated using 150 sccm $SiCl_4$, 160 sccm PCl_3 and 40 sccm $GeCl_4$; partially sintered at 1000°C for 15 minutes; and fully sintered at 1280°C for 1 hour. The second set of results are for 6 µm thick SiO_2-P_2O_5 films, with a refractive index of 1.467. The films were fabricated using 150 sccm $SiCl_4$ and 160 sccm PCl_3; partially sintered at 960°C for 30 minutes and fully sintered at 1300°C for 2 hours.

The loss measured for the SiO_2-GeO_2-P_2O_5 film using the three-prism technique was 0.4 dB/cm. The loss for a SiO_2-GeO_2-P_2O_5 film partially sintered, immersed in an alcohol solution for 15 minutes and dried by spinning at 3000 rpm for 60 seconds and placed on a hot plate set at 90°C for 5 minutes before final sintering, as shown in figure 4.18, was 0.6 dB/cm. The increase in loss compared to the passive film is thought to be due to damage to the glass structure on immersion in the solution and the drying process. For a sample which was not spun dry after immersion, but dried by placing on a hot plate, the propagation loss was measured to be 1.1 dB/cm. A similar loss figure was measured for samples blown dry with nitrogen gas. The drying process was therefore identified to be an important factor in minimising the propagation losses.

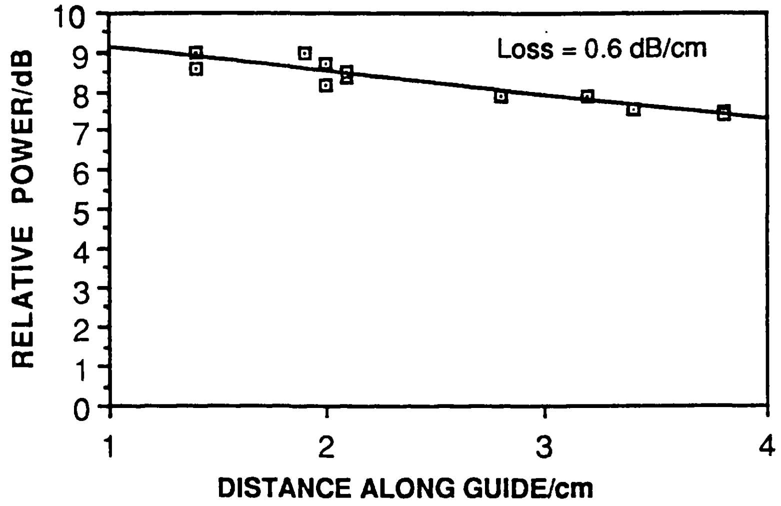

Figure 4.18 Loss measurement for film immersed in alcohol, spun and dried on hot plate using three-prism technique. (SiO_2-GeO_2-P_2O_5 film)

On incorporating 0.1 wt% Er in a SiO_2-GeO_2-P_2O_5 film, by immersing the partially sintered film in a 0.01 molar $ErCl_3$ solution for 5 minutes and drying by spinning at 3000 rpm for 60 seconds and heating at 90°C on a hot plate for 5 minutes, the propagation loss was found to be 0.9 dB/cm. The increase in loss over the sample which was immersed in alcohol and spun dry, is due to scattering of light from the non-uniform distribution of rare earth ions.

For the binary glass SiO_2-P_2O_5, the propagation loss using the three-prism technique, was measured to be below 0.1 dB/cm. A photograph of a SiO_2-P_2O_5 film, with the fundamental mode propagating is given below in figure 4.19, exhibiting no out of plane scatter.

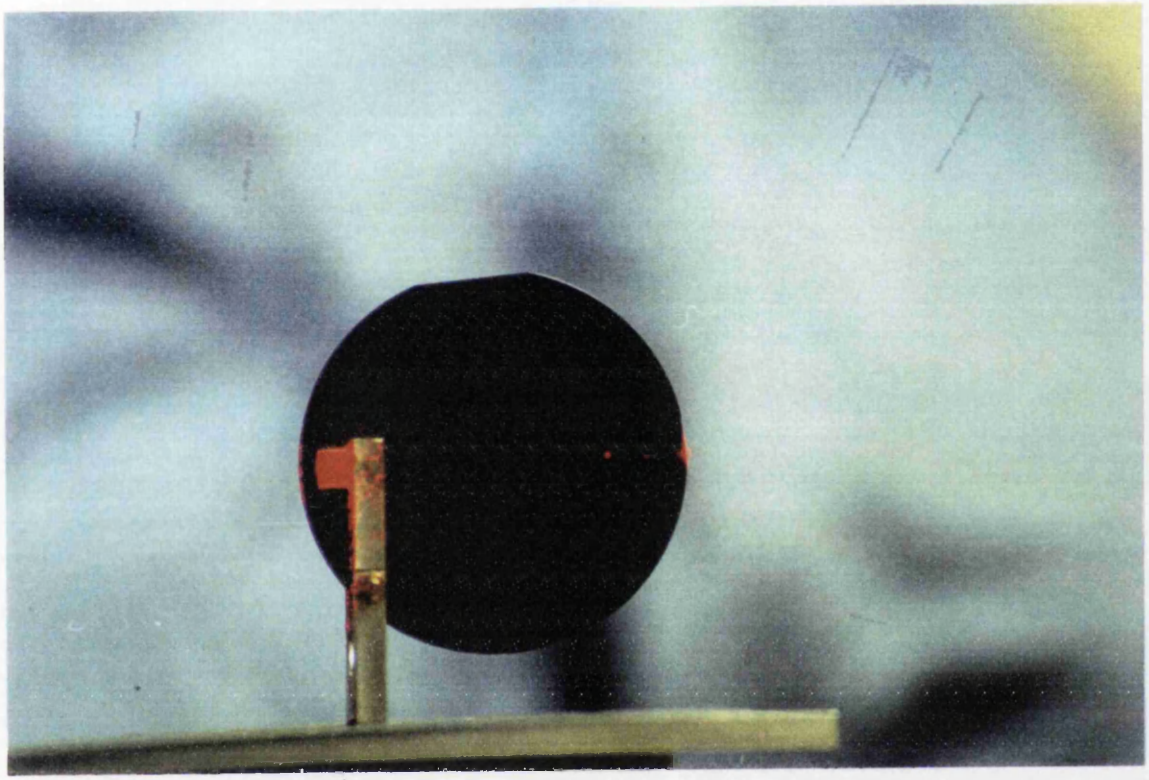

Figure 4.19 Photograph of fundamental mode propagating in passive SiO_2-P_2O_5.

For SiO_2-P_2O_5 films, the propagation loss for samples immersed in 0.02 molar $NdCl_3$ solution incorporating 0.4 wt% Nd in the glass, was determined to be 0.4 dB/cm using both the fibre-probe and three-prism technique. The loss measurement using the fibre-probe technique is presented in figure 4.20. The increase in loss of the rare earth doped sample over the passive film is due to increased volume scattering. The loss of SiO_2-P_2O_5 films, with comparable rare earth doping levels fabricated by the aerosol doping technique, was 0.3 dB/cm. However, for a film immersed in a 0.04 molar $NdCl_3$ solution yielding a Nd concentration of 0.6 wt%, the loss was measured to be 1.1 dB/cm. The increase in loss to 1.1 dB/cm, compared to 0.4 dB/cm for samples with approximately half the rare earth doping level, indicates that propagation loss is sensitive to the rare earth doping level, increasing with increasing rare earth concentration.

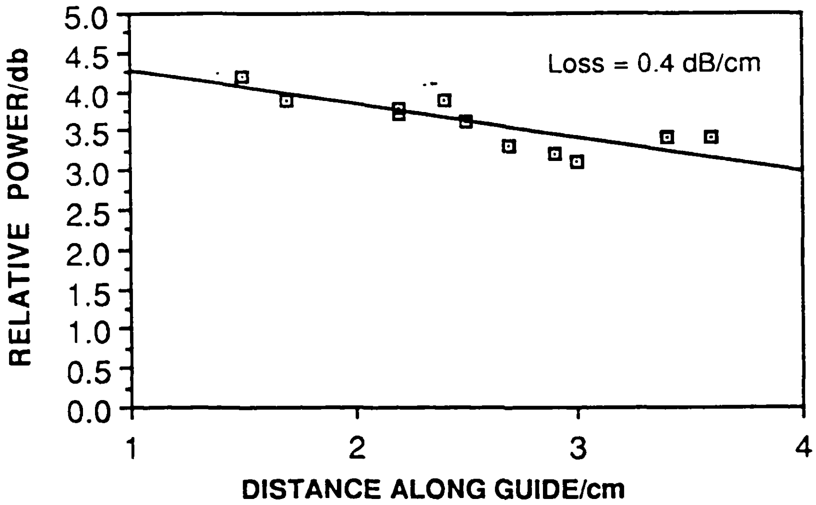

Figure 4.20 Loss measurement for film immersed in 0.02 molar $NdCl_3$ solution and spun dry using fibre-probe technique. (SiO_2-P_2O_5 film)

Finally, for a 0.1 wt% Nd doped SiO_2-P_2O_5 film, fabricated by the aerosol doping technique, with a P_2O_5 dopant level 25 % lower than films which have been previously reported in this section, the loss was measured to be 0.6 dB/cm using the fibre-probe technique. It may be concluded that the loss of rare earth doped samples is also dependent on the P_2O_5 doping levels and hence the solubility of the rare earth ions in the glass matrix. A summary of the loss measurement results is presented below in table 4.2.

Film Composition	Film Processing	Measurement Technique	Loss (dB/cm)
SiO_2-P_2O_5-GeO_2	none	3-prism	0.4
SiO_2-P_2O_5-GeO_2	Immersed in alcohol for 15 minutes Spun dry: 3000 rpm 60 s Hot plate: 90°C 5 minutes	3-prism	0.6
SiO_2-P_2O_5-GeO_2	Immersed in alcohol for 15 minutes Hot plate: 90°C 5 minutes	3-prism	1.1
SiO_2-P_2O_5-GeO_2	Immersed in 0.01 M $ErCl_3$ alcohol solution for 15 mins Spun dry: 3000 rpm 60 s Hot plate: 90°C 5 minutes	3-prism	0.9
SiO_2-P_2O_5	none	3-prism	< 0.1
SiO_2-P_2O_5	aerosol doping	3-prism	0.3
SiO_2-P_2O_5	Immersed in 0.02 M $NdCl_3$ alcohol solution for 15 mins Spun dry: 3000 rpm 90 s Hot plate: 90°C 5 minutes	3-prism fibre-probe	0.4 0.4
SiO_2-P_2O_5	Immersed in 0.04 M $NdCl_3$ alcohol solution for 15 mins Spun dry: 3000 rpm 90 s Hot plate: 90°C 5 minutes	3-prism	1.1

Table 4.2 Loss measurements for TE fundamental mode of planar films at 632.8 nm.

4.11 Conclusion

The homogeneity of the thickness and refractive index of SiO_2-P_2O_5 films fabricated by FHD was investigated. For a continuous traversal speed of the torch, film thickness varied by 17%, but the inhomogeneity in the refractive index was below 0.1%. The large variation in film thickness can be dramatically reduced by increasing the speed of the torch in increments during the traversal as the torch approaches the centre of the turn-table.

Rare earth doping of the SiO_2-P_2O_5 films was accomplished by the solution doping technique and for the first time in the planar format, an aerosol doping technique. The propagation losses of the resultant planar films were found to be dependent on the processing steps involved in the solution doping technique and the solubility of the rare earth ions in the glass matrix, which was dependent on the rare earth concentration and the P_2O_5 codoping level. The losses of rare earth doped films fabricated by the solution doping and the aerosol doping techniques with comparable doping levels ~~was~~ were similar. Therefore, the aerosol doping technique exhibited the capability of being able to produce low loss films, similar to the solution doping technique, but had the added advantage of being able to incorporate the rare earth ions directly into the glass matrix during the deposition.

4.12 References

1. Tien, P. K.
   Appl. Opt., 1971, **10**, 2395.
2. Kogelnik, H.
   Integrated Optics; Ed. T. Tamir, 15 - 81.
   Topics In Applied Physics, **7**, Springer- Verlag, 1975.
3. Hunsperger, R. G.
   Integrated Optics: Theory and Technology.
   Springer- Verlag.
4. Lee, D. L.
   Electromagnetic Principles of Integrated Optics.
   John Wiley & Sons, Inc., 1986.
5. Nishihara, H., Haruna, M., and Suhara, T.
   Optical Integrated Circuits.
   McGraw-Hill, 1989.
6. Yariv, A.
   Optical Electronics.
   New York: Holt, Rhinehart, and Winston.
7. Tien, P. K., and Ulrich, R.
   J. Opt. Soc. Am., 1970, **60**, 1325.
8. Dalgoutte, D. G., and Wilkinson, C. D. W.
   Appl. Opt., 1975, 14, 2983.
9. Tien, P. K., and Martin, R. J.
   Appl. Phys. Lett., 1971, **18**, 398.
10. Ulrich, R., and Torge, R.
    Appl. Opt., 1973, **12**, 2901.
11. Tien, P. K., Ulrich, R., and Martin, R. J.
    Appl. Phys. Lett., 1969, **14**, 291.
12. Pliskin, W. A., and Gnall, R. P.
    J. Electrochem. Soc., 1964, **111**, 872.
13. Gambling, W. A., Payne, D. N., Hammond, C. R., and Norman, S. R.
    IEE Proc., 1976, **123**, 570.
14. Bebbington, J. A., Barbarossa, G., Bonar, J. R., and Aitchison, J. S.
    Appl. Phys. Lett., 1993, ,1992.
15. Beales, K. J., and Day, C. R.
    Phys. & Chem. Glasses, 1980, **21**.

16. Deri, R. J., and Kapon, E.
IEEE J. Quantum. Electron., 1991, **27**, 626.

17. Marcuse, D.
Bell Syst. Tech. J., 1969, **48**, 3233.

18. Weber, H. P., Dunn, F. A., and W. N. Leibolt.
Appl. Opt., 1973, **12**, 755.

19. Jackel, J. L., and Veselka, J. J.
Appl. Opt, 1984, **23**, 197.

20. Okamura, Y., Yoshinaka, S., and Yamamoto, S.
Appl. Opt., 1983, **22**, 3892.

21. Won, Y. H., Jaussaud, P. C., and Chartier, G. H.
Appl. Phys. Lett., 1980, **37**, 269.

22. Nourshargh, N., Starr, E. M., Fox, N. I., and Jones, S. G.
Electron. Lett., 1985, **21**, 818.

Chapter 5 Rare Earth Doped Silica Channel Waveguides

5.1 Introduction

Chapter 5 reviews the basic theory of dielectric channel waveguides and discusses in detail the fabrication of silica channel waveguides achieved through a combination of photolithographic and RIE processes. Three different RIE processes were investigated, assessing etch rate and quality for passive and rare earth doped SiO_2-P_2O_5 films. An annealing process after the RIE is also reported which was developed to further reduce the scattering loss of the channel waveguides. Details of the cladding process using a SiO_2-B_2O_3-P_2O_5 glass composition are also given.

Optical assessment of the channel waveguides was also carried out. Fluorescence and absorption spectra were obtained for both Nd^{3+} and Er^{3+} doped SiO_2-P_2O_5 waveguides. Fluorescence lifetime measurements concentrated on Er^{3+} doped SiO_2-P_2O_5 samples fabricated by solution and aerosol doping techniques, investigating the dependency of the lifetime on doping levels and fabrication conditions. Loss measurements were performed for channel waveguides with SiO_2-B_2O_3-P_2O_5 glass or air as the cladding layer. Finally, the experimental arrangement used to investigate Nd^{3+} doped SiO_2-P_2O_5 waveguide lasers is described and the demonstration of cw oscillation reported.

5.2 Dielectric Channel Waveguides

Light in channel or three dimensional waveguides is confined not only along the depth, but is also confined in the y-direction, as depicted in figure 5.1, where n_1 is greater than n_j, with $j = 2, .., 5$. Consequently the guided mode does not experience diffraction.

Dielectric channel waveguides do not support purely TE or TM modes, but instead two sets of hybrid modes, which have the principal polarisation component along the x or y directions. The mode which has the electric field mainly in the x-direction is classified as a E^x_{pq} mode and resembles the TM mode of a planar waveguide. Although E_x is much greater than E_y and E_z, E_y and E_z are always present in the waveguide core, region 1 in figure 5.1. The subscripts p and q refer to the number of nodes of the electric field E_x in the x and y-directions. An E^y_{pq} mode has the main electric field polarised in the y-direction and is a TE-like mode.

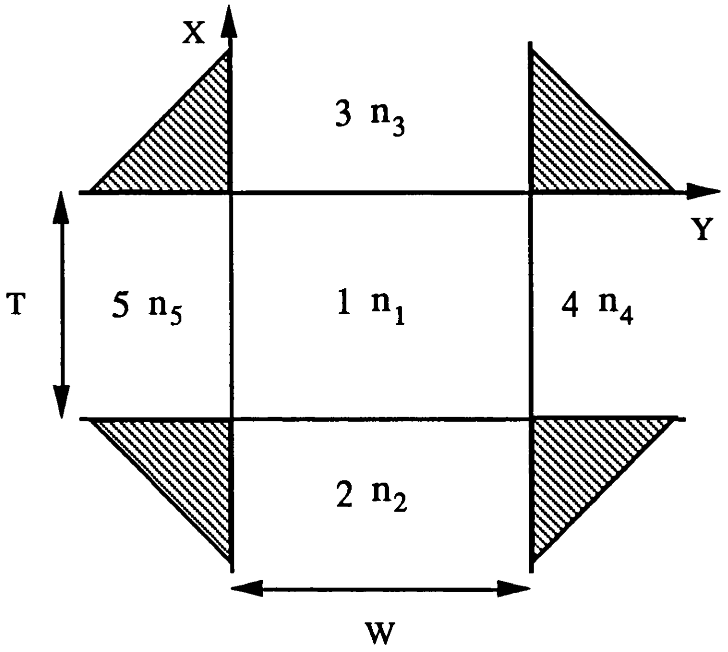

Figure 5.1 Schematic diagram of channel waveguide.

An exact analytical treatment of the waveguide structure shown in figure 5.1 is not possible and numerical analysis is required for an accurate solution [1,2]. However, an approximate analytical solution can be obtained by assuming the guided mode is far from cut-off and that most of the optical power is confined in region 1 [3]. As a result, only a small fraction of the light propagates in regions 2, 3, 4 and 5 and the field in the shaded regions of figure 5.1 may be neglected, with only a small error incurred in the calculation.

For an E^x_{pq} mode, the main field components are E_x and H_y, with H_x approximated to be zero. The wave equation can be solved by applying the boundary conditions that E_x and H_z are continuous on the interfaces y = - W/2 and y = W/2 and that H_y and E_z are continuous on x = 0 and x = T. The propagation constant β in the z-direction may then be written as:

$$\beta = \left(n_1^2 k^2 - k_x^2 - k_y^2\right)^{\frac{1}{2}} \tag{5.1}$$

where k_x and k_y are propagation constants in the x and y directions in the core and are solutions of the transcendental equations:

$$k_xT = p\pi + \tan^{-1}\left(\frac{n_1}{n_2}\right)^2\left(\frac{\gamma_{x2}}{k_x}\right) + \tan^{-1}\left(\frac{n_1}{n_3}\right)^2\left(\frac{\gamma_{x3}}{k_x}\right) \qquad (5.2)$$

$$k_yW = q\pi + \tan^{-1}\left(\frac{\gamma_{y4}}{k_y}\right) + \tan^{-1}\left(\frac{\gamma_{y5}}{k_y}\right) \qquad (5.3)$$

where:

$$\gamma_{x2}^2 = \left(k_y^2 + \beta^2\right) - n_2^2k^2 \qquad (5.4)$$

$$\gamma_{x3}^2 = \left(k_y^2 + \beta^2\right) - n_3^2k^2 \qquad (5.5)$$

$$\gamma_{y4}^2 = \left(k_x^2 + \beta^2\right) - n_4^2k^2 \qquad (5.6)$$

$$\gamma_{y5}^2 = \left(k_x^2 + \beta^2\right) - n_5^2k^2 \qquad (5.7)$$

The reciprocals of the decay constants, given in equations (5.4) to (5.7), give the penetration depths of the electric field into each region.

Following a similar procedure for E^y_{pq} modes, putting $E_x = 0$ into Maxwell's equations and applying the appropriate boundary conditions, the transcendental equations below are derived:

$$k_xT = p\pi + \tan^{-1}\left(\frac{\gamma_{x2}}{k_x}\right) + \tan^{-1}\left(\frac{\gamma_{x3}}{k_x}\right) \qquad (5.8)$$

$$k_yW = q\pi + \tan^{-1}\left(\frac{n_1}{n_4}\right)^2\left(\frac{\gamma_{y4}}{k_y}\right) + \tan^{-1}\left(\frac{n_1}{n_5}\right)^2\left(\frac{\gamma_{y5}}{k_y}\right) \qquad (5.9)$$

From the transcendental equations given above, the propagation constant β may be calculated and consequently the field patterns for the propagating mode may be deduced.

The horizontal electric field distributions for the E^y_{00} fundamental mode of rare earth doped SiO_2-P_2O_5 channel waveguides fabricated by FHD and RIE and used to demonstrate planar oscillators and amplifiers are ilustrated below in figures 5.2 and

5.3. The numerical calculations were performed using the the Fwave III computer program written by M.R.S. Taylor, which was based on a finite difference implementation of the vector electromagnetic wave equation. Fwave III produces contour plots of the magnitude of the electric field strength, each contour line further from the core centre indicating a 10% drop in the strength of the electric field from the peak value. The electric field profile shown in figure 5.2 was calculated for the fundamental mode of a 7 μm deep, 8 μm wide channel waveguide, with a relative index difference between the core and cladding of 1.2%. Er^{3+} doped SiO_2-P_2O_5 channel waveguides with the given specifications were used as integrated optical amplifiers at 1.535 μm. The second field profile given in figure 5.3, calculated for a wavelength of 1.05μm, is for a 6 μm deep, 6 μm wide channel waveguide with an index difference between the core and the cladding of 1%. It was with this design of waveguide that cw oscillation was achieved with Nd^{3+} doped SiO_2-P_2O_5 and is reported in this thesis.

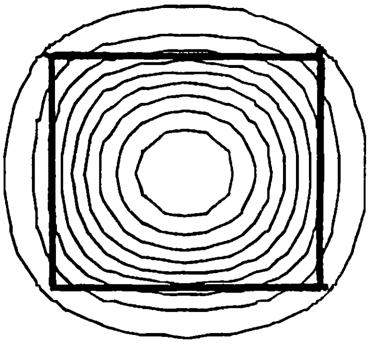

Figure 5.2 Electric field distribution of mode at wavelength of 1.535 μm in channel waveguide with cross-section of 7μm by 8 μm.

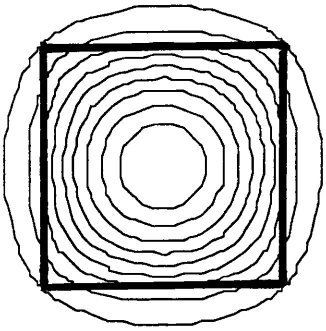

Figure 5.3 Electric field distribution of mode at wavelength of 1.05 μm in channel waveguide with cross-section of 6 μm by 6 μm

5.3 Channel Waveguide Fabrication

Channel waveguides have been formed in a wide range of materials by a variety of techniques including dry etching, wet etching, thermal diffusion, ion exchange and ion implantation. Fabrication of channel waveguides by the conventional ion exchange process in high silica glass is not possible because the glass is composed of network former oxides, namely SiO_2 with GeO_2, TiO_2, P_2O_5 and B_2O_3 dopants. However, silica channel waveguides may be formed by a combination of photolithography and RIE techniques which has the advantage of producing waveguides with a well defined core structure and almost perfect field matching to silica optical fibres [4].

5.3.1 Photolithography

A photolithographic process was used to generate the patterns for the optical waveguides, involving the exposure of selected areas of an ultra violet sensitive polymer coating a planar waveguide film [6]. The pattern was defined by placing a mask, on which the original pattern was present, in direct contact with the surface of the photoresist film and exposing the sample to ultra violet radiation. Contact printing ensured accurate pattern reproduction by minimising the diffraction of the ultra violet radiation between the mask and photoresist. After exposure, the photoresist was developed, resulting in the mask pattern being transferred onto the photoresist.

There are two types of mask: a light field mask, on which the pattern is defined by the opaque areas; and a dark field mask, on which the pattern is detailed by the transparent regions. There are also two forms of photoresist: a negative type, in which the exposed areas remain after development; and a positive type, in which the exposed area is removed after development. In general, work in this project concentrated on the use of a positive photoresist used in conjunction with a light field mask to form patterns for straight ridge waveguides 5 cm long, with widths ranging from 5 to 25 μm, each individual guide separated by 100 μm.

Prior to coating the sample with photoresist, the sample was cleaned to improve the adhesion of the photoresist and remove any particulate contamination. The standard cleaning procedure used in a cleanroom was:

1) 5 minute ultrasonic bath with Opticlear.
2) Rinse with acetone.
3) 5 minute ultrasonic bath with acetone.

4) Rinse with methanol.
5) 5 minute ultrasonic bath with methanol.
6) Rinse with RO water.
7) Blow dry with nitrogen.
8) Dry for 10 minutes on hot plate.

To improve the adhesion of the photoresist further, a primer was spun onto the sample. The sample was then covered in photoresist using a filtered syringe with 0.2 μm pores and spun to produce a uniform coating. The thickness of the photoresist film was determined by the spin speed, keeping the spin time constant. The photoresist was then pre-baked in an oven to vaporise the solvent and to enhance adhesion. Typical parameters for the Shipley 1400-31 resist are listed in table 5.1.

Parameter	
Resist Primer	Hexamethyl disilazine (HMDS)
Spin Speed	4000 rpm
Spin Time	30 seconds
Resist Thickness	1.8 μm
Pre-bake Temperature	90°C
Pre-bake Time	30 minutes

Table 5.1 List of photolithographic parameters for S1400-31 photoresist.

Exposure of the samples was carried out using a Hybrid Technology Group (HTG) mask aligner or a contact printer. After exposure of the sample to ultra violet radiation, the photoresist was developed. Careful examination of the photoresist edge profile and designed markers enabled accurate determination of correct exposure and development times. A list of typical exposure and development times are given below in table 5.2.

The final stage of the photolithographic process was to post-bake the samples at 120°C for 20 minutes to harden the remaining patterned photoresist, in preparation for etching.

For certain RIE processes a more rugged mask than photoresist is required. Such a mask may be formed using a thin metal film. In this case, a dark field mask was used in combination with positive photoresist and the 30 minute pre-bake was replaced by the following sequence of steps: 15 minute pre-bake; a 15 minute soak in chlorobenzene; followed by a further 15 minute pre-bake. After exposure and development, the sample was given a low pressure oxygen etch for 4 minutes to guarantee complete removal of the photoresist which had been exposed. A metal film of 200 Å of titanium, followed by 1500 Å of nickel was then evaporated onto the sample. The metal mask was produced by 'lift-off', immersing the sample in acetone and thus removing the remaining photoresist. Figure 5.4 illustrates the processing steps involved in both methods.

Mask Aligner	
Resist Thickness	1.8 μm
Exposure Time	10 seconds
Developer	1 : 1 Shipley AZ Developer : Water
Development Time	75 seconds
Contact Printer	
Resist Thickness	1.8 μm
Lamp Current	24 mA
Exposure Time	7 minutes
Developer	1 : 1 Shipley AZ Developer : Water
Development Time	75 seconds

Table 5.2 List of exposure and development times for S1400-31 resist spun at 4000 rpm.

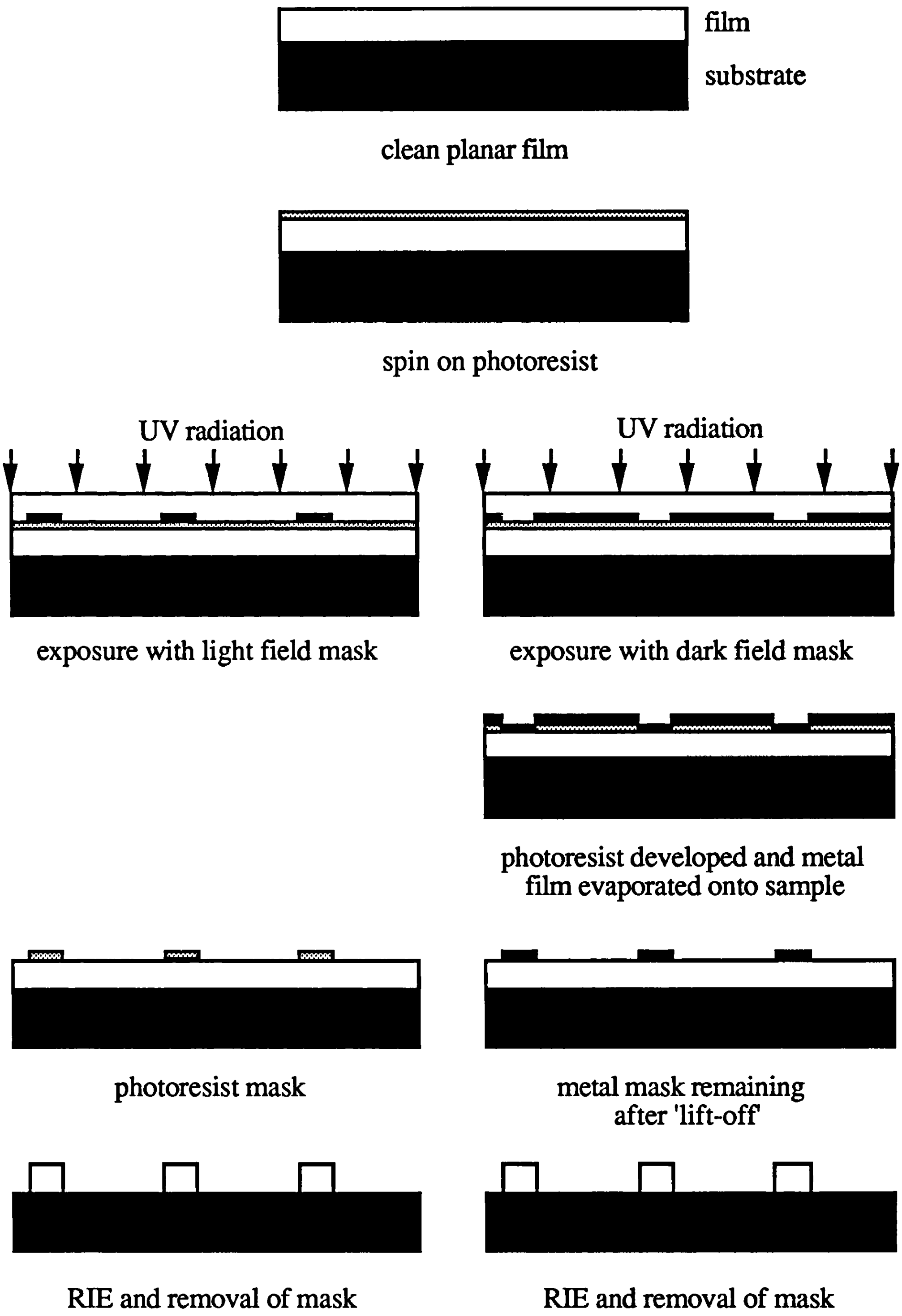

Figure 5.4 Schematic diagram of photolithographic process using positive photoresist with light and dark field masks to obtain ridge waveguides after RIE.

For planar waveguide laser structures, it is essential that the channel waveguides are normal to the polished end facets. To achieve this, rectangular samples, typically 5 cm long by 3 cm wide, were exposed using the contact printer. The mask was placed against two sides of a precision-made right-angle block. A slip gauge was placed on the mask, against the block and the long side of the sample was placed against the slip gauge. This procedure ensured that the long side of the sample was parallel to the pattern of straight waveguides on the mask to within an estimated few minutes of arc. Samples were then polished normal to this reference edge. A schematic diagram of the photolithographic arrangement is given below in figure 5.5.

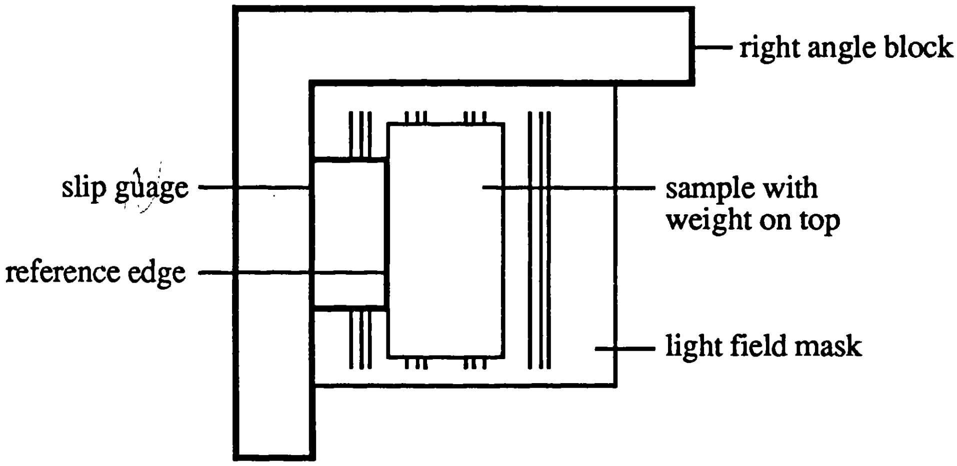

Figure 5.5 Schematic diagram of photolithographic arrangement to ensure that patterned photoresist of straight waveguides are parallel to reference edge of sample.

Alternatively, exposure was carried out using the full 3 inch diameter sample. After RIE and if required cladding of the ridge waveguides with SiO_2-B_2O_3-P_2O_5 glass, the sample was cut using a diamond resin bonded blade, the alignment of the cut checked using a video camera and monitor system.

5.3.2 Reactive Ion Etching

RIE involves the inducement of a molecular glow discharge in a reactive gas with Radio Frequency (RF) power (typically 13.6 MHz) between two planar parallel electrodes. Partial rectification of the rf power takes place due to ions moving more slowly than electrons and a dc voltage builds up across the electrodes, with a dark space existing above the cathode. The sample to be etched is placed on the cathode and is subjected to chemical and physical etch mechanisms by free radicals and energetic positive ion bombardment. The chemistry of the reactive gas is chosen such that the product molecule is volatile and may be removed without redeposition. Suitable gases used to etch silica include CF_4 [6], CHF_3 [7] and C_2F_6 [8].

The factors which need to be taken into consideration when making the choice of the etching process for a particular material are:

- Film etch rate and reproducibility.
- Material selectivity between mask and substrate.
- Etching anisotropy.
- Damage to sidewalls.

To obtain the desired etch depth, a well quantified process with reproducible etch rates is required. It is also necessary to ensure that the etch rate of the film is greater than that of the mask for accurate reproduction of the mask pattern. To minimise the propagation loss of the channel waveguides, the etched surface should also be smooth. For rare earth doped SiO_2-P_2O_5 films, there was an added complication in that the rare earth halides are non-volatile. Consequently, the redeposition of the non-volatile rare earth compounds resulted in micro-masking and additional surface roughness.

The etching process for silica is also dependent on the carbon/fluorine ratio of the etchant gas. For a low ratio, the etch rate is increased, but the material selectivity is reduced as photoresist masks are attacked more rapidly and a metal mask is required. The ratio may be lowered by adding O_2 to the plasma which also prevents the formation of organic polymers [9]. A high ratio presents good material selectivity and photoresist may be used as the mask material. However, there is a danger that there may be polymer formation, resulting in redeposition. Thus, the choice of etchant gas depends on several factors such as glass composition, mask material and redeposition.

Furthermore, the etch process is dependent on the etchant gas flow, pressure, power, chamber geometry, electrode material and substrate temperature. The behaviour of the system also depends on the preconditioning of the chamber in order to remove any polymeric impurities. Figure 5.6 shows schematically the Plasma Technology RIE80 machine used to etch the samples.

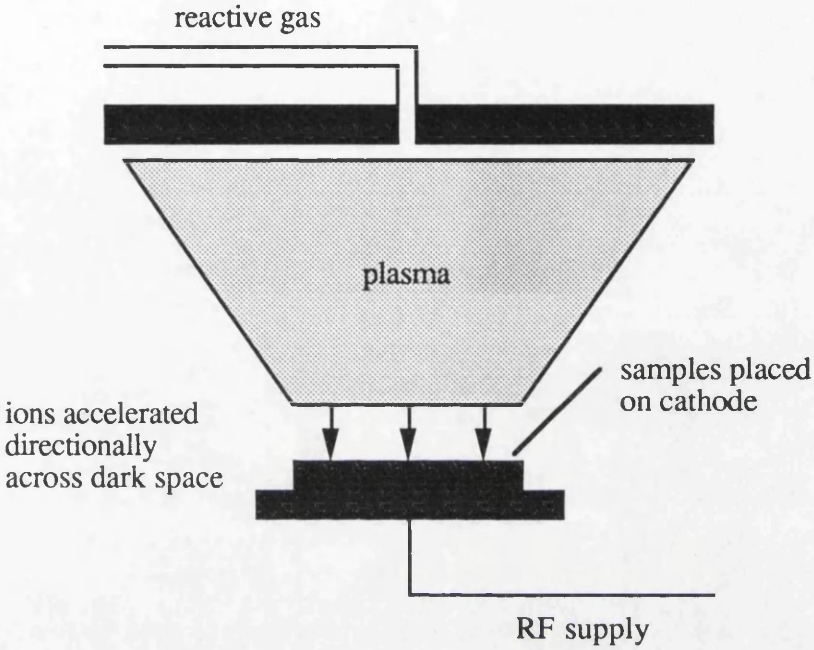

Figure 5.6 Schematic diagram of RIE chamber.

Three etching processes were analysed for their suitability for etching passive and rare earth doped SiO_2-P_2O_5 films. The processes examined were: a high pressure, high power C_2F_6 plus O_2 process; a low pressure, high DC bias CHF_3 process; and a C_2F_6 plus C_2H_4 process. The etch depth was determined by talystep measurements and the etch quality by SEM analysis.

5.3.2 C_2F_6 + O_2 Process

A high pressure, high power C_2F_6 plus O_2 process was investigated because of its high etch rate of silica, typically greater than 5 µm/hour and lack of polymer redeposition, due to the presence of O_2 [10]. A metal mask, consisting of 200 Å of titanium and 1500 Å of nickel, was used as the presence of O_2 in the etchant gas mixture would quickly remove a photoresist mask. The process parameters are summarised in table 5.3.

The etch rate for SiO_2-P_2O_5 glass was 6 µm/hour for the given parameters, which could be increased further by increasing the etchant gas pressure. The sidewalls of the etched ridge waveguide were smooth, as shown by figure 5.7, but the walls deviated further from the vertical with increasing etchant gas pressure.

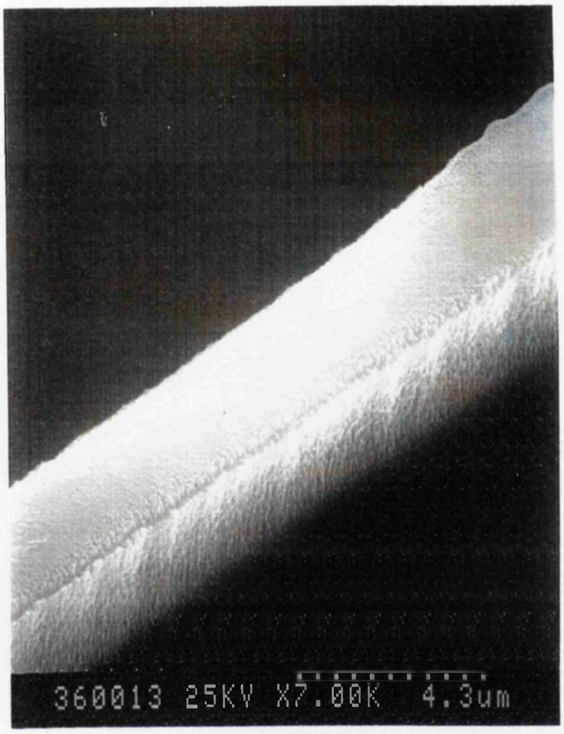

Figure 5.7 SEM of RIE of SiO_2-P_2O_5 film using C_2F_6 plus O_2 process.

However, the process was found to be unsuitable for etching rare earth doped SiO_2-P_2O_5 films. The etch rate collapsed from 6 µm/hour for passive films to 2 µm/hour for rare earth doped samples, due to the non-volatile nature of and subsequent redeposition of rare earth compounds forming a mask on the sample. The high etchant gas pressure was the apparent cause for the exacerbated redeposition, resulting in severe micromasking and surface roughness as shown in the SEM. The surface roughness formed by the redeposition produced ridge waveguides with high propagation losses.

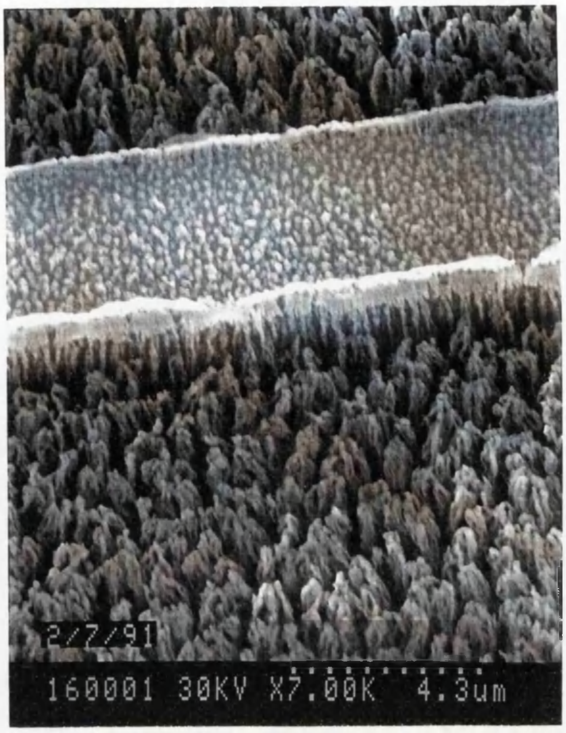

Figure 5.8 SEM of RIE rare earth doped SiO_2-P_2O_5 film using C_2F_6 plus O_2 process.

5.3.2 CHF_3 Process

A low pressure, high DC bias etching process was therefore investigated to minimise the redeposition of the non-volatile rare earth compounds, as the etching mechanism would be of a more physical nature due to energetic ion bombardment removing the surface atoms of the sample by sputtering. The process chosen was a low pressure, high DC bias CHF_3 process, giving an etch rate of 1.8 μm/hour for SiO_2-P_2O_5 films, which was maintained for rare earth doped SiO_2-P_2O_5 films. In addition, the surface roughness produced by the non-volatile rare earth products was much reduced when compared to the high pressure C_2F_6 plus O_2 process. SEM photographs of passive and rare earth doped channel waveguides etched using the CHF_3 process are given below in figures 5.9 and 5.10 respectively. With the added advantage of being able to use a photoresist mask, the CHF_3 process was the process chosen to etch the rare earth doped silica channel waveguides.

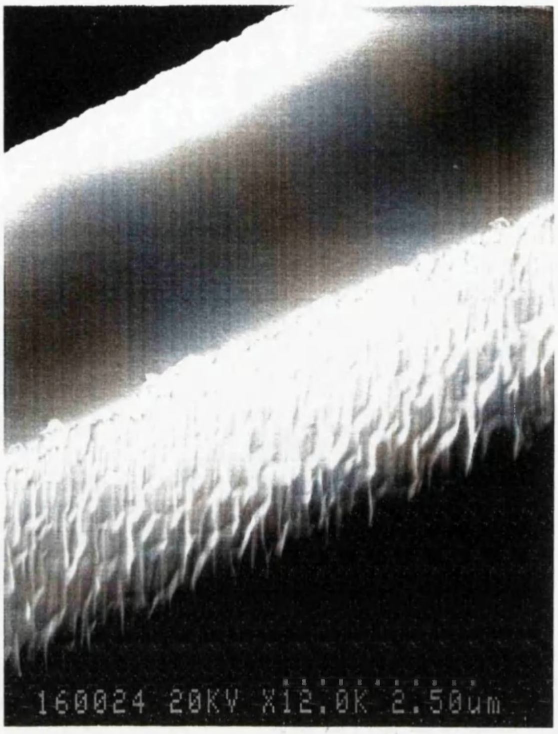

Figure 5.9 SEM of SiO_2-P_2O_5 film etched using CHF_3 process.

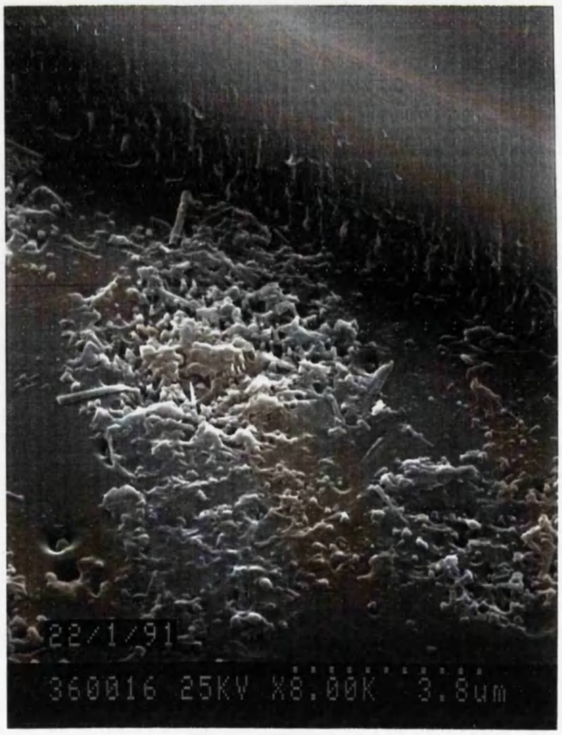

Figure 5.10 SEM of rare earth doped SiO_2-P_2O_5 film using the CHF_3 process.

However, as shown in figure 5.11, when the rare earth concentration was increased to greater than 1 wt%, the quality of the etching process deteriorated. The SEM shows significant redeposition and an increase in surface roughness, which would result in higher scattering losses of the resulting waveguides.

Figure 5.11 SEM of channel waveguide and surface roughness produced by etching SiO_2-P_2O_5 with a doping level of 1 wt% Er^{3+} using the low pressure CHF_3 process.

A disadvantage of the CHF_3 process was polymer redeposition. To reduce the possibility of formation of such impurities, the etch was stopped after one hour, the samples removed and chamber cleaned by a low pressure O_2 process for 30 minutes. Combined with the slow etch rate of 1.8 µm/hour and the pump down time of approximately 15 minutes to evacuate the chamber prior to etching, two days were required to etch 8 µm.

5.3.2 C_2F_6 + C_2H_4 Process

A third process was investigated which used a C_2F_6+C_2H_4 etchant gas mixture [11]. Using the etch conditions summarised in table 5.3, an etch rate of 4 µm/hour was obtained for SiO_2-P_2O_5 glass, with smooth, vertical sidewalls. But due to the success of the low pressure CHF_3 process, a complete investigation of the etching quality using this process for rare earth doped samples was not carried out.

A summary of the etch conditions used for the three processes and the main results from this investigation are presented below in table 5.3.

Etchant gas	CHF_3	C_2F_6+O_2	C_2F_6+C_2H_4
Etch rate SiO_2-P_2O_5 (µm/hour)	1.8	6	4
Etch quality for SiO_2-P_2O_5	very good	very good	very good
Etch rate Nd/Er: SiO_2-P_2O_5 (µm/hour)	1.8	2	-
Etch quality for Nd/Er: SiO_2-P_2O_5	good	poor	-
Polymer redeposition	yes	no	no
Mask material	photoresist	Ti/Ni	photoresist
Gas flow rate (sccm)	8	24/15	15/3
Pressure (mTorr)	8	100	20
DC bias (v)	510	320	360
Power (W)	100	200	200
Electrode material	graphite	graphite	graphite
Substrate temperature	21°C	21°C	21°C

Table 5.3 List of RIE parameters for three different RIE processes investigated.

5.3.3 Annealing Process

As discussed, the roughness of the etched sidewalls of the ridge waveguides strongly affects the propagation losses. To minimise such defects, an annealing process was developed to produce smooth sidewalls after the etching.

The optimum annealing condition for SiO_2-P_2O_5 channel waveguides with a index difference of 0.8 % with respect to the substrate, was found empirically to be 1000°C for 30 minutes. The results of the reflow process for SiO_2-P_2O_5 and rare earth doped samples are presented in figures 5.12 and 5.13 respectively. If the reflow process was carried out at too high a temperature, for example at 1100°C for 30 minutes, as shown in figure 5.14, due to the low softening temperature of the glass, the channel waveguides deformed. No reduction in the surface roughness was noted when the channel waveguides were annealed at the lower temperature of 300°C, indicating that the roughness was not due to polymer redeposition.

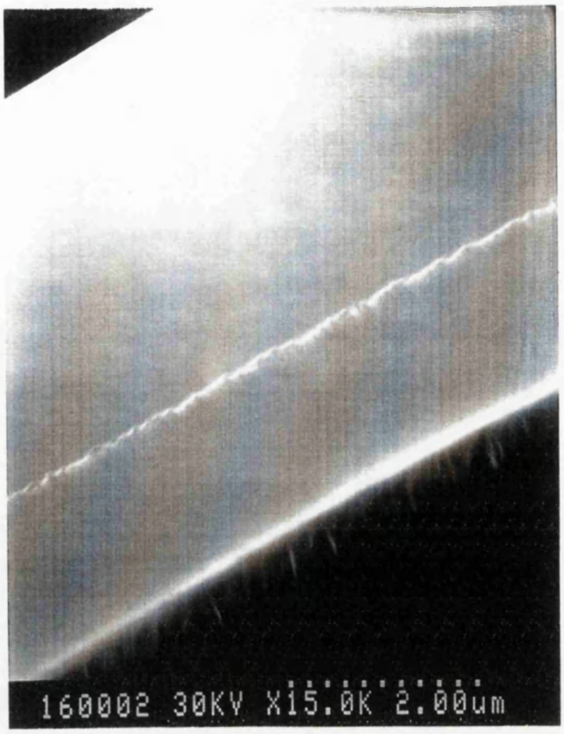

Figure 5.12 SEM of SiO_2-P_2O_5 channel waveguide reflowed at 1000°C for 30 minutes.

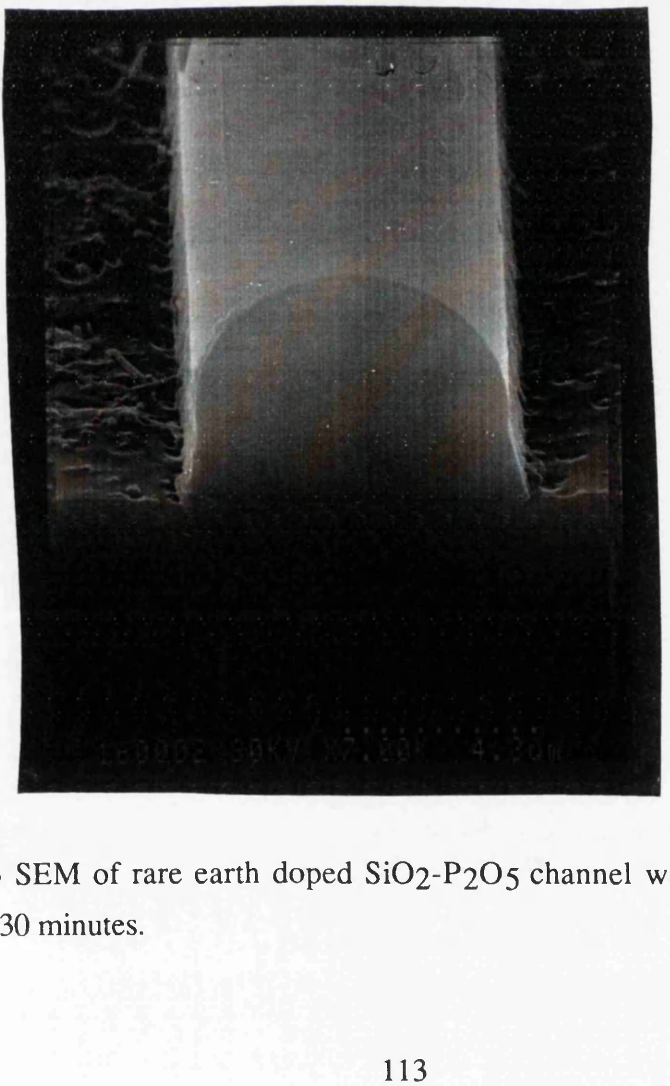

Figure 5.13 SEM of rare earth doped SiO_2-P_2O_5 channel waveguide reflowed at 1000°C for 30 minutes.

Figure 5.14 SEM of SiO_2-P_2O_5 channel waveguides reflowed at 1100°C for 30 minutes indicating vast deformation of channel waveguides.

5.3.4 Polishing Process

To enable efficient end fire coupling of light into the channel waveguides it is important to have the end faces polished. Furthermore, it was essential to have the channel waveguides polished normal to the end faces for the formation of Fabry-Perot type laser cavities, as angled waveguides would result in a reduction in reflectivity from mirrors placed against the end polished face [12]. To achieve this, samples were bound to a carrier rod with shellac resin, as illustrated in figure 5.15. The reference edge of the sample to which the channel waveguides were parallel, was placed against the edge of the carrier rod and the holder was set up level with the conditioning ring of the Logitech polishing jig, such that the final polished end face was perpendicular to the reference edge. Following such a procedure, the angle which the waveguides made to the polished end face was measured to be less than 0.25°.

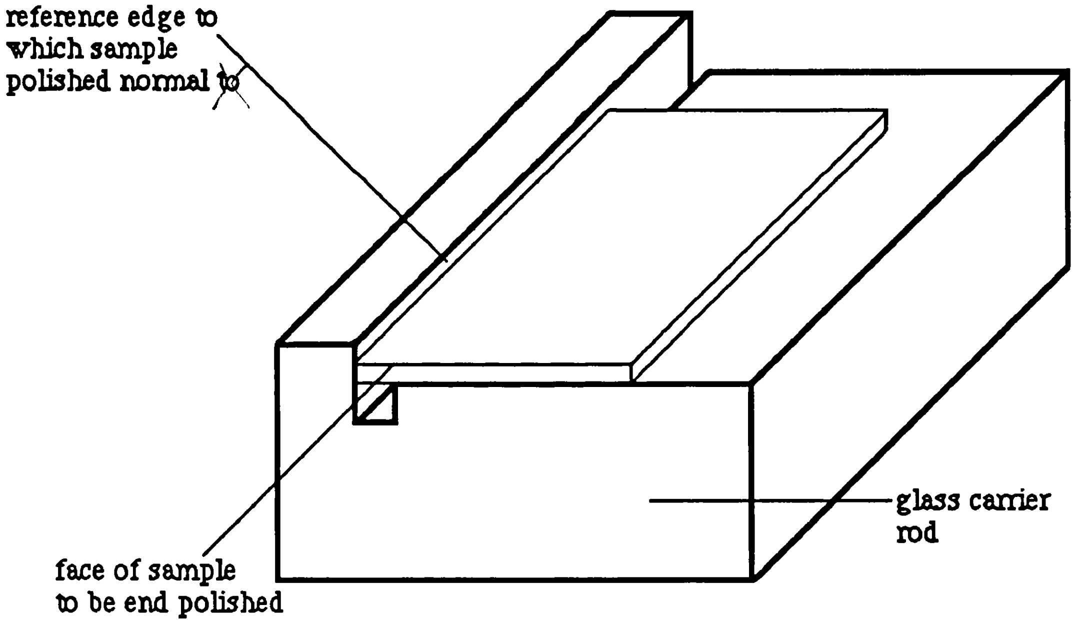

Figure 5.15 Schematic diagram of glass carrier rod used for polishing of samples.

The polishing process consisted of three different stages. The first stage involved a 'rough-down' on a cast-iron plate with silicon carbide powder suspended in water. This was followed by a semi-polish on a brass plate with a solution of aluminium oxide. The final stage to give the polishing a sharp edge used Syton W15, colloidal silica suspended in an alkali solution.

5.4 Optical Properties of Rare Earth Doped Silica Channel Waveguides

Fluorescence spectra, absorption spectra, fluorescence lifetimes and propagation losses were measured for rare earth doped silica channel waveguides. Characterisation of both Nd^{3+} and Er^{3+} doped SiO$_2$-P$_2$O$_5$ waveguides, fabricated by both the solution and aerosol doping techniques was carried out. The 6 µm thick films were fabricated using flow rates of 150 sccm SiCl$_4$ and 120 to 160 sccm PCl$_3$, with rare earth doping levels ranging from 0.1 wt% to 0.8 wt%. Films fabricated with PCl$_3$ flow rates below 120 sccm exhibited propagation losses too high for optical characterisation.

5.4.1 Fluorescence Spectra

Fluorescence spectra were obtained by 'end-fire' launching into 25 µm wide channel waveguides, the 514 nm output from an argon ion laser, the spectra recorded using an Advantest Spectrum Analyser.

The fluorescence spectra for Nd^{3+} doped SiO$_2$-P$_2$O$_5$ fabricated by the solution doping technique from the metastable $^4F_{3/2}$ to the $^4I_{9/2}$, $^4I_{11/2}$ and $^4I_{13/2}$ energy levels are presented in figures 5.16 - 5.18 respectively.

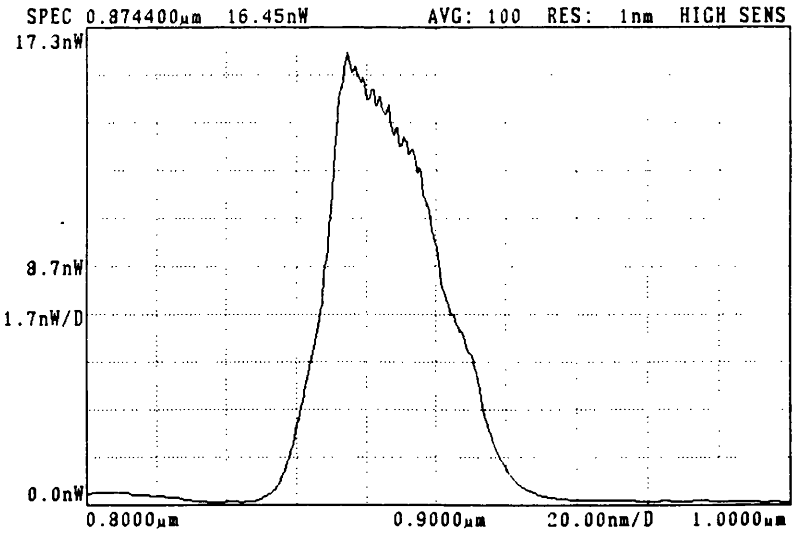

Figure 5.16 Fluorescence spectra of the Nd^{3+} $^4F_{3/2}$- $^4I_{9/2}$ transition.

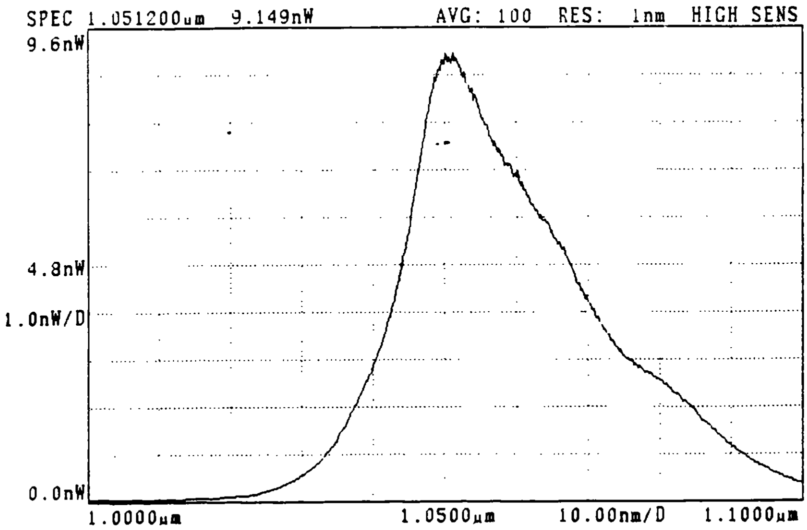

Figure 5.17 Fluorescence spectra of the Nd^{3+} $^4F_{3/2}$- $^4I_{11/2}$ transition.

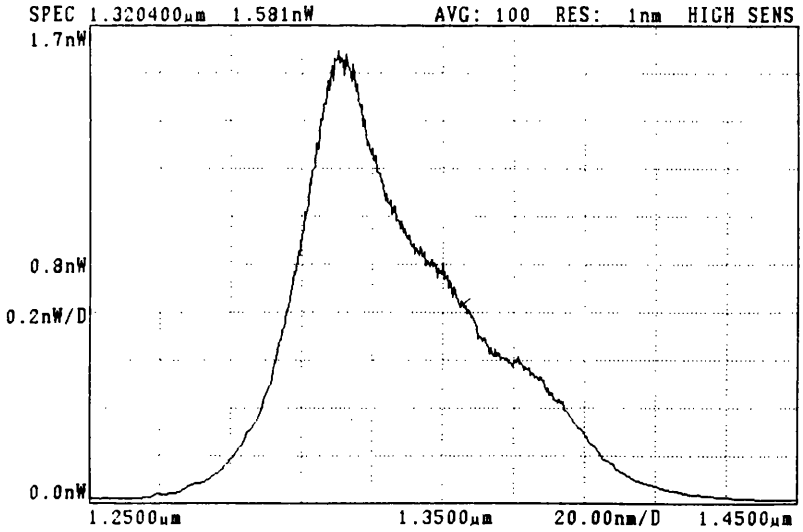

Figure 5.18 Fluorescence spectra of the Nd^{3+} $^4F_{3/2}$- $^4I_{13/2}$ transition.

Due to the high P_2O_5 codopant concentration, the emission peak for the three transitions were moved to shorter wavelengths than compared to Nd^{3+} doped pure silica. The emission peak wavelengths for the transitions $^4F_{3/2}$- $^4I_{13/2}$, $^4F_{3/2}$- $^4I_{13/2}$ and $^4F_{3/2}$- $^4I_{13/2}$ were 1.32 µm, 1.051 µm and 0.880 µm respectively. For Nd^{3+} doping levels ranging from 0.1 wt% to 0.6 wt% and for films fabricated with flow rates of 120 sccm and 160 sccm PCl_3, there was no change in the spectra for the three transitions. In addition, there was no difference in fluorescence spectra between samples fabricated by aerosol and solution doping techniques. Figure 5.19 gives the fluorescence spectra of the $^4F_{3/2}$- $^4I_{11/2}$ transition for a sample doped using the aerosol technique, with a doping level of 0.3 wt%.

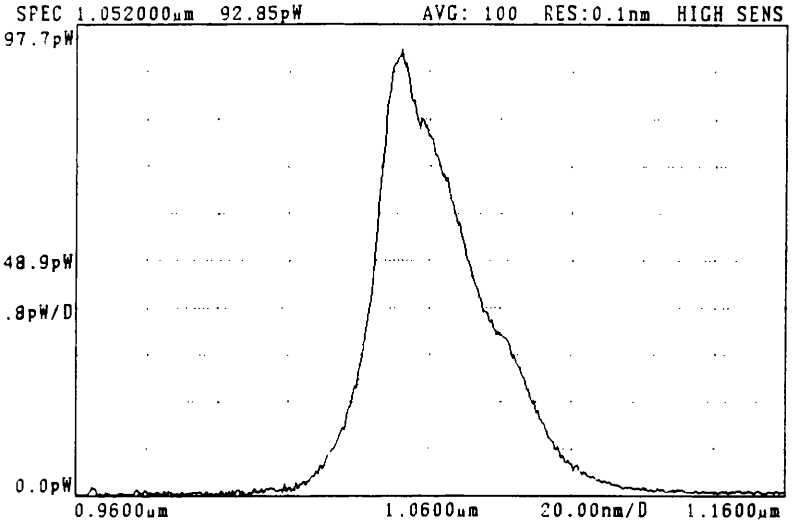

Figure 5.19 Fluorescence spectra of the Nd^{3+} $^4F_{3/2}$- $^4I_{13/2}$ transition for sample fabricated using aerosol doping technique.

The fluorescence spectra for the Er^{3+} doped SiO_2-P_2O_5 waveguide fabricated by the aerosol and solution doping techniques are given in figures 5.20 and 5.21. The emission peak and the full width half maximum for both spectra were 1.535 µm and 20 nm respectively. The difference in spectra compared to Er^{3+} doped pure silica, which has two emission peaks, the stronger at 1.535 µm and the weaker at 1.552 µm, is again due to the P_2O_5 codopant [13].

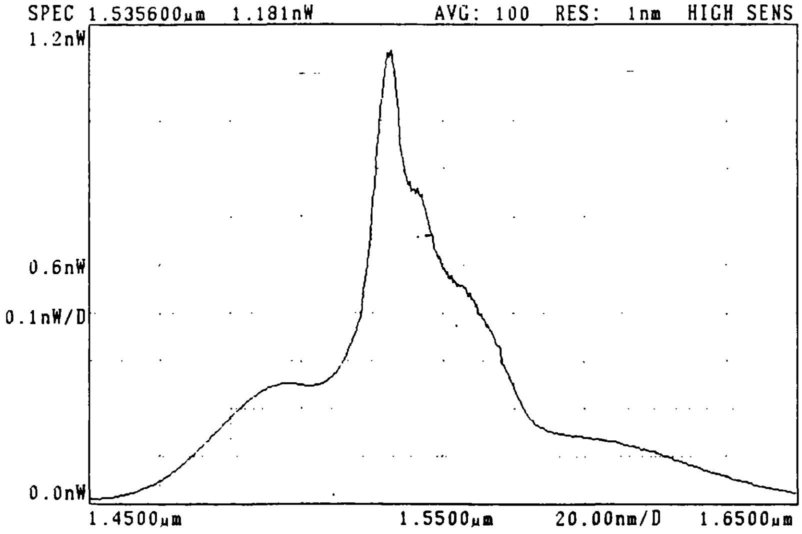

Figure 5.20 Fluorescence spectra of the Er^{3+} $^4I_{13/2}$- $^4I_{15/2}$ transition for sample fabricated using aerosol doping technique.

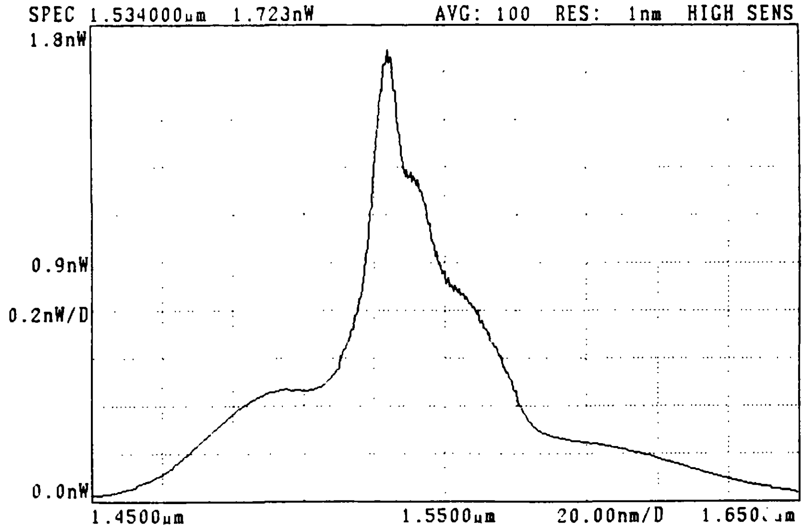

Figure 5.21 Fluorescence spectra of the Er^{3+} $^4I_{13/2}$- $^4I_{15/2}$ transition for sample fabricated using solution doping technique.

5.4.2 Absorption Spectra

Absorption spectra are of great importance as they give an indication of the doping level of the rare earth incorporated in the glass and the wavelength at which the rare earth dopant has peak absorption. These parameters are required when optimising the optical pumping efficiency of a device.

Nd^{3+} and Er^{3+} have many absorption bands, but for a compact, cost effective device, semiconductor diode pumping is desirable. As a result, absorption spectra measured have concentrated on absorption bands in the infra red where high power semiconductor sources are available. Absorption measurements were carried out on 25 μm wide channel waveguides using a halogen lamp as a white light source, 'end-fire' equipment and an Advantest Spectrum Analyser.

An estimation of the rare earth concentration in the silica glass was made by measuring the transmission spectra of the channel waveguides. The dopant levels were calculated by measuring the absorption peaks at 0.804 μm for Nd^{3+} and at 1.535 μm for Er^{3+} as shown in figures 5.22 and 5.23 respectively. Using the absorption coefficients of 5 $dBcm^{-1}wt\%^{-1}$ for the Nd^{3+} $^4I_{9/2}$- $^4F_{5/2}$ transition and 2.2 $dBcm^{-1}wt\%^{-1}$ for the Er^{3+} $^4I_{15/2}$- $^4I_{13/2}$ transition [14], it was found that for a given flow rate of carrier gas which was used to nebulise the aqueous rare earth chloride solution, the rare earth dopant level in the silica glass was proportional to the concentration of the nebulised solution as indicated in table 5.4. The rare earth doping levels achieved using the solution doping technique for samples partially sintered at 960°C for 30 minutes prior to immersion in absolute alcohol solutions are given in table 5.5.

Aerosol doping Technique

N_2 Flow rate	Solution strength (molar)	Doping level (wt%)
2.8 l/min	0.1	0.15
	0.2	0.30
	0.4	0.55

Table 5.4 Rare earth doping level in SiO_2-P_2O_5 glass as function of nebulised solution strength for constant flow rate of carrier gas.

Immersion time	Solution strength (molar)	Doping level (wt%)
15 min	0.01	0.2
	0.02	0.4
	0.04	0.6

Table 5.5 Rare earth doping level in SiO_2-P_2O_5 glass as function of solution strength for constant immersion time.

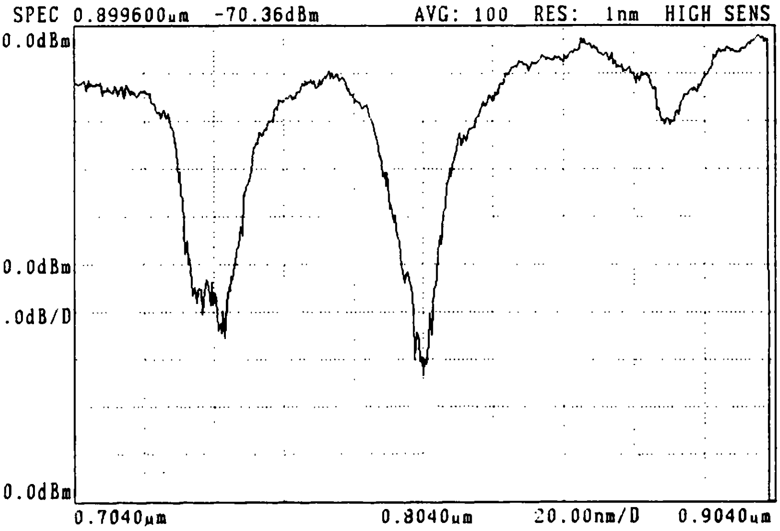

Figure 5.22 Absorption spectra of Nd^{3+} doped SiO_2-P_2O_5 fabricated by solution doping technique exhibiting $^4I_{9/2}$- $^4F_{7/2}$, $^4I_{9/2}$- $^4F_{5/2}$ and $^4I_{9/2}$- $^4F_{3/2}$ transitions.

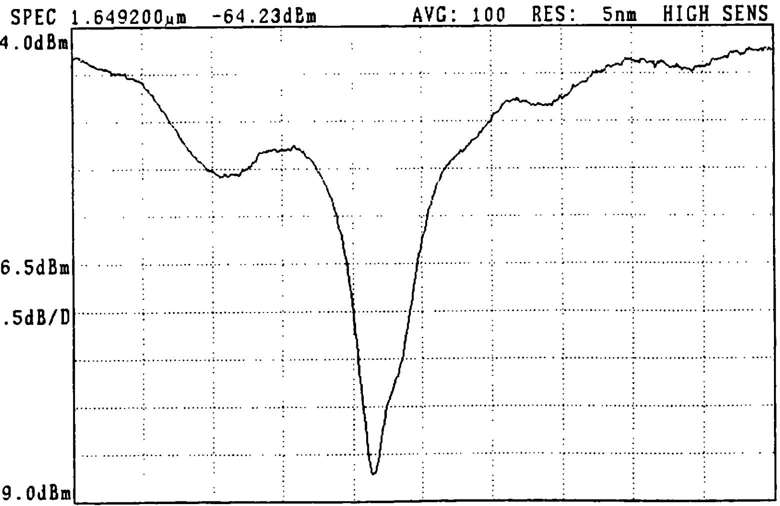

Figure 5.23 Absorption spectra of Er^{3+} doped SiO_2-P_2O_5 fabricated by solution doping technique exhibiting $^4I_{15/2}$- $^4I_{13/2}$ transition.

5.4.3 Fluorescence Lifetime Measurements

Lifetime measurements are an integral part of the optical assessment because they yield information concerning the solubility and doping uniformity of the rare earth in the host glass. As discussed in Chapter 2, fluorescence decay rates from the excited state provide knowledge about ion-ion interactions such as quenching processes and cooperative up-conversion, which influences the $^4I_{13/2}$- $^4I_{15/2}$ transition for Er^{3+}. These processes are detrimental to the performance of oscillators and amplifiers as they decrease the effective lifetime of the upper laser level and the quantum efficiency. The resonant transfer rate has a probability of occurrence which is inversely proportional to the inter- atomic distance raised to the sixth power and hence are strongly influenced by the doping density [15].

Fluorescence lifetime measurements concentrated on Er^{3+} doped SiO_2-P_2O_5 samples fabricated by both the solution and aerosol doping techniques with different doping concentrations. Moreover, lifetimes were measured for samples with the same doping density, but which were fabricated with different sintering rates and the lifetime was compared for a sample before and after the reflow process.

The experimental set up used to measure the fluorescence lifetime, shown in figure 5.24, consisted of a mechanical chopped argon-ion laser beam operating at 488 nm, with powers ranging from 50 mW to 500 mW, 'end-fire' launched into a 25 μm wide channel waveguide. The pulse duration was approximately 100 μs. The 1.54 μm fluorescence was detected using a Ge photodetector, the residual pump light removed after suitable filtering. The experimental set-up gave a temporal resolution of approximately 0.5 ms.

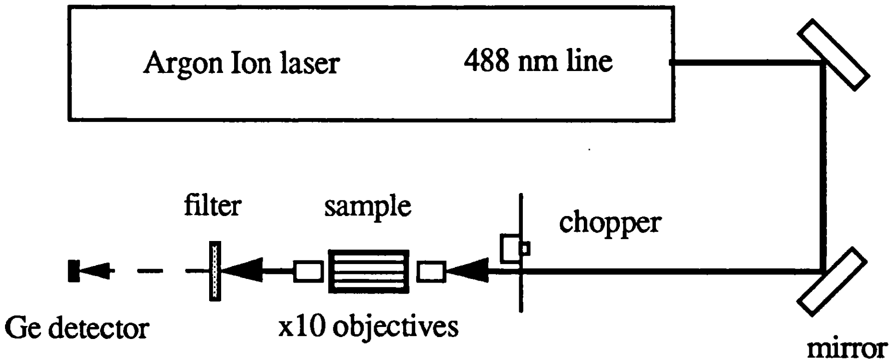

Figure 5.24 Experimental set-up utilised to measure fluorescence lifetimes.

The lifetime was determined using the above set-up by measuring the time taken for the signal to decay to the 1/e value of its peak value. Furthermore, there was the facility to examine the natural logarithm of the decay to view any departure from a single exponential decay.

Decay rates for samples fabricated by the aerosol doping technique were also measured by an experimental set-up at BT Laboratories. The excitation source in this case was an AlGaAs semiconductor laser diode operating near 0.8 μm, with the decay curves stored on a Tektronix 7854 digital storage oscilloscope. This system enabled examination of the decay curve itself, its natural logarithm and the differential of the natural logarithm. This facilitated analysis of the signal to determine any departure from exponentiality and the instantaneous decay rate at any time during the decay process.

Results for the measured fluorescence lifetimes are presented in tables 5.6 and 5.7.

Fabrication technique	Er doping level (wt%)	Δn (%)	Lifetime (ms)
solution doping	0.15	0.75	7
solution doping	0.6	0.75	7
solution doping	0.8	0.55	3
aerosol doping	~0.1	0.75	6.8
aerosol doping	~0.3	0.75	6.5
aerosol doping	~0.6	0.75	6.5

Table 5.6 Measured fluorescence lifetimes for Er^{3+} doped SiO_2-P_2O_5 samples fabricated by solution doping and aerosol doping techniques with different Er^{3+} doping levels. All samples were sintered at 1300°C for 2 hours.

Figures 5.25a and 5.25b show the natural logarithm and the differential of the natural logarithm of the decay for a sample fabricated by the aerosol doping technique with an Er^{3+} doping level of approximately 0.6 wt%. It is clearly evident that the decay was non-exponential, with the instantaneous fluorescence lifetime increasing with time. Figures 5.26a and 5.26b give the decay and the natural logarithm of the decay for a sample with an Er concentration of 0.6 wt% fabricated using the solution doping technique. Again it is evident from the natural logarithm curve that the decay deviates from exponentiality. Such behaviour was typical for all the samples investigated.

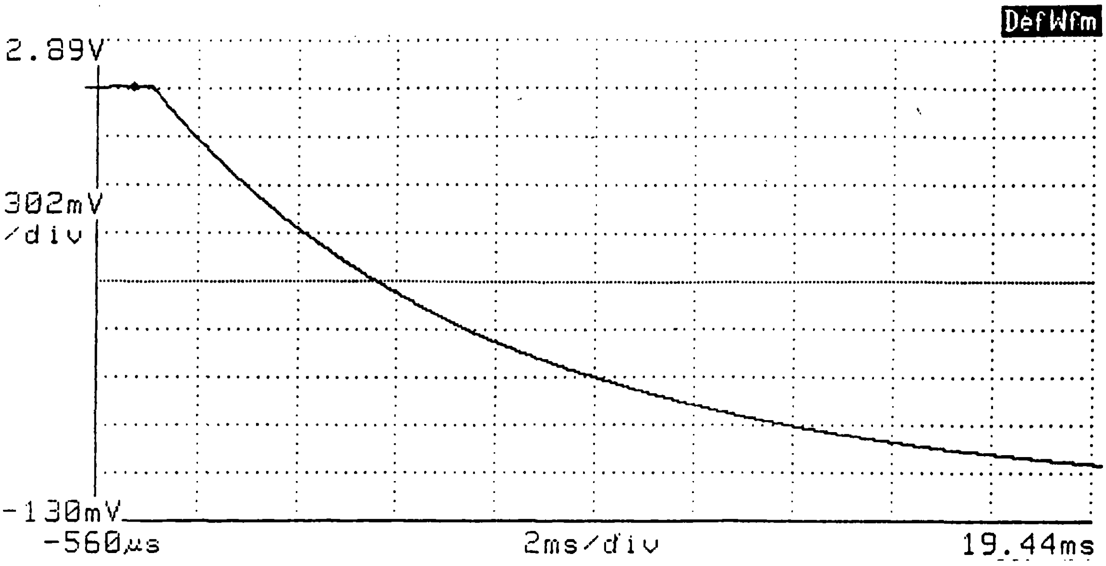

Figure 5.25a The natural logarithm of the fluorescence decay for 0.6 wt% Er^{3+} SiO_2-P_2O_5 fabricated by the aerosol doping technique.

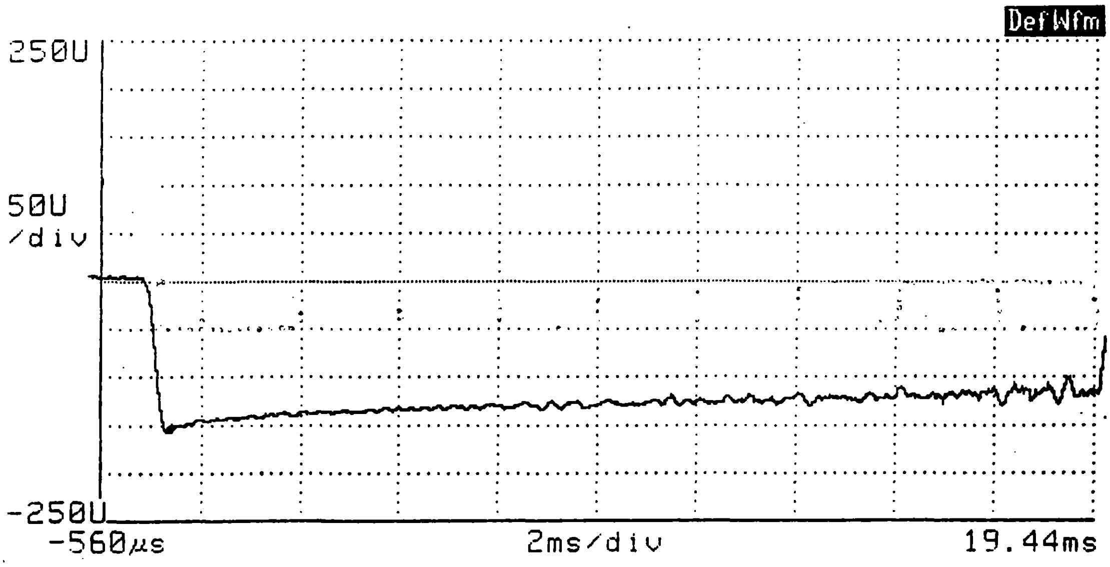

Figure 5.25b The differential of natural logarithm of the fluorescence decay for 0.6 wt% Er^{3+} doped SiO_2-P_2O_5 fabricated by the aerosol doping technique.

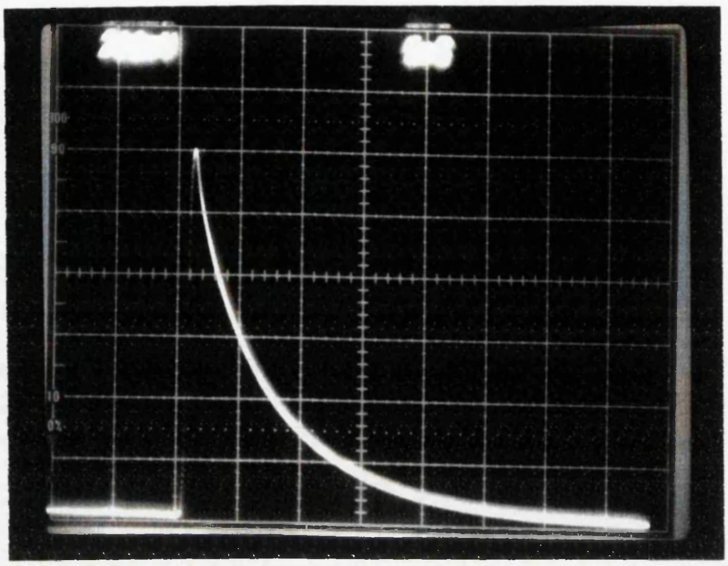

Figure 5.26a The fluorescence decay for 0.6 wt% Er^{3+} doped SiO_2-P_2O_5 fabricated by the solution doping technique.

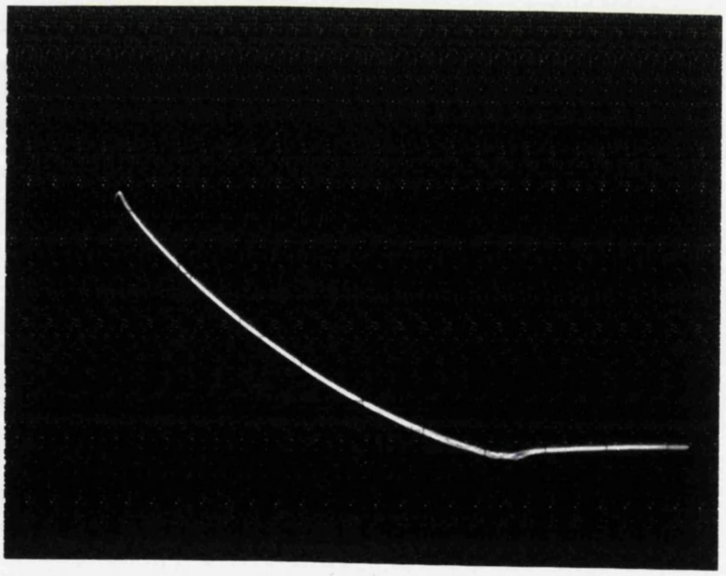

Figure 5.26b The natural logarithm of the fluorescence decay for 0.6 wt% Er^{3+} doped SiO_2-P_2O_5 fabricated by the solution doping technique.

The main conclusions that can be drawn from table 5.6 are:

1. There was no major difference in the measured fluorescence lifetime for samples fabricated by the aerosol or the solution doping technique.

2. The measured lifetime, approximately 7 ms, was relatively independent of the Er^{3+} doping concentration ranging from 0.1 to 0.6 wt%, with a P_2O_5 codoping level resulting in a relative index difference, Δn, between the guide and substrate of 0.75 %.

3. For a P_2O_5 codoping level giving a Δn of 0.55% and Er^{3+} doping level of 0.8 wt%, the lifetime was dramatically reduced to 3 ms, indicating greater dominance of non-radiative decay, due to greater clustering of the Er^{3+}.

4. The decay was non-exponential, with the decay rate decreasing as a function of increasing time.

5. The measured fluorescence lifetimes were independent of excitation power, ranging from 50 to 500 mW ($\lambda = 488$ nm) and pump wavelength.

In assessments of Er^{3+} doped silica fibres, with concentrations below 0.1 wt%, the decay was found to be a smooth exponential and had an equivalent lifetime of ~10 ms. However, the decay behaviour of fibres with an Er^{3+} concentration of 2.3 wt% was non-exponential with high excitation power levels of ~100 mW, the decay rate decreasing late in the decay process, also decreasing with excitation power levels reduced to approximately 1 mW. The observed increased decay rates and non-exponential decay were attributed to the up-conversion mechanism [15]. This behaviour is similar to that noted for the Er^{3+} doped SiO_2-P_2O_5 planar waveguides and hence the decay characteristics may be due to the co-operative upconversion mechanism, indicating non-uniform distribution of the Er^{3+} in the glass host. Non-uniform distribution of Nd^{3+} in planar SiO_2-P_2O_5 films has also been observed [16], with a measured lifetime of 250 μs, as compared to 500 μs for Nd^{3+} doped silica where no clustering is evident.

Table 5.7 presents the results of the dependence of the fluorescence lifetime on the fabrication process of Er^{3+} doped SiO_2-P_2O_5 planar waveguides. Two samples doped with ~0.3 wt% Er^{3+} using the aerosol doping technique were consolidated at different rates: one sample was placed in the furnace at 1300°C and held there for 2 hours; the second sample was placed in the furnace at 800°C, ramped up to 1300°C at 5°C/minute and held there for 2 hours. The 1/e point for both samples was measured to be ~7 ms, but as illustrated in figure 5.27, there was evidence of a rapid decay component at the start of the decay of the sample which was consolidated with the ramped sintering process. No change in the 1/e point was found for the sample which had been reflowed at 1000°C for 30 minutes, which had been previously sintered at 1300°C for 2 hours.

Sintering process	Er doping level (wt%)	Δn (%)	Lifetime (ms)
1300°C for 2 hrs	~0.3	0.75	7
800°C to 1300°C 5°C /min 1300°C for 2hrs	~0.3	0.75	7
1300°C for 2 hrs Reflow process 1000°C for 30 min	~0.3	0.75	7

Table 5.7 Measured fluorescence lifetimes for Er^{3+} doped SiO_2-P_2O_5 samples fabricated by the aerosol doping technique and consolidated with different sintering rates and comparison of lifetime before and after reflow process.

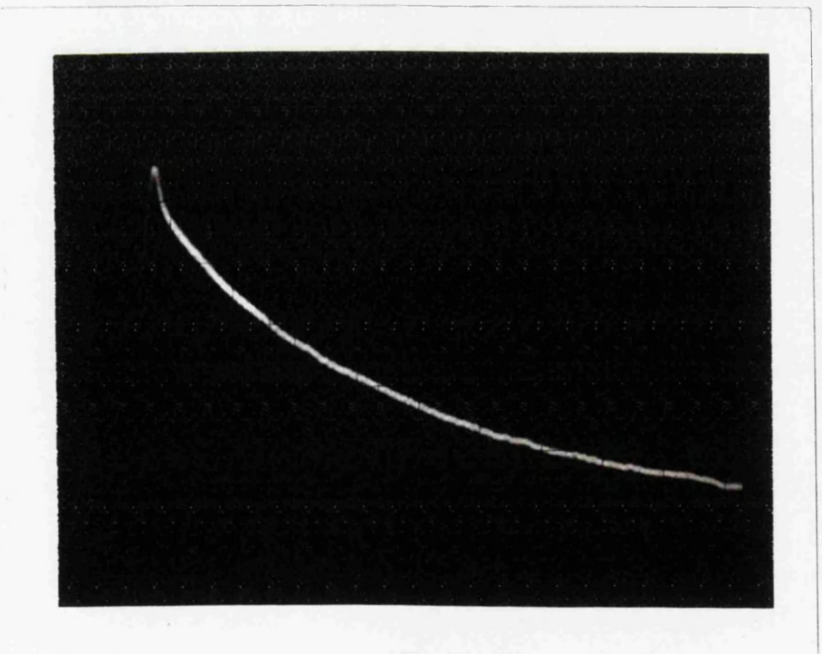

Figure 5.27 The fluorescence decay for 0.3 wt% Er^{3+} SiO_2-P_2O_5 sintered using the ramp process.

5.4.4 Channel Waveguide Loss Measurements

The formation of low loss rare earth doped SiO_2-P_2O_5 channel waveguides is of great importance as the available optical gain from the rare earth dopant must be greater than the background loss to form useful devices. Moreover, the lower the loss, the lower the required pump power for threshold and the greater the slope efficiency for lasers and the greater the pump efficiency and signal gain for amplifiers.

The loss of the channel waveguides formed by RIE is generally greater than the loss for planar waveguides due to scattering losses arising from imperfections in the etched sidewalls of the ridge waveguide. These imperfections are due to roughness in the mask used to form the pattern for the channel waveguides and damage to the sidewalls during the etch process. The surface roughness produced is generally of the order of 0.1 μm. Furthermore, as discussed in section 5.3, the scattering loss is increased by the additional surface roughness produced when rare earth doped SiO_2-P_2O_5 glass is etched as compared to passive SiO_2-P_2O_5 glass due to the non-volatile nature of the rare earth products produced during the RIE process. In an attempt to reduce the scattering loss of the channel waveguides, as descibed previously, an annealing process was developed and the channel waveguides were clad with SiO_2-B_2O_3-P_2O_5 glass.

The cladding of the ridge waveguides was performed by G. D. Maxwell at BT Laboratories. The SiO_2-B_2O_3-P_2O_5 glass was formed by the FHD of 150 sccm $SiCl_4$, 50 BCl_3 and 15 sccm PCl_3. The deposited glass soot was consolidated at a reduced temperature to avoid vast deformation of the channel waveguides. The refractive index of the cladding layer was approximately equal to that of the substrate. The thickness of the clad was 15 to 20 μm.

The losses of the channel waveguides were measured by two techniques: the fibre probe technique used for samples with no glass cladding layer and a method entailing the butt-coupling of optical fibres to the channel waveguides and measuring the insertion loss. As shown in figure 5.28, the second method involved light from a fibre pig-tailed, temperature controlled laser diode emitting at 1.54 μm being fed into the device under test through single mode optical fibres. The power output from the laser diode was monitored using an optical coupler: one output port of the coupler leading to the device and the second port to a Ge detector, the measured power level acting as a reference value. The 1.54 μm light was fed into the channel waveguide under assesssment by butt-coupling the single mode optical fibre against the end-face of the substrate. To maximise the coupling of light into the channel waveguide, visible light at 632.8 nm from a He-Ne laser was first coupled into the optical fibre, enabling alignment of the fibre and the channel waveguide, aided by a microscope situated above the sample.

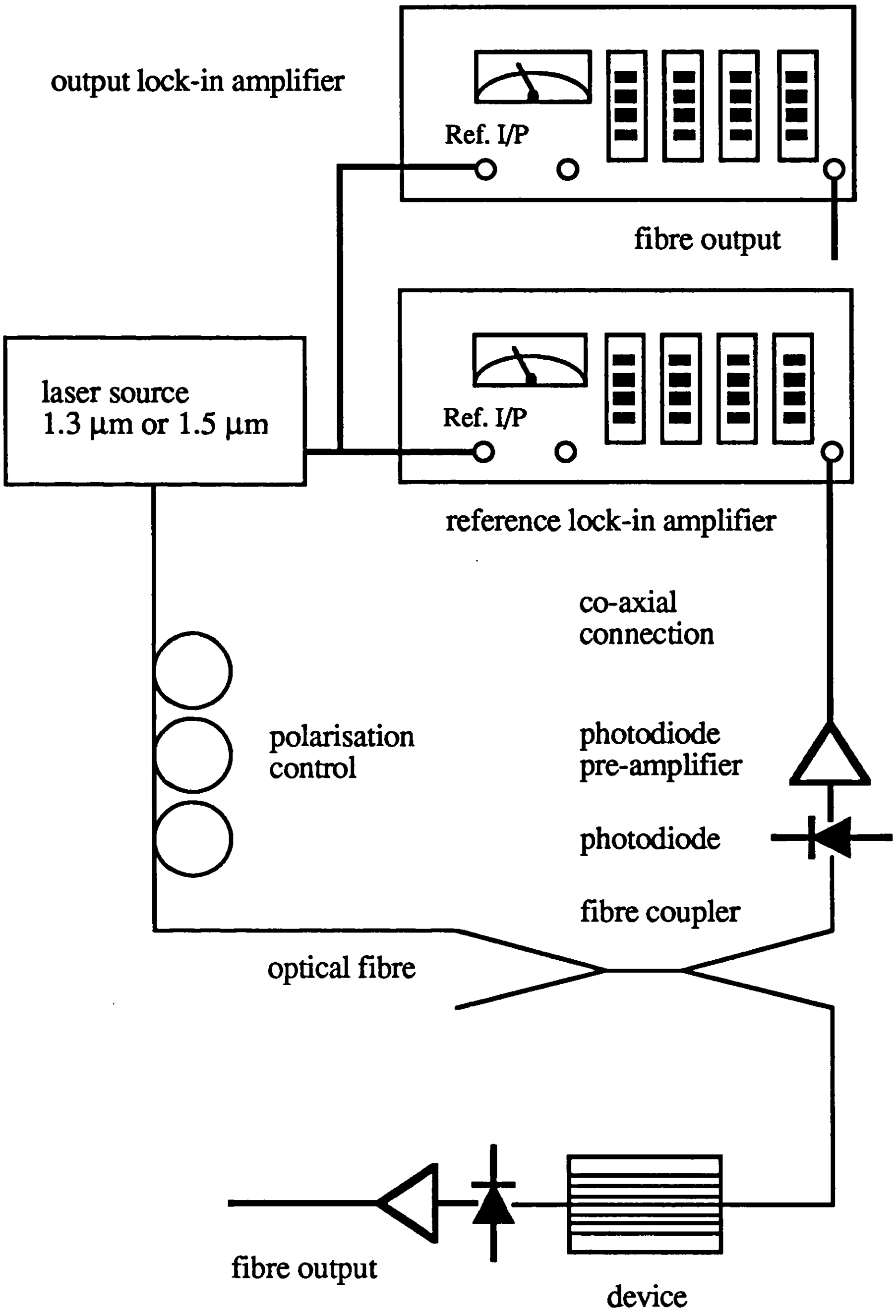

Figure 5.28 Schematic of experimental set-up used to measure ridge waveguide loss using the butt-coupling of optical fibres.

The light output from the channel waveguide was collected by a multimode optical fibre, the output from which was detected by a second Ge photodiode. After maximising the coupling efficiency the light source was then switched to the 1.54 μm diode laser. To obtain a high coupling efficiency of light into the channel waveguides, stages with differential and piezoelectric translational adjustment were used and index matching fluid was placed on the optical fibre face brought into close proximity with the channel waveguide. Lock-in techniques and photodiode pre-amplifers were also employed.

Figures 5.29 and 5.30 present the loss measurements for 0.4 wt% Nd^{3+} doped SiO_2-P_2O_5, 20 μm wide channel waveguides, measured at 632.8 nm using the fibre-probe technique, illustrating the effect of the annealing process on the loss of the channel waveguides. The channel waveguides formed by the low pressure, high DC bias CHF_3 process, which etched through the 6 μm thick core and 1.2 μm into the buffer layer, yielded a loss of 6.5 dB/cm. After the annealing process, the loss of the same waveguide was reduced to 2.5 dB/cm. The annealing process was therefore effective in reducing the loss of the channel waveguides.

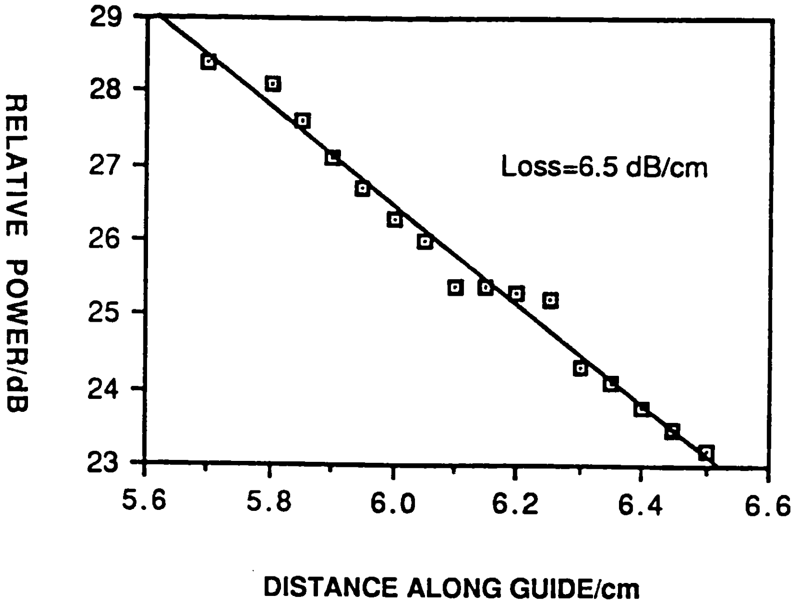

Figure 5.29 Loss measurement of 20 μm wide channel waveguide at 632.8 nm formed by CHF_3 process using fibre-probe technique before annealing process.

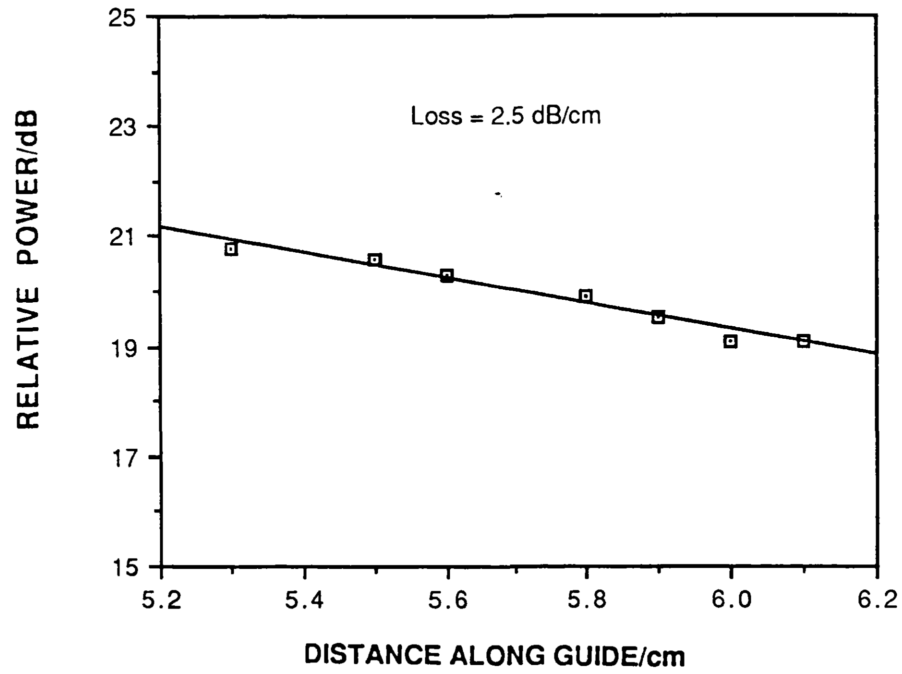

Figure 5.30 Loss measurement of 20 µm wide channel waveguide at 632.8 nm formed by CHF_3 process using fibre-probe technique after annealing process.

The loss measurements for annealed, cladded channel waveguides formed by the CHF_3 etch process for various widths and Nd^{3+} doping concentrations with an etch depth of 1.2 µm into the buffer layer is summarised below in table 5.8. The loss values were determined by butt-coupling optical fibres against the polished end-face of the channel waveguides in order to measure the insertion loss. This method gave an over-estimation of the loss of the channel waveguides by approximately 0.1 dB/cm as the input coupling loss was assumed to be negligible.

Nd^{3+} doping concentration(wt%)	Channel waveguide width (µm)	Insertion loss (dB)	Loss (dB/cm)
0.4	10	4.0	1.1
0.4	20	1.7	0.5
0.6	10	4.9	1.2
0.6	20	3.0	0.8

Table 5.8 Loss measurements of channel waveguides of various widths and Nd^{3+} doping concentrations at 1.54 µm using the optical fibre butt-coupling method.

As indicated in Table 5.8, the loss of channel waveguides with a width of 10 μm was greater than that for waveguides with a width of 20 μm. This was due to the greater exposure of the guided mode in the narrower waveguide to the wall roughness and surface roughness produced by the rare earth redeposition. Also, as expected, the loss of the channel waveguide with a 0.6 wt% Nd^{3+} doping level was greater than that of the waveguide with the lower Nd^{3+} doping level. Moreover, as the loss measurements were performed at 1.54 μm, it is anticipated that the loss of the waveguides at the emission wavelength of Nd^{3+} at 1.05 μm will be greater due to the scattering losses being wavelength dependent, increasing for decreasing wavelength.

In an attempt to reduce the loss of the channel waveguides further, the etch depth into the silica buffer layer, after etching through the core layer, was increased to 3 μm in order to increase the separation between the waveguide core and the rare earth redeposition, thus decreasing the exposure of the evanescent field to the surface roughness produced by such redeposition. The loss of cladded channel waveguides, 8 μm wide with the increased etch depth into the buffer layer, was found to be 0.5 dB/cm. Similarly, the loss of Nd^{3+} doped SiO_2-P_2O_5 channel waveguides fabricated by Maxwell at BT Laboratories using a high power C_2F_6 plus CHF_3 etch process with a 6 μm by 6 μm core cross-section was measured to be below 0.3 dB/cm.

5.4.5 Nd^{3+} doped SiO_2-P_2O_5 Planar Waveguide Lasers

The fabrication of the Nd^{3+} doped SiO_2-P_2O_5 channel waveguides by G. D. Maxwell at BT Laboratories and assistance with the optical assessment of the devices at Glasgow University by J. R. Bonar is gratefully acknowledged.

The 6 µm thick SiO_2-P_2O_5 films were formed using a recipe developed by the author involving the FHD of 150 sccm $SiCl_4$ and 200 sccm PCl_3 and partially sintered at 950°C for 10 minutes. Rare earth ions were incorporated into the porous structure using the solution doping technique. After immersion and drying, the films were consolidated at 1375°C for 2 hours and finally removed from the furnace without first ramping down the temperature. Channel waveguides were patterned using a 500 nm thick Ni and Ti mask and formed by a high power, high DC bias CHF_3 and C_2F_6 gas mixture process. The etch rate was approximately 9 µm/hour. The ridge waveguides were clad with a glass produced by the FHD of 150 sccm $SiCl_4$, 50 sccm BCl_3 and 15 sccm PCl_3 and sintered at a reduced temperature. The refractive index of the cladding layer was tailored to match that of the silica substrate. The core dimensions were 6 µm wide, 6 µm deep and 6 cm long and the substrate was cut normal to the guides.

The laser cavity was formed by pressing two dielectric coated 2 mm thick mirrors against the ends of the 1 mm thick substrate. Index matching fluid, with a refractive index of 1.45, was used to hold the mirrors in place. The input mirror used had a high reflectivity (R=99.9%) at the lasing wavelength and high transmission at the pumping wavelength (T=90%). The output coupler had a R=95% at the lasing wavelength and T=90% at the pumping wavelength. 804 nm radiation from an Ar ion pumped Ti: Al_2O_3 laser was end-fire coupled into the waveguides using a x10 microscope objective. The light output from the waveguide was collimated also using a x10 microscope objective, the residual pump light removed using a filter. The signal spectrum was measured using an Advantest Spectrum Analyser and the output power levels by a calibrated Ge detector. The experimental arrangement to achieve oscillation is illustrated in figure 5.31.

For a Nd^{3+} doping level of 0.4 wt%, the absorbed pump power threshold for cw oscillation was 25 mW. The incident pump power was 220 mW. The absorbed pump power was measured by tuning the Ti: Al_2O_3 laser to a wavelength at which there was no absorption and comparing the transmitted power to that of the transmitted power at 804 nm, the difference in power levels yielding the absorbed pump power. As shown in figure 5.32, using the 95 % reflectivity output coupler, the slope efficiency attained was approximately 3.3 %.

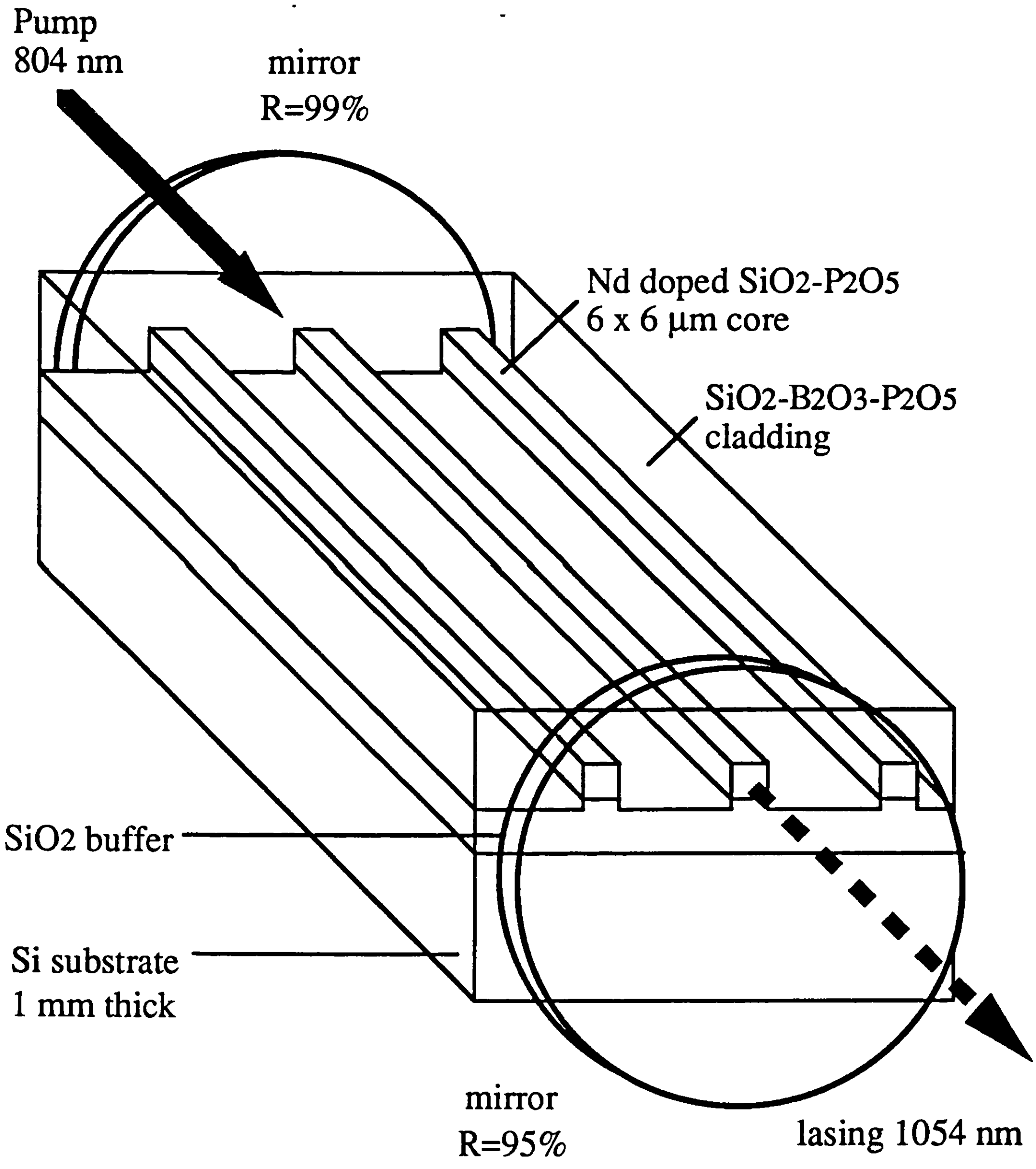

Figure 5.31 Schematic of experimental arrangement to achieve oscillation in Nd^{3+} doped SiO_2-P_2O_5 ridge waveguides.

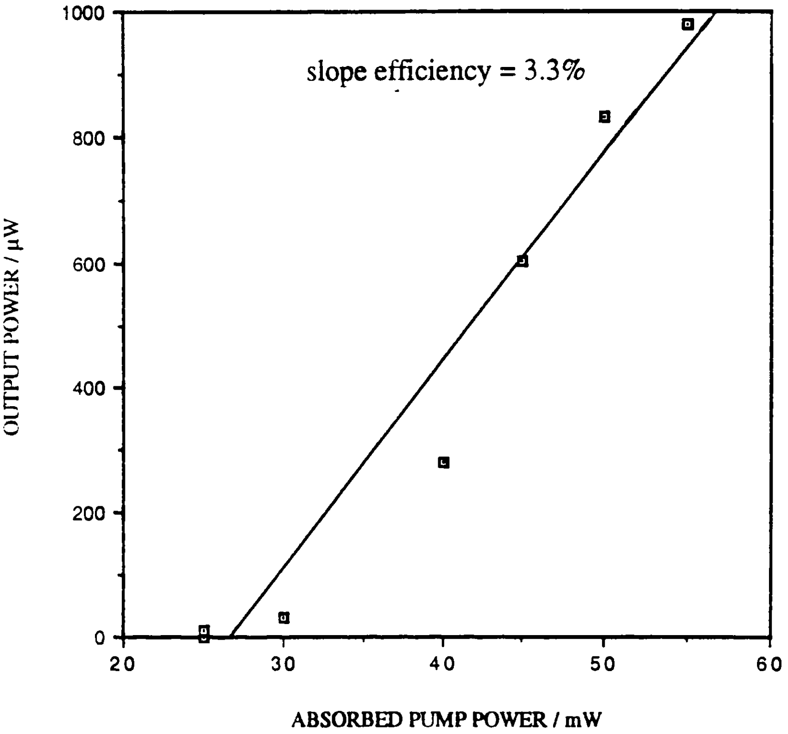

Figure 5.32 Output power at 1054 nm as a function of absorbed pump power at 804 nm.

The signal spectrum at threshold and for an absorbed pump power of 50 mW are given in figure 5.33 and 5.34, respectively. The peak lasing wavelength was 1.054 µm, with a FWHM of 1.7 nm. The subsidiary peaks present in figure 5.34 are probably due to the mirrors not being in hard contact with the ends of the substrate, thus forming a Fabry-Perot cavity between the face of the substrate and the mirror. The frequency separation of the modes indicates a 10 µm gap between the substrate face and mirror. CW oscillation was maintained for 5 hours with no deterioration in output power and without variation in peak lasing wavelength, indicating the lack of thermal conductivity problems.

Oscillation was also achieved with 0.5 wt% Nd^{3+} doping level. Incident pump power for cw oscillation in this case was 450 mW. The lasing spectrum for an incident pump power of 550 mW is illustrated below in figure 5.35. The peak lasing wavelength was again 1054 nm, with a FWHM of 2 nm. The maximum output power was greater than 2 mW and was limited by the maximum availble pump power set at 600 mW.

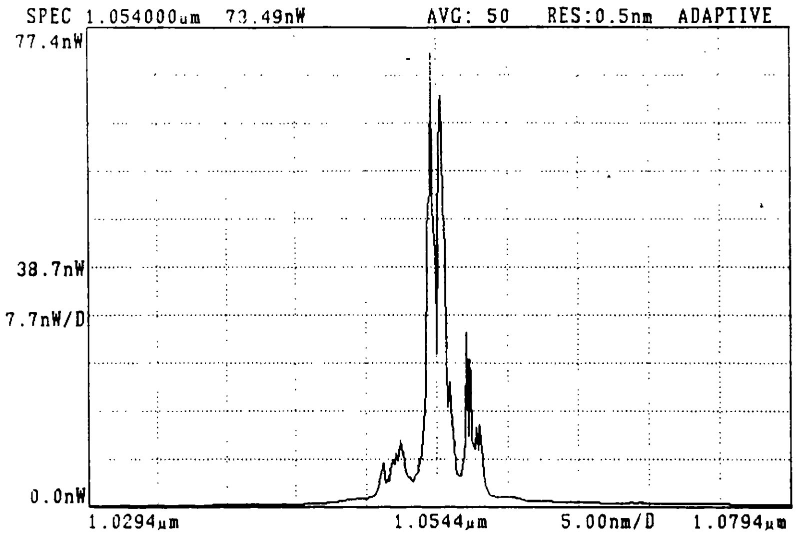

Figure 5.33 Lasing spectrum at threshold for 0.4 wt% Nd^{3+} doping level.

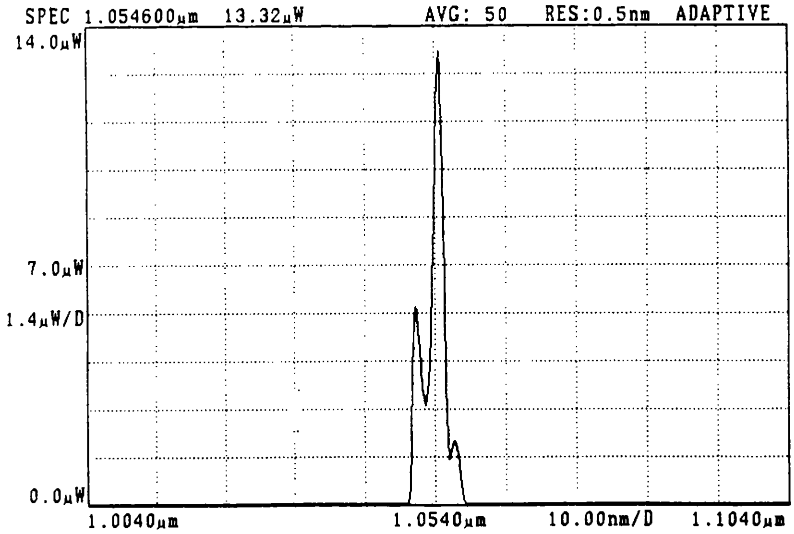

Figure 5.34 Lasing spectrum at 50 mW of absorbed pump power for 0.4 wt% Nd^{3+} doping level.

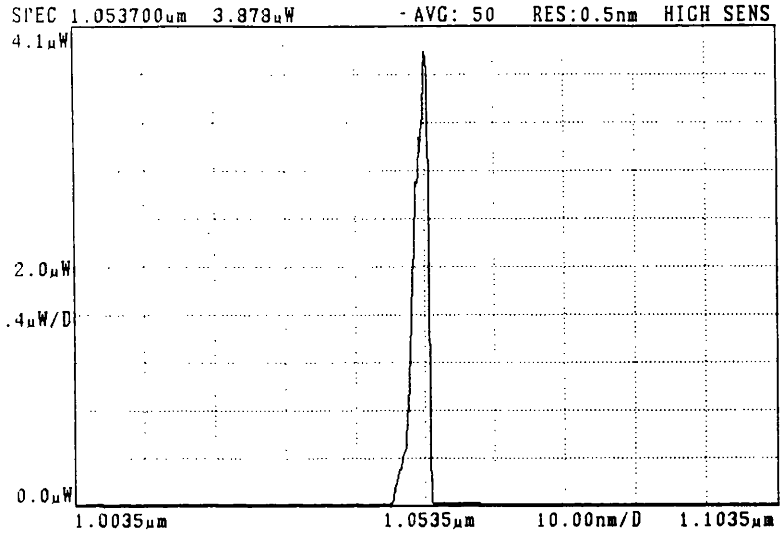

Figure 5.35 Lasing spectrum at 550 mW of incident pump power for 0.5 wt% Nd^{3+} doping level.

5.5 Conclusion

Channel waveguides were formed by a combination of photolithographic and RIE techniques. Three different RIE processes were investigated for producing high quality, low loss ridge waveguides: a low pressure, high DC bias CHF_3 process proving to be the most suitable to etch rare earth doped SiO_2-P_2O_5. A high power, high DC bias C_2F_6 and CHF_3 process used by Maxwell at BT Labs was also successful at producing low loss channel waveguides. Loss measurements were performed for channel waveguides with SiO_2-B_2O_3-P_2O_5 glass or air as the cladding layer, with losses measured to be below 0.3 dB/cm for waveguides with a 6 by 6 μm cross-section.

Fluorescence and absorption spectra were obtained for both Nd^{3+} and Er^{3+} doped SiO_2-P_2O_5 waveguides. Fluorescence lifetime measurements concentrated on Er^{3+} doped SiO_2-P_2O_5 samples fabricated by solution and aerosol doping techniques and were measured to be approximately 7 ms for both doping techniques, with doping concentrations ranging from 0.1 to 0.6 wt%. Finally, Nd^{3+} doped SiO_2-P_2O_5 planar waveguide lasers were realised for two doping concentrations of 0.4 and 0.5 wt%.

5.6 References

1. Goell, J. E.
Bell Syst. Tech. J., 1969, **48**, 2133.
2. Kumar, A., Haul, A. K., and Chatak, A. K.
Opt. Lett., 1985, **10**, 86.
3. Marcatili, E. A. J.
Bell Syst. Tech. J., 1969, **48**, 2071.
4. Kawachi, M.
Opt. and Quant. Electron., 1990, **22**, 391.
5. Sze, S. M.
Semiconductor Devices
John Wiley & Sons, Inc., 1985.
6. Magab, C. J, Adams, C. A., and Flamm, D. L.
J. Appl. Phys., 1978, **49**, 3796.
7. Steinbruchel, Ch., Lehmann, H. W., and Kirk, F.
J. Electrochem. Soc., 1985, **132**, 180.
8. Ruby, B. A.
J. Vac. Sci. Technol., 1980, **23**, 117.
9. Izawa, T., Mori, H., Murakami, Y., and Shimizu, N.
Appl. Phys. Lett., 1981, **38**, 483.
10. Maxwell, G. D.
Private communication.
11. Izawa, T., Mori, H., Murakami, Y., and Shimizu, N.
Appl. Phys. Lett., 1981, **38**, 483.
12. Marcuse, D.
J. Lightwave Techn., 1989, **7**, 336.
13. Hattori, T., Hattori, K., Shimizu, M., Ohmori, Y., and Kobayashi, M.
Electron. Lett., 1985, **27**, 334.
14. Ainslie, B. J., Armitage, J. R., Craig, S. P., and Wakefield, B.
Mater. Lett., 1988, **6**, 139.
15. Ainslie, B. J., Craig-Ryan, S. P., Davey, S. T., Armitage, J. R., Atkins, C. G., Massicott, J. F., and Wyatt, R.
IEE Proc., Pt. J, 1990, **137**, 205.
16. Hattori, K., Kitagawa, T., Ohmori, Y., and Kobayashi, M.
IEEE Photonics Technol. Lett., 1991, **3**, 882.

Chapter 6 Monolithic Integration of Rare Earth Doped Silica Planar Waveguide Lasers and Amplifiers

6.1 Introduction

Chapter 6 is split into two sections concerning the monolithic integration of rare earth doped silica planar waveguide lasers and amplifiers. The first section deals with the realisation of rare earth regional and vertical selective area doping of SiO_2-P_2O_5 planar films fabricated by FHD. The second section is concerned with the fabrication of gratings with a view to be used as Bragg reflectors in an integrated waveguide laser, or as filters acting to flatten the gain spectrum of amplifiers [1].

6.2 Selective Area Doping of Planar Waveguides Fabricated by FHD

Regional selective area doping of planar waveguides is important since it permits monolithic integration of active and passive optical functions and enables the multiplexing of pump and signal wavelengths, of particular significance for the three level Er^{3+} laser system. Vertical selective area doping is also of interest as it facilitates control of the rare earth doping profile, such that the peak doping level is situated in the centre of the film, coinciding with the maximum intensity of the cladded waveguide mode [2]. This may have important implications for long path length integrated amplifier structures [3], as it permitting a more efficient excitation of the rare earth ions and hence may produce amplifier structures with improved signal gain-pump power characteristics. A similar technique has been applied to Er^{3+} doped fibre amplifiers [4].

Regional selective area doping of planar films fabricated by FHD may be accomplished using both the solution and aerosol doping techniques [5]. As illustrated in figure 6.1, regional selective area doping may be realised by a multi-step fabrication process, involving multiple deposition and consolidation steps and RIE. Selective area doping is possible due to the fact that the rare earth ions are 'locked' and do not diffuse from the consolidated rare earth doped region, as confirmed by Secondary Ion Mass Spectroscopy (SIMS) analysis. The disadvantage of this technique is that it is a multi-step process.

As previously discussed in chapter 4, using the aerosol doping technique, the rare earth concentration incorporated into the glass is dependent on the carrier gas flow rate transporting the aerosol to the torch. Consequently, regional selective area doping of a planar film was achieved by interrupting the aerosol delivery during the traversal of the torch during a soot deposition, as shown in figure 6.2.

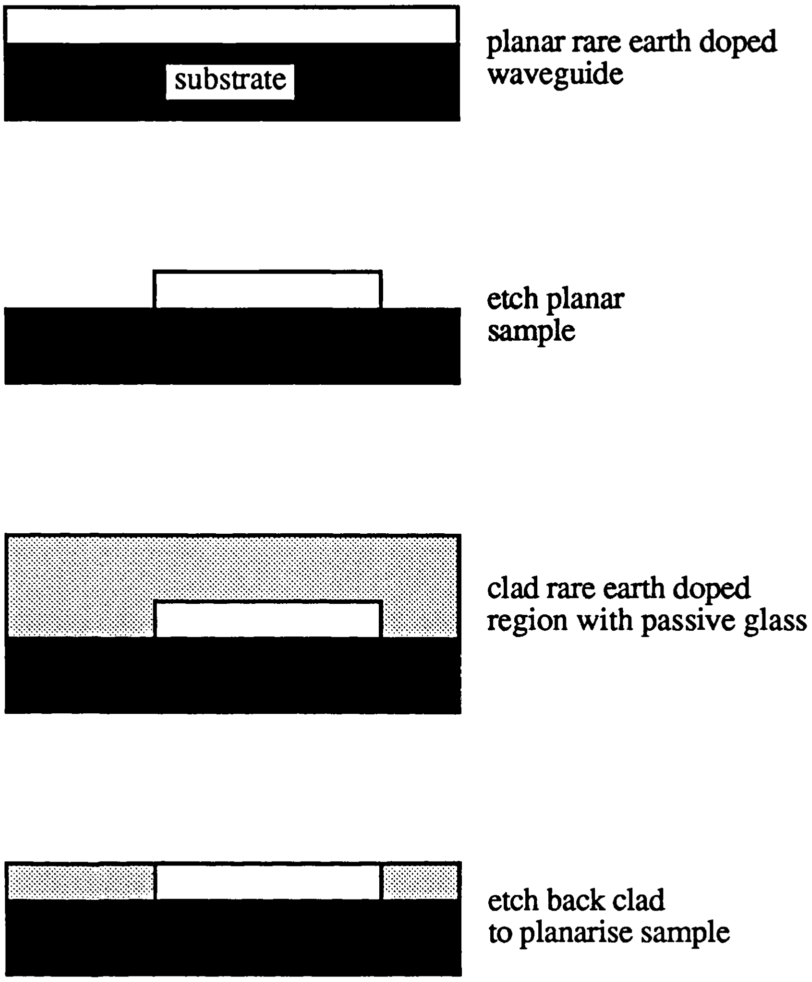

Figure 6.1 Schematic diagram of proposed multi-step fabrication process for achieving regional selective area doping of planar films fabricated by FHD.

Figure 6.3 shows a photograph of the 465 nm output from an argon ion laser prism coupled into a regional selective area Eu^{3+} doped SiO_2-P_2O_5 planar waveguide. Eu^{3+} has an absorption band at 465 nm and fluoresces in the red region of the visible spectrum. The area which was not doped with Eu ions, on the left side of the sample, is visible by the out of plane scatter of the blue light and the Eu^{3+} regionally doped area on the right is evident by the red fluorescence. Furthermore, it should be possible to dope selected areas of the SiO_2-P_2O_5 film with different dopants by nebulising different solutions during the torch traversal.

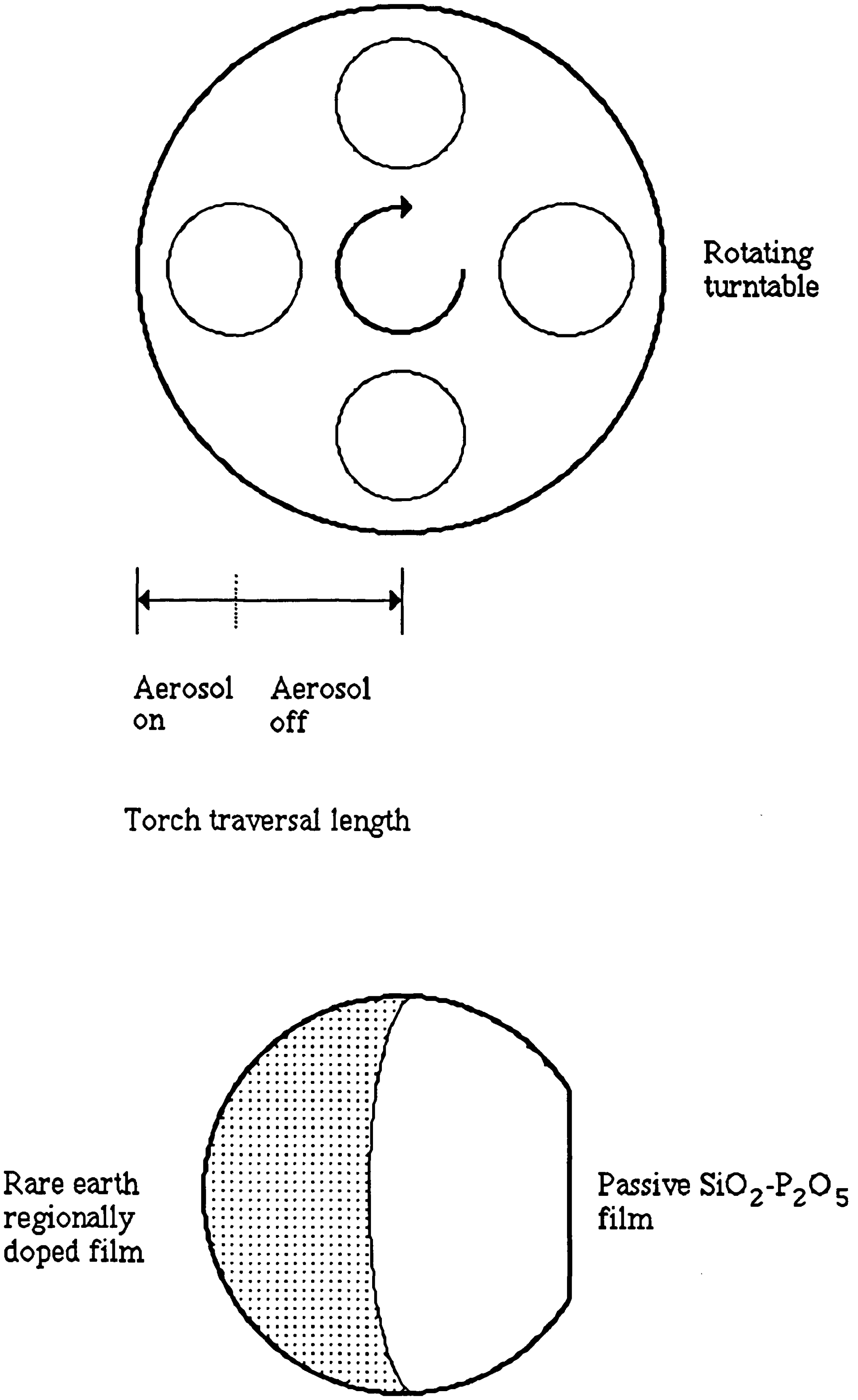

Figure 6.2 Regional selective area doping of planar films using the aerosol doping technique.

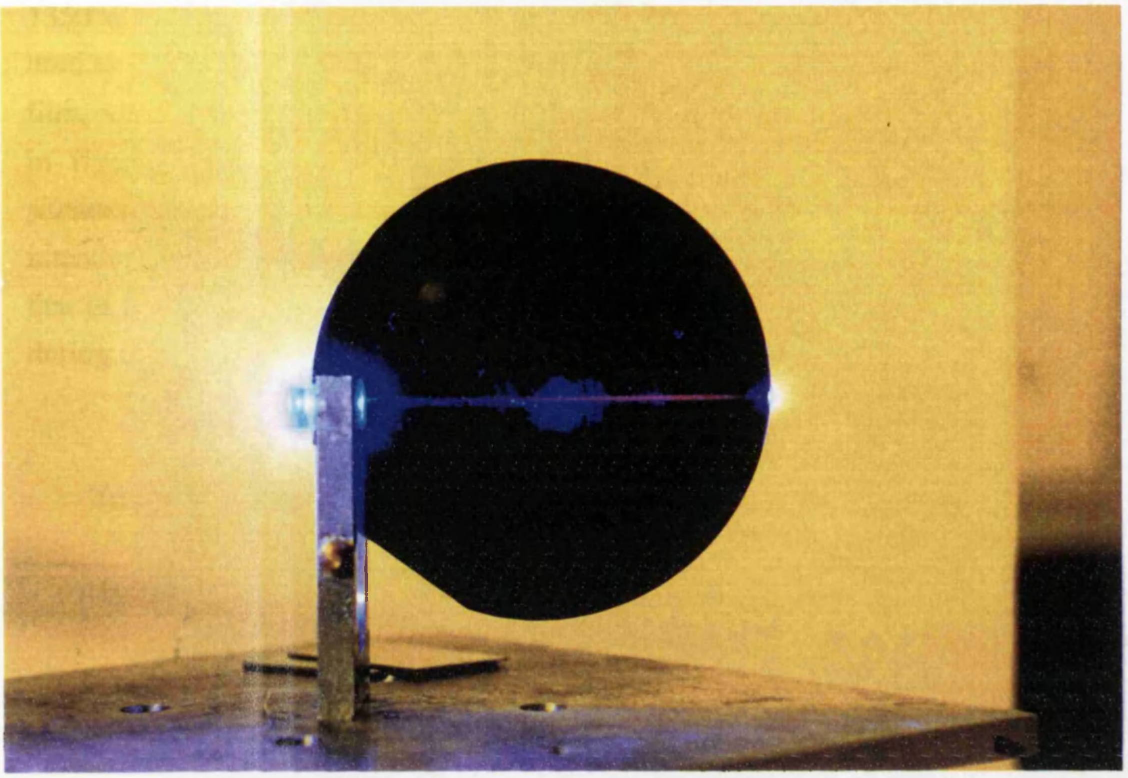

Figure 6.3 Photograph of 465 nm output from argon ion laser prism coupled into Eu^{3+} regionally selective area doped SiO_2-P_2O_5 planar film.

One disadvantage of this technique was the inability to produce a distinct boundary between rare earth doped and undoped regions, a consequence of the size of the flame in contact with the substrate and the torch traversal rate. The area of the substrate affected by the diffuse boundary between the doped and undoped regions, indicated in figure 6.3 by the region of scattered blue light is estimated to be 1 cm, approximately the diameter of the flame. Analysis of the doped region using energy dispersive x-ray analysis (EDAX) would yield information about the homogeneity of the rare earth doping level.

Vertical selective area doping of the planar film was also demonstrated using the aerosol doping technique by controlling the aerosol carrier gas flow rate during the deposition. Control of the rare earth vertical doping profile in the waveguide film was achieved by first depositing a low density glass soot layer onto the substrates by feeding $SiCl_4$ and PCl_3 to the torch. The aerosol carrier gas flow rate was then increased to 3 litres/minute without disrupting the $SiCl_4$ and PCl_3 flow rates. The second deposited layer of glass soot was therefore doped with rare earth ions. For the third and final deposited layer, the aerosol carrier gas was switched off, but the $SiCl_4$ and PCl_3 flow rates were maintained. The substrates were then removed from the turntable and sintered at

1350°C for 2 hours. Table 6.1 gives a detailed account of the fabrication parameters used to achieve vertical selective area doping for a 6 μm thick Er^{3+} doped SiO_2-P_2O_5 film, with the SIMS profile of the elements P and Er^{3+} vertically through the film given in figure 6.4. It is evident from figure 6.4 that the peak doping level of the Er^{3+} is situated in the centre of the film, but the Er ions were not confined to the centre 2 μm as intended, but diffused throughout the film, resulting in a profile with a FWHM 80% of that of the P profile. The diffusion of the Er ions through the film probably occurred during both the deposition and sintering fabrication steps.

Traversal number	Halide flow rate (sccm)	Aerosol carrier gas flow rate (l/min)
1-4	$SiCl_4$ 150 PCl_3 160	0.25
5-8	$SiCl_4$ 150 PCl_3 180	3
9-12	$SiCl_4$ 150 PCl_3 160	0.25

H_2 flow rate: 4 litres/minute
O_2 flow rate: 6 litres/minute
Nebulised aqueous solution: 0.4 molar $ErCl_3$.

Table 6.1 Fabrication parameters used to achieve vertical selective area doping of 6 μm thick Er^{3+} doped SiO_2-P_2O_5 film

Two modifications to the above procedure were performed in an attempt to improve the confinement of the rare earth ions to the centre of the waveguide region. The first method involved switching off the flow of the halides after each group of four traversals as listed in table 6.1 and partially sintering the deposited soot layer with the flame for four further traversals of the torch. However, no improvement in the confinement of the rare earth ions was measured by SIMS analysis. The second method adopted the procedure used to confine the rare earth ions to the centre of the core of optical fibres by codoping with Al [6]. The fabrication parameters were identical to those listed in table 6.1, but the nebulised solution was a mixture of 0.2 molar

$Al(NO_3)_3$ and 0.1 molar $ErCl_3$. Due to the low doping levels of Al and Er^{3+} in this particular case, results from SIMS analysis of the doping profiles were inconclusive and hence further investigations are required.

Nonetheless, the aerosol doping technique gave a greater degree of control of the vertical doping profile compared to the solution doping technique, as there is no fabrication variable available using the solution doping technique which influences the doping profile. Illustrating the lack of control of the doping profile using the solution doping technique, figure 6.5 gives the vertical doping profile of Er^{3+} through a 4 µm thick SiO_2-GeO_2-P_2O_5 film, indicating two distinct peaks: the first peak at the film surface due to immersion and drying processes and the second situated approximately in the centre of the film.

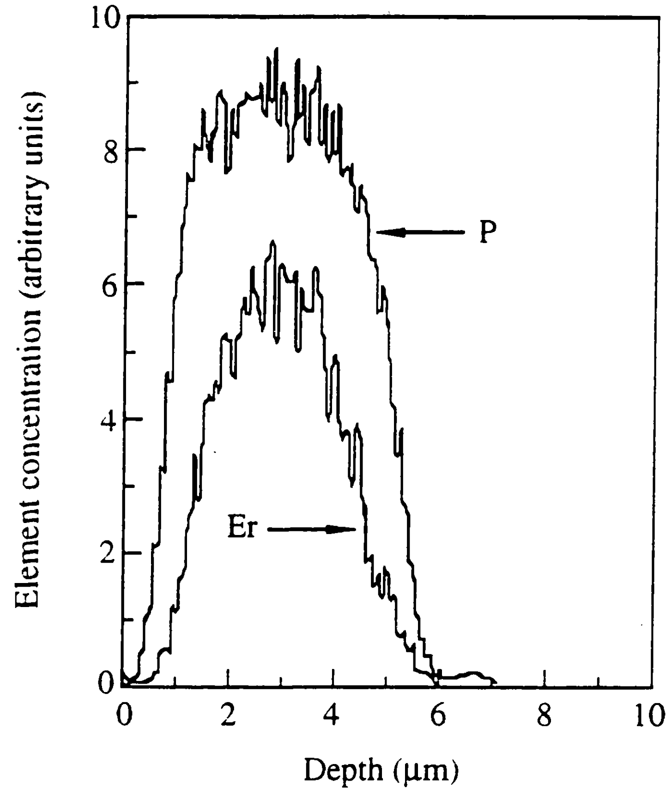

Figure 6.4 SIMS profile of the elements Er^{3+} and P vertically through the 6 µm thick Er^{3+} doped SiO_2--P_2O_5 film fabricated by the aerosol doping technique .

Greater confinement of the rare earth dopant to the centre of the waveguide region may be possible by a fabrication process involving three separate soot depositions and sintering steps: the second and middle deposited glass layer doped with the rare earth ions using the aerosol or the solution doping technique. This is possible due to the fact that the rare earth ions do not diffuse from consolidated glass layers, as previously discussed. However, this method would be time consuming and would remove the advantage of the aerosol doping technique which potentially may form rare earth doped samples which are regionally and vertically selectively area doped in a single fabrication step.

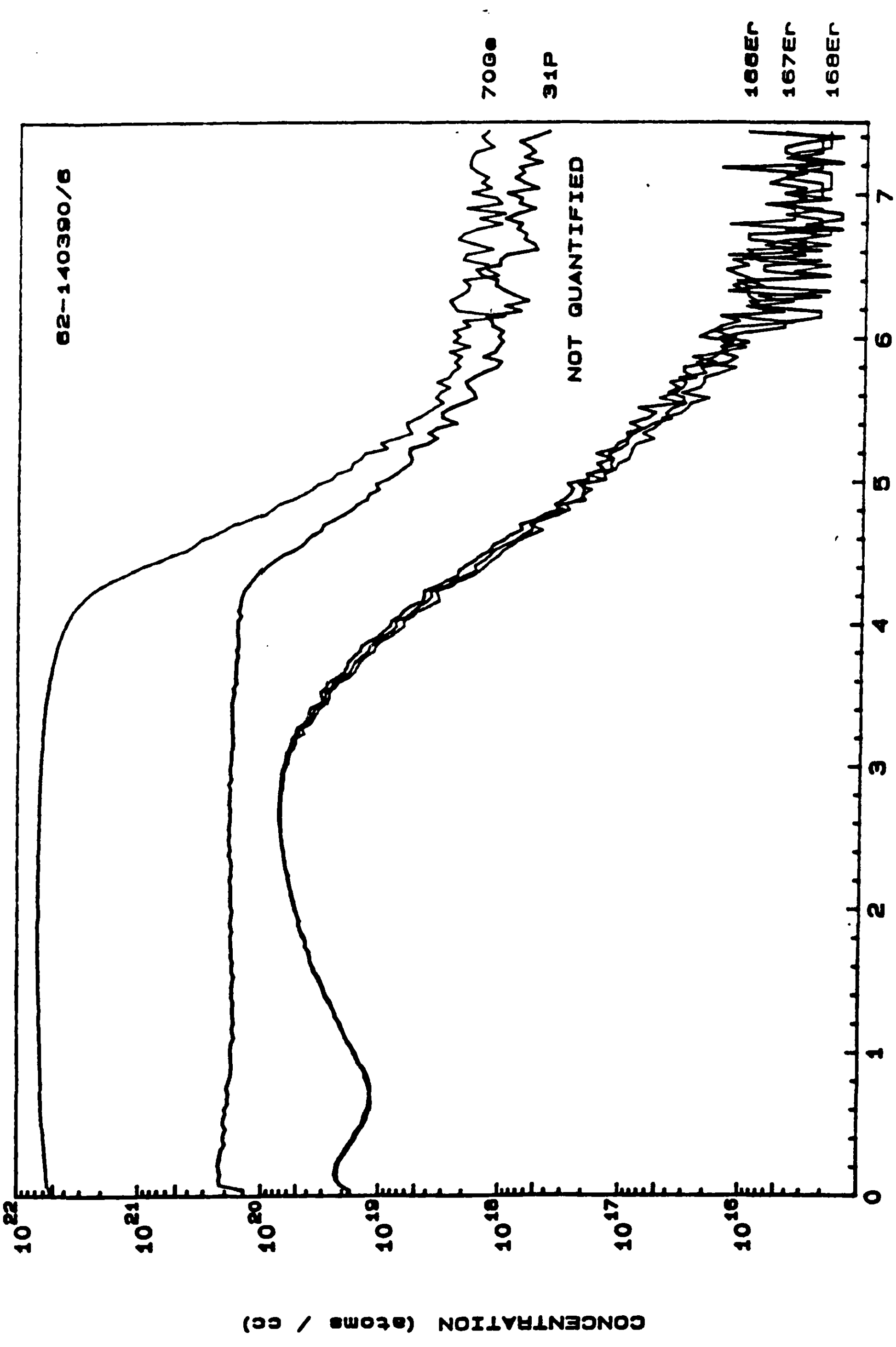

Figure 6.5 SIMS profile of Er^{3+} vertically through a 4 μm thick SiO_2-GeO_2-P_2O_5 film, the Er^{3+} incorporated by the solution doping technique .

6.3 Grating Fabrication and Assessment

Regional selective area doping permits monolithic integration of rare earth doped planar waveguide lasers, but the presence of external mirrors or the direct coating of a dielectric mirror at each end of the substrate to provide the necessary feedback for laser action makes integration difficult. Furthermore, external mirrors are sensitive to vibration and misalignment. One solution to this problem is the use of a grating structure acting as a Bragg reflector which would allow integration of a laser, provide single longitudinal mode operation and would be insensitive to vibration. Another possible application is to incorporate the grating structure within the length of the amplifier structure in order to smooth the gain spectrum and saturation characteristics, similar to that used for Er^{3+} doped fibre amplifiers for WDM applications [1,7]. Unlike the optical fibre equivalent though, the integrated optic grating would be rugged, with the centre wavelength and strength of the filter precisely defined.

There are several publications which give a detailed treatment of the coupled wave theory of Bragg reflectors [8-10], the method adopted in this study being that of Kogelnik.

The Bragg condition is satisfied when $\Lambda = \lambda_g/2$, where Λ is the grating period and λ_g is the wavelength of light in the waveguide. The reflectivity of the grating is dependent on the grating length L and the coupling coefficient κ between the incident and reflected waves, where κ for TE waves is given by:

$$\kappa = \frac{\pi h\left(n_g^2 - n_c^2\right)E_c^2}{2\lambda N \int_{-\infty}^{-\infty} E_y^2 dx} \qquad (6.1)$$

where:

κ = coupling coefficient
h = amplitude of grating corrugation ($h < \Lambda$ for expression to hold)
N = effective index
n_g = guide index
n_c = clad index
E_c = transverse electric field at grating surface
$\int_{-\infty}^{\infty} E_y^2 dx$ = integral of square of electric field over transverse direction

The maximum reflectivity R for a sinusoidal grating is specified by:

$$R = \tanh(\kappa L) \tag{6.2}$$

The dependency of the peak reflectivity of a grating structure as a function of the length for different amplitudes of corrugation, for λ=1.05 μm and 1.53 μm, are plotted in figures 6.6 and 6.7 respectively. In both cases the waveguide thickness is 6 μm, with a relative refractive index difference between the guide and the substrate and clad of 0.75%.

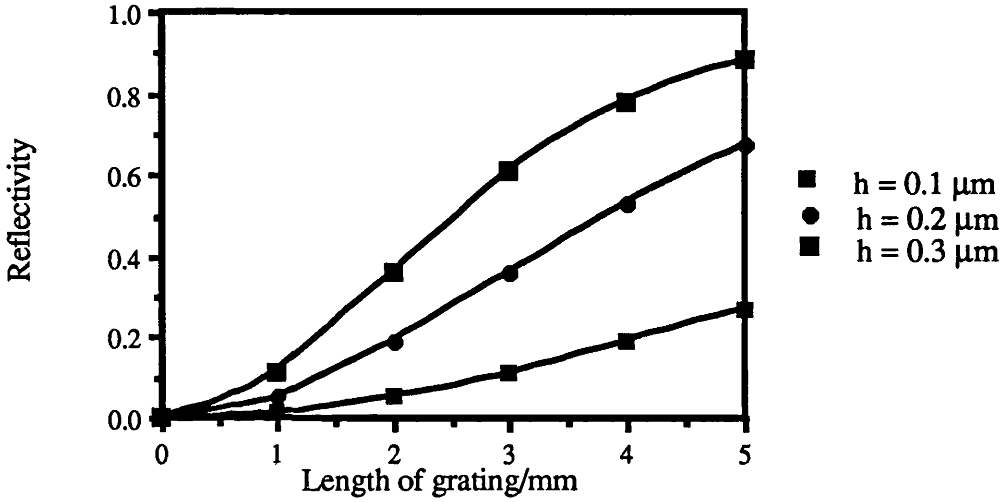

Figure 6.6 Reflectivity of grating for different lengths and corrugation amplitude, with a period of 530 nm designed for λ=1.53 μm.

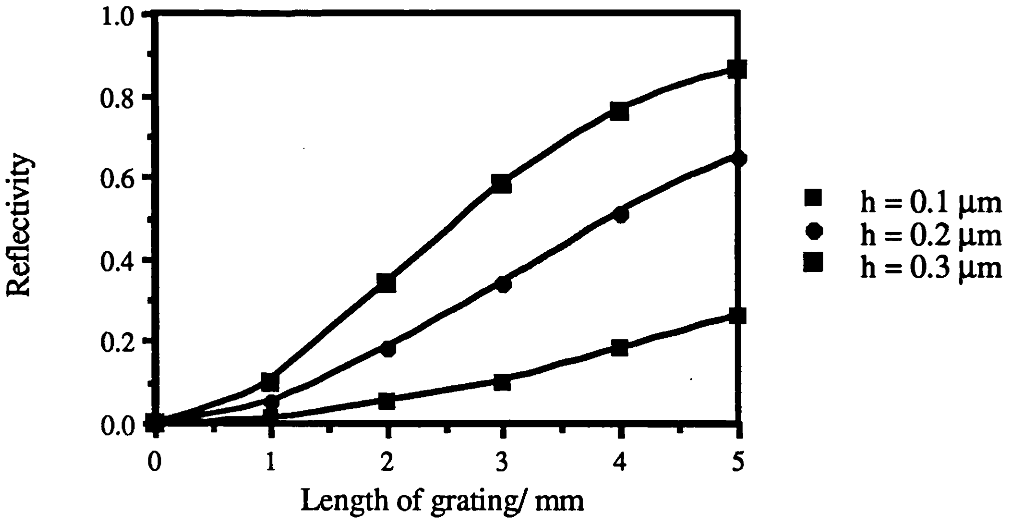

Figure 6.7 Reflectivity of grating for different lengths and corrugation amplitude, with a period of 360 nm designed for λ=1.05 μm

The linewidth of the grating is defined as:

$$\Delta\lambda = \frac{2\lambda N}{Ln_g}\left[1 + \left(\frac{\kappa L}{\pi}\right)^2\right]^{\frac{1}{2}} \qquad (6.3)$$

where n_g is the group effective index, which is approximated to be equal to N.

The linewidth of the gratings modelled in figures 6.6 and 6.7 was calculated to be approximately 0.1 nm.

The methods employed to fabricate the grating structures were the holographic [11] and electron beam lithography techniques [12].

The holographic technique has the advantage of defining a grating over a large area, approximately a centimetre square, in a short period of time. As shown in figure 6.8, this involved light from an argon ion laser λ = 457.9 nm being divided into two beams of equal intensity, the beams recombined after being directed through beam expanders and spatial filters, necessary to remove any high spatial frequency noise present in the expanded beams. The substrates were situated at the point where the two beams recombined, the resultant interference pattern exposing photoresist coating the substrates, producing a low contrast grating after development. The substrates used were 20 mm square, 1 mm thick Homosil grade silica, which were bonded to a matt black glass prism with RO water. The substrates were held in such a manner in order to suppress any reflections from the transmitted beams which may form a spatial interference pattern, thus reducing the definition of the grating.

The period of the interference fringes and hence period of the grating is given by:

$$\Lambda = \frac{\lambda}{2 \sin \theta} \qquad (6.4)$$

where λ = 457.9 nm and θ is the angle of incidence of the beams on the photoresist surface. The photoresist used was S1400-31, which had been thinned down by a 1:2 ratio (33%), resulting in a film thickness of approximately 0.12 μm after being spun at 4000 rpm for 30 seconds. A typical exposure time was 25 seconds, followed by development in a 2:1, water:developer mixture for 15 seconds.

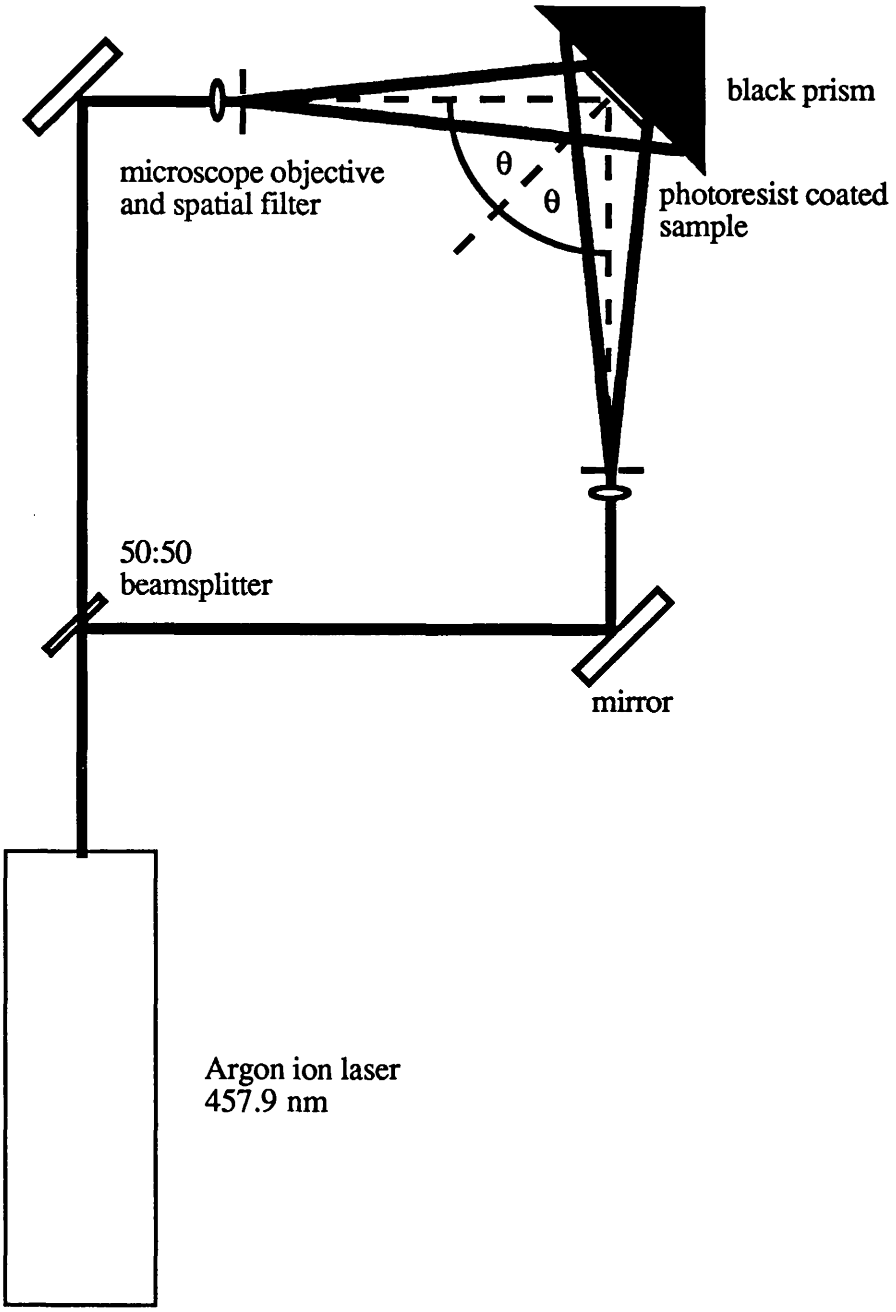

Figure 6.8 Diagram of interferometer arrangement for production of gratings.

Following development, the samples were placed in an evaporator and shadow masked with 30 nm of nichrome, at an angle of 70°, calculated to give an aspect ratio of 1:1 for the final grating structure. The samples were given a low pressure O_2 etch for 2 minutes to remove any residual resist, before being etched by a low pressure CHF_3 process which gave an etch rate of 30 nm/minute. The remaining mask material was removed in an acetone ultra sonic bath leaving the grating structure, which was overgrown with a SiO_2-P_2O_5 film. The different steps involved in the fabrication process are illustrated below in figure 6.9.

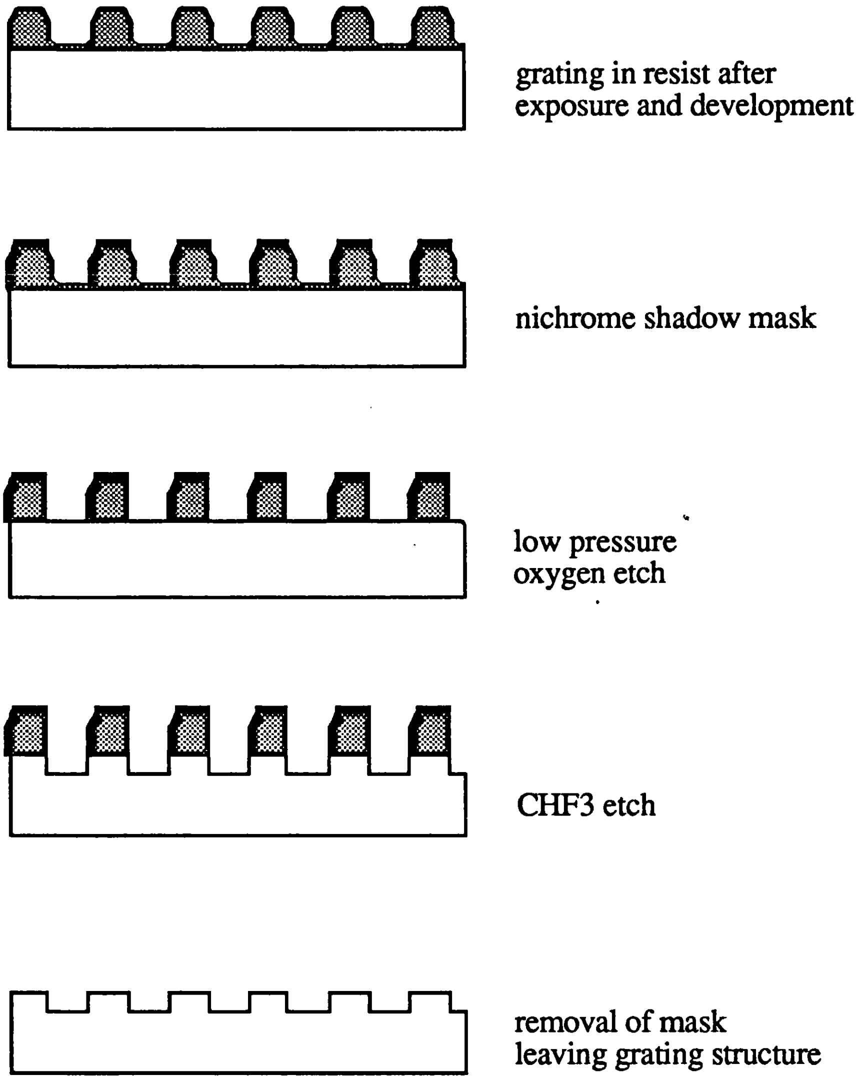

Figure 6.9 Diagram of processing steps involved in the fabrication of grating structure.

Gratings were formed over selected areas by exposing the samples using the mask aligner for 60 seconds prior to exposure to the interference pattern, the opaque areas on the mask defining the areas on the substrate ~~which~~ where the gratings would be formed. Figure 6.10 is a SEM photograph of a grating formed on a silica substrate and figure 6.11 is a SEM photograph of a grating formed over a defined area, achieved using the double exposure technique.

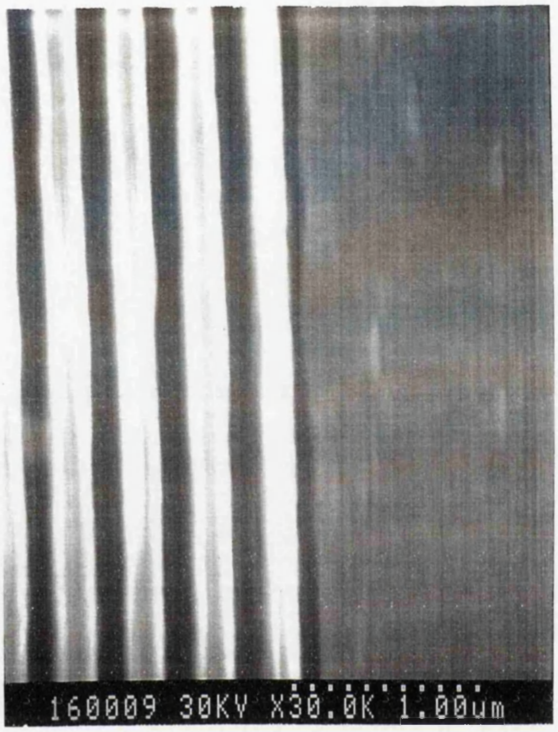

Figure 6.10 SEM photograph of grating formed by holographic technique.

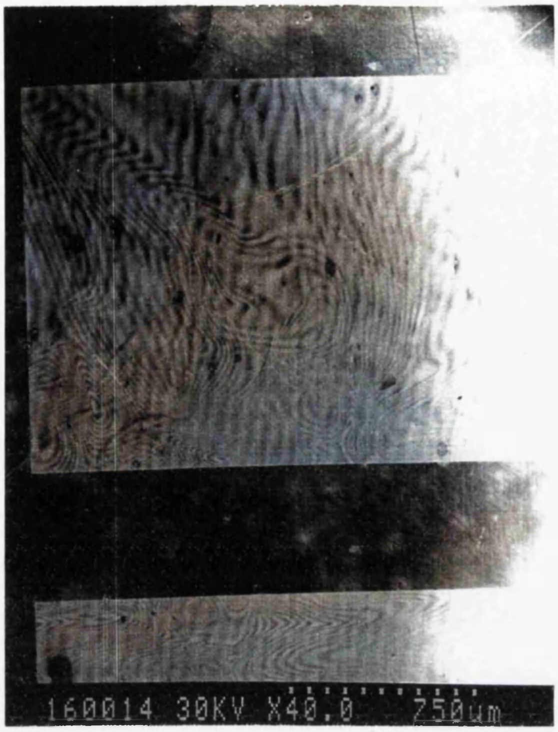

Figure 6.11 SEM photograph of grating formed over selected area achieved by double exposure.

The second technique used to form the grating structures was the electron beam (e-beam) writing method and I acknowledge R. Harkins for the e-beam writing and sample processing.

The e-beam writer used was the Phillips EBPG5-HR and the software package used to design the gratings was Sigraph-Optik, a Siemens software package, which enabled design of the length, width and period of the grating. A GDSII file was created and transferred to a Computer Aided Transcription System (CATS), a program that transcribed CAD design into readable instructions for the e-beam writing machine. The e-beam writer operated at 50 KeV using the vector scan principle, with an e-beam with a guassian cross-section. The spot size of the focussed e-beam was 40 nm. The resolution was 21.2 nm, which was a divisible factor into the period of the grating, equal to 0.53 µm, suitable for application as a Bragg reflector operating at 1.53 µm. The pattern was written in 400 µm square blocks which were stitched together to form grating structures over areas ranging from 1 to 5 mm^2.

Prior to writing the grating, the silicon substrate with a 10 μm thick oxide layer was cleaned using the standard cleaning process outlined earlier. The sample was then coated in e-beam sensitive resist. 4% BDH PMMA (poly methyl methacryllate): a solution of xylene (solvent) and BDH PMMA, with 4% of the total weight being PMMA, was spun onto the sample at 5000 rpm for 60 seconds and then baked at 180°C for 2 hours. The sample was then coated with 4% Elv PMMA by spinning at 5000 rpm for 60 seconds and baked overnight. A 30 nm thick chrome layer was evaporated onto the sample to avoid charging-up problems during the writing. Following completion of the writing, the chrome was removed by an ammonium nitrate, acetic acid and water wet etch and the resist developed in 3:1 IPA:MiBK mixture for 30 seconds at 23°C. To ensure complete removal of the residual resist, the sample was placed in a oxygen plasma for 30 seconds. A 30 nm thick chrome film was evaporated onto the sample, prior to a 'lift-off' process in acetone at 45°C in a water bath, producing a suitable mask for RIE using the low pressure CHF_3 process.

A grating structure with a 1:1 mark:space ratio, shown in figure 6.12, was achieved using a 600 $\mu C/cm^2$ dose, which was able to be formed over selected areas as illustrated in figure 6.13. The e-beam writing method had the advantage of being to form gratings with a high resolution, with an accurately assigned position and orientation. However, a disadvantage was the long time involved in writing gratings over the large areas required.

An attractive alternative to gratings formed by RIE is permament, photoinduced gratings formed by the absorption of UV radiation in Ge-doped silica planar waveguides [13]. This technique has the advantage of directly writing and controlling the strength of the grating structure and UV written gratings in planar waveguides formed by FHD have been shown to give reflectivities of 13 dB, with a bandwidth of 0.6 nm [14]. This technique is potentially the most applicable for the formation of integrated grating structures in future planar devices.

Figure 6.12 SEM photograph of grating formed by e-beam writing technique.

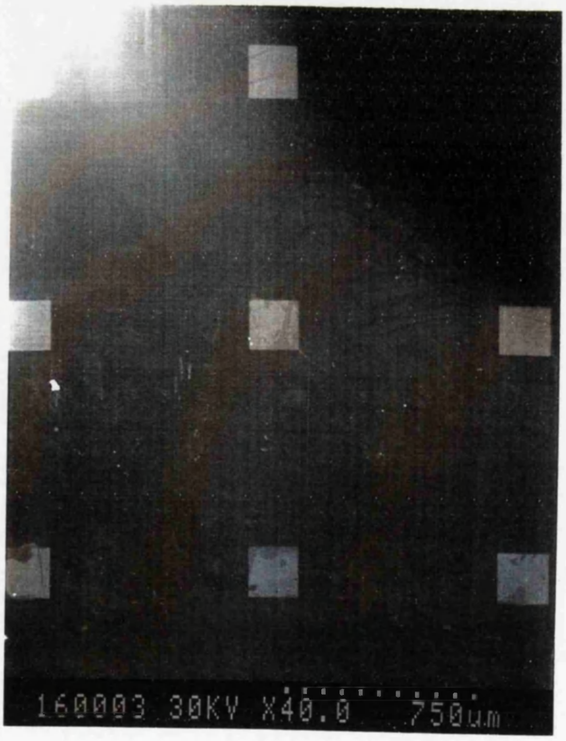

Figure 6.13 SEM photograph of grating formed over selected areas by e-beam writing.

6.4 Conclusion

Rare earth regional and vertical selective area doping of SiO_2-P_2O_5 planar films formed by FHD was demonstrated for the first time using the aerosol doping technique. Multiple-step fabrication processes were also proposed to enable selective area doping with a more distinct boundary between rare earth doped and undoped regions using both the solution and aerosol doping techniques.

Grating structures were formed by holographic and electron beam lithography techniques, both techniques giving the possibilty of forming the grating structure over selected areas, which may be used in future integrated laser and amplifier structures.

6.5 References

1. Tachibana, M., Laming, R. I., Morkel, P. R., and Payne, D. N.
IEEE Photon. Technol. Lett., 1992, **4**, 852
2. Bebbington, J. A., Barbarossa, G., Bonar, J. R., and Aitchison, J. S.
Appl. Phys. Lett., 1993, **62**, 337.
3. Rasmussen, T., Lumholt, O., Povlsen, J. H., and Bjarklev, A.
Electron. Lett., 1993, **29**, 455.
4. Armitage, J. R.
Appl. Opt., 1988, **27**, 4831.
5. Bebbington, J. A., Barbarossa, G., Bonar, J. R., and Aitchison, J. S.
Proc. OSA Annual Meeting, Albuquerque, 1992.
6. Ainslie, B. J., Craig-Ryan, S. P., Davey, S. T., Armitage, J. R., Atkins, C. G., Massicott, J. F., and Wyatt, R.
IEE Proc., Pt. J, 1990, **137**, 205.
7. Wilkinson, M., Bebbington, A., Cassidy, S. A., and McKee, P.
Electron. Lett., 1992, **28**, 131.
8. Kogelnik, H.
'Theory of Dielectric Waveguides' in 'Topics in Applied Physics', **7**, Integrated Optics.
Springer Verlag, 1975.
9. Taylor, H. F., and Yariv, A.
Proc. IEEE, 1974, **62**, 1044.
10. Nishihara, H., Haruna, M., and Suhara, T.
Optical Integrated Circuits.
McGraw-Hill Optical and Electro-optical Engineering Series.
11. Yi-Yan, A., Wilkinson, J. A. H., and Wilkinson, C. D. W.
IEE Proc., Pt. H, 1980, **127**, 335.
12. Thoms, S.
EBL Fundamentals, Departmental Report.
13. Maxwell, G. D., Ainslie, B. J., Williams, D. L., and Kashyap, R.
Electron. Lett., 1993, **29**, 425.
14. Maxwell, G. D., Kashyap, R, Ainslie, B. J., Williams, D. L., and Armitage, J. R.
Electron. Lett., 1992, **28**, 2106.

Chapter 7 Conclusion and Future Work

In this final chapter, the major achievements from the project are reviewed and future areas of work arising from this project are outlined.

7.1 Conclusion

SiO_2-P_2O_5 planar waveguides formed by FHD were doped with rare earth ions using the solution doping technique and for the first time in the planar geometry, by an aerosol doping technique, in order to develop integrated optic lasers and amplifiers.

Research concentrated on the binary glass SiO_2-P_2O_5 as: P_2O_5 increases the solubility of the rare earth ions in the silica glass host; decreases the consolidation temperature; and acts to increase the refractive index of the glass. The SiO_2-P_2O_5 films were fabricated using a 3 port quartz torch: the metal chloride vapour and nitrogen carrier gas, hydrogen and oxygen fed through the centre, second and outermost conduits respectively. The hydrogen and oxygen flow rates were 4 litres/minute and 6 litres/minute. The flow rate of the nitrogen carrier gas used to transport the $SiCl_4$ to the torch was kept constant at 150 sccm. During the deposition, the torch traversed in a radial direction with respect to a rotating turn-table and the low density glass soot synthesized by the flame hydrolysis was deposited onto silica or oxidised silicon substrates which were placed on the turn-table. The torch traversal rate was kept constant at 15 cm/minute and the turn-table rotation rate was 30 revolutions/minute. Film thickness and refractive index were determined independently by varying the number of traversals of the torch and the flow rate of the nitrogen gas used to transport the PCl_3 vapour, respectively. To produce high quality, passive planar films, the glass soot was sintered at temperatures up to 1350°C for 2 hours in an air atmosphere.

The homogeneity of planar film thickness and refractive index was investigated for the multimode SiO_2-P_2O_5 films using 'p-etch' and prism coupling techniques. For a continuous traversal speed of the torch, film thickness varied by 17%, but the inhomogeneity in the refractive index was below 0.1%. The increase in refractive index of the film relative to the substrate was found to be proportional to the PCl_3 flow rate. The maximum obtainable refractive index change of the film relative to the substrate was approximately 0.9 %, obtained using a 200 sccm PCl_3 flow rate, corresponding to a P_2O_5 concentration of approximately 45 wt%. On increasing the PCl_3 flow rate further, a gel was obtained on the substrate rendering the film unsuitable for consolidation. The propagation loss of the passive planar films, measured by the three prism technique, was below 0.1 dB/cm.

Rare earth doping of the SiO_2-P_2O_5 films was accomplished by the solution doping and by a novel aerosol doping technique. For integrated optic waveguide lasers and amplifiers, the concentration of rare earth dopant must be higher than that found in fibre lasers and amplifiers to overcome the higher losses and the shorter length of the active medium. Both the solution doping and aerosol doping techniques proved successful in producing low loss films with rare earth doping levels suitable for producing efficient lasers and amplifiers.

The solution doping technique involved the deposited soot being partially sintered at a reduced temperature, typically 960°C for 30 minutes. The resultant porous structure was then immersed in an alcohol solution of the required rare earth chloride. Immersion times varied from 5 to 15 minutes and solution strengths from 0.01 to 0.04 molar, giving rare earth doping levels ranging from 0.1 to 0.6 wt%. The degree of partial sintering also determined the doping level and had to be controlled. After immersion, the sample was dried and completely consolidated. The drying process was found to be important in minimising the in-plane and out-of-plane scatter of the planar guides: the most effective method of drying accomplished by spinning the sample after immersion at 3000 rpm and then placing on a hot plate for 5 minutes.

The second method, developed during the course of this project, employed an aerosol doping technique which directly incorporated the rare earth ions into the glass soot during the deposition [Appendix I]. The aerosol generator was a PVC pneumatic atomiser and zero grade nitrogen gas was used to atomise the aqueous solution and to deliver the resultant aerosol droplets to the torch. Superior reproducibility of rare earth doping levels, quality of flame shape and deposition uniformity were achieved when the aerosol was fed into the third conduit, between the hydrogen and oxygen in a four port torch. The rare earth dopant level incorporated into the glass was dependent on: the strength of the nebulised aqueous solution; the carrier gas flow rate transporting the aerosol to the torch; and position of the torch with respect to the turn-table during the deposition. Using a nitrogen flow rate of 2.8 litres/minute, a rare earth doping level of 0.15 wt% was obtained using a 0.1 molar solution strength, increasing to 0.55 wt% for a 0.4 molar solution strength. The soot deposition rate for the four port torch decreased by a third in comparison to the three port torch when using identical halide flow rates, torch and turn-table speeds. Furthermore, the refractive index difference of a film relative to the substrate fabricated using the four port torch was lower by approximately 20 % for identical PCl_3 flow rates in comparison to a film fabricated using the three port torch. The differences were due to different flame shape, greater flame turbulence and lower flame temperature resulting from the high nitrogen flow rate used as the carrier gas for the aerosol.

The loss of planar rare earth doped films was investigated using the three-prism and fibre-probe techniques and was found to be determined by the solubility of the rare earth ions in the glass host, which was a function of the rare earth and P_2O_5 codoping concentrations. For 0.4 wt% Nd^{3+} doped SiO_2-P_2O_5 films, with a relative index difference of 0.7 % between film and substrate, the loss was measured to be 0.4 dB/cm by both the fibre-probe and three-prism technique. The loss increased to 1.1 dB/cm for a 0.6 wt% Nd^{3+} doping level due to increased volume scattering, arising from the non-uniform distribution of the rare earth ions. With a P_2O_5 dopant level 25 % lower and 0.1 wt% Nd^{3+} doping level, the loss was measured to be 0.6 dB/cm using the fibre-probe technique. The loss of films fabricated by the solution and aerosol doping techniques with comparable rare earth and P_2O_5 codoping levels was similar.

Furthermore, regional and vertical selective area doping of planar films fabricated by FHD may be accomplished using both the solution and aerosol doping techniques. Regional selective area doping may be realised by a multi-step fabrication process, involving multiple deposition and consolidation steps and RIE. Likewise with vertical selective area doping. However, the major advantage of the aerosol doping technique over the solution doping technique is the ability to produce regional and vertical selective area doping in a single fabrication step. This was demonstrated for the first time by controlling the aerosol delivery during the traversal of the torch during the soot deposition. Control of the rare earth vertical doping profile in the waveguide film was achieved by first depositing a low density glass soot layer onto the substrates by feeding $SiCl_4$ and PCl_3 to the torch. The aerosol carrier gas flow rate was then increased without disrupting the $SiCl_4$ and PCl_3 flow rates. The second deposited layer of glass soot was therefore doped with rare earth ions. For the third and final deposited layer, the aerosol carrier gas was switched off, but the $SiCl_4$ and PCl_3 flow rates were maintained. The deposited soot was then sintered producing a film with the peak rare earth doping level situated in the centre of the film. Vertical selective area doping may have important implications for long path length integrated amplifier structures, as it enables a more efficient excitation of the rare earth ions and hence may produce amplifier structures with improved signal gain-pump power characteristics.

Ridge waveguides were formed by a combination of photolithographic and reactive ion etching techniques. Three etching processes were analysed for their suitability for etching passive and rare earth doped SiO_2-P_2O_5 films. The processes examined were:

a low pressure, high DC bias CHF_3 process developed by the author; a high pressure, high power C_2F_6 plus O_2 process; and a C_2F_6 plus C_2H_4 process. The etch depth was determined by talystep measurements and the etch quality by SEM analysis. The redeposition of non-volatile rare earth products during the etching process was minimised by using the low pressure, high DC bias CHF_3 process and hence this process was selected to form the channel waveguides.

Loss measurements were performed on Nd^{3+} doped SiO_2-P_2O_5 channel waveguides using the fibre-probe technique for samples with no glass cladding layer and a method entailing the butt-coupling of optical fibres to the channel waveguides and measuring the insertion loss for waveguides clad with SiO_2-B_2O_3-P_2O_5 glass. The loss for 20 μm wide channel waveguides formed by the CHF_3 process, which etched through the 6 μm thick core and 1.2 μm into the buffer layer, measured at 632.8 nm using the fibre-probe technique was 6.5 dB/cm for a 0.4 wt% Nd^{3+} doping level. The loss was reduced to 2.5 dB/cm, after reflowing the waveguides at 1000°C for 30 minutes. The annealing process was therefore effective in reducing the loss of the channel waveguides. The loss reduced to 0.5 dB/cm at 1.54 μm when the waveguide was clad with SiO_2-B_2O_3-P_2O_5 glass, the refractive index of which was tailored to match that of the substrate. In order to reduce the loss of the channel waveguides further, the etch depth into the silica buffer layer, after etching through the core layer, was increased to 3 μm to increase the separation between the waveguide core and the rare earth redeposition, thus decreasing the exposure of the evanescent field to the surface roughness produced by such redeposition. The loss of 8 μm wide channel waveguides fabricated in this manner was measured to be 0.5 dB/cm at 1.54 μm. A high power, high DC bias CHF_3 plus C_2F_6 process was also established to yield low loss ridge waveguides. The propagation loss for buried channel waveguides with 0.4 wt% Nd^{3+} doping level was measured to be below 0.3 dB/cm.

Fluorescence, absorption and fluorescence lifetime measurements were obtained for Nd^{3+} and Er^{3+} doped SiO_2-P_2O_5 channel waveguides, yielding information about doping levels and optical efficiencies.

The emission peak wavelengths for Nd^{3+} doped SiO_2-P_2O_5 for the transitions $^4F_{3/2}$-$^4I_{13/2}$, $^4F_{3/2}$- $^4I_{13/2}$ and $^4F_{3/2}$- $^4I_{13/2}$ were 1.32 μm, 1.051 μm and 0.880 μm respectively. The emission peaks for the three transitions were moved to shorter wavelengths than compared to Nd^{3+} doped pure silica, due to the high P_2O_5 codopant concentration. For Nd^{3+} doping levels ranging from 0.1 wt% to 0.6 wt% and for films fabricated with PCl_3 flow rates ranging from 120 sccm to 200 sccm, there was no change in the spectra for the three transitions. In addition, there was no difference in fluorescence spectra between samples fabricated by aerosol and solution doping techniques. The single emission peak and the full width half maximum for the $^4I_{13/2}$-$^4I_{15/2}$ transition for Er^{3+} doped SiO_2-P_2O_5 fabricated by the aerosol and solution doping techniques was 1.535 μm and 20 nm respectively. The difference in spectra compared to Er^{3+} doped pure silica, which has two emission peaks, the stronger at 1.535 μm and the weaker at 1.552 μm, was again due to the P_2O_5 codopant. The rare earth dopant levels were calculated by measuring the absorption peaks at 0.804 μm for Nd^{3+} and at 1.535 μm for Er^{3+} using the absorption coefficients of 5 $dBcm^{-1}wt\%^{-1}$ for the Nd^{3+} $^4I_{9/2}$- $^4F_{5/2}$ transition and 2.2 $dBcm^{-1}wt\%^{-1}$ for the Er^{3+} $^4I_{15/2}$-$^4I_{13/2}$ transition.

Fluorescence lifetime measurements concentrated on Er^{3+} doped SiO_2-P_2O_5 samples fabricated by solution and aerosol doping techniques and were measured to be approximately 7 ms for both doping techniques, with doping concentrations ranging from 0.1 to 0.6 wt%. The decay was non-exponential, with the decay rate decreasing as a function of increasing time. The observed increased decay rates and non-exponential decay were attributed to the up-conversion mechanism, indicating non-uniform distribution of the Er^{3+} in the glass host.

CW oscillation was achieved at 1.054 μm for 0.4 wt% and 0.5 wt% Nd^{3+} doped SiO_2-P_2O_5 channel waveguides. The buried channel waveguides were 6 cm long and 6 μm wide, with a core thickness of 6 μm and an index difference of the core with respect to the cladding of approximately 0.9 %. Dielectric mirrors were pressed against the end faces of the waveguide to form a Fabry-Perot cavity. The input mirror had a R=99.9% at the lasing wavelength and high transmission at the pumping wavelength. The output mirror had R=95% at the lasing wavelength and T=95% at the pumping wavelength. Pumping was carried out at 804 nm using a Ti: Al_2O_3 laser. The absorbed pump power threshold and slope efficiency were 25 mW and 3.3 %, respectively, for the 0.4 wt% Nd^{3+} doping level. A maximum output power of 1 mW was achieved.Threshold incident pump power for cw oscillation with the 0.5 wt% Nd^{3+} doping level was 450 mW, which gave a maximum output power of 2 mW, limited only by the available pump power from the Ti: Al_2O_3 laser. The slope efficiency, absorbed pump power threshold and maximum output power achieved with these devices were superior to the Nd^{3+} doped SiO_2-P_2O_5 planar waveguide lasers reported by NTT.

However, the presence of external mirrors or the direct coating of a dielectric mirror at each end of the substrate to provide the necessary feedback for laser action makes integration difficult. A grating structure acting as a Bragg reflector would enable integration of a laser, provide single longitudinal mode operation and would be insensitive to vibration. Consequently, gratings were fabricated over selected areas on a substrate by holographic and electron-beam writing techniques, suitable for use as feedback elements in future integrated laser structures, or as filters acting to flatten the gain spectrum of amplifiers, increasing the suitability for wavelength division multiplexing schemes.

In conclusion, rare earth doped planar silica devices fabricated by FHD have been shown to have potential for application in future all optical communication networks as optical amplifiers and sources, particularly in the third telecommunication window.

7.2 Future Work

Future work falls into two areas: a more detailed analysis of the rare earth doping technologies; and the demonstration of devices with applications in future all-optical transmission networks.

A more detailed study of fluorescence lifetime and optical efficiencies through gain measurement studies as a function of doping concentration and incorporation method is requisite. A thorough study of different porous structures, ranging from an open to a more closed structure, used for solution doping and the resultant optical efficiencies with identical rare earth concentrations would be beneficial. A study should also be made of the optical efficiency of rare earth doped samples fabricated using the aerosol doping technique, comparing samples fabricated with a low aerosol carrier gas flow rate, with a strong nebulised solution, to samples fabricated using an increased carrier gas flow rate, but with a decreased solution strength. Furthermore, for both of the rare earth doping methods described, the trade-off between the loss and the rare earth concentration in the waveguides and hence optical gain would also have to be examined.

The second area of future work is concerned with the advancement from material analysis to the realisation of working devices and possible commercial exploitation. Clearly the realisation of planar waveguide lasers fabricated using the aerosol doping technique is essential and would complete the comparison between the two rare earth doping technologies. The key device for future development would be a 1 x N splitter with an integrated planar amplifier compensating for the splitting losses. Deviating from the straight waveguide design to a coiling path would enable an increased signal gain and hence an increased number of output ports. Such a device could be developed in the third telecommunication using Er^{3+} and possibly at 1.36 μm using Nd^{3+}. A further possible modification to the device would be the incorporation of selective area doping to enable multiplexing of the pump and signal wavelengths. Another important device for development would involve the integration of gratings of different periods to act as feedback elements for laser sources operating at different wavelengths within the gain spectrum of the rare earth ion.